Calculation and Validation of the Noise Emission of Electric Machines

Master's Thesis

Lina Alexandra Reitz

Supervisor: Univ.Prof. Dipl.-Ing. Dr.techn. Alois Sontacchi

Graz, 2017

institut für elektronische musik und akustik

Abstract

The recent development of more powerful computers makes the simulation of electrical engines as data source for the computation of its noise emission, as opposed to measurements on the real object, more and more attractive. This work shall contribute to the response to the question to what extent Finite Element Method (FEM) based Multi-Body-Simulation (MBS) computation and noise emission computation are suited for qualitative and quantitative assessment of electric machines and where there is need for further research. At the focal point there are objective criteria such as torsional oscillation, level of structure-borne noise and noise level. Especially the accuracy of results, frequency range, model accuracy, and model depth should be put in the center of attention. A comparison of simulation results and existing measurement results is therefore executed. The simulation is carried out using a SIMULINK-model in combination with a commercial MBS-tool. Within the Multi-Body-Simulation the excitation of the chassis originating from the magnetic field is considered and from there first the structure-borne noise on the stator surface and subsequently the air-borne noise are calculated.
The master's thesis is conducted on behalf of and in cooperation with AVL List GmbH.

Durch die Entwicklung immer leistungsstärkerer Rechner, wird die Simulation von Elektromotoren als Datenquelle zur Bestimmung ihrer Schallabstrahlung als Ergänzung zu Messungen am realen Objekt immer attraktiver. Diese Arbeit soll zur Beantwortung der Frage beitragen, inwieweit Finite-Elemente-Methode (FEM) basierte Mehrkörper-Simulations-Berechnung (MKS) und Schallabstrahlungsberechnung zur qualitativen und quantitativen Bewertung des akustischen Verhaltens von elektrischen Maschinen geeignet ist und wo weiterer Forschungsbedarf zu finden ist. Der Fokus liegt bei objektiven Kriterien wie Drehschwingungen, Körperschallpegel und Schalldruck. Dabei sollen insbesondere Ergebnisgenauigkeit, Frequenzbereich, Modellgenauigkeit und Modelltiefe betrachtet werden. Für diese Betrachtung findet ein Vergleich der Simulationsergebnisse mit vorhandenen Messdaten statt. Die Simulation erfolgt über ein SIMULINK-Modell in Kombination mit einem kommerziellen MKS-Tool. Innerhalb der Mehrkörpersimulation wird die Anregung des Gehäuses aus dem Magnetfeld berücksichtigt und über eine Rückrechnung werden zunächst der Körperschall auf der Statoroberfläche und anschließend der abgestrahlte Luftschall berechnet.
Die Masterarbeit erfolgt im Auftrag und Kooperation mit der AVL List GmbH.

Contents

1 Introduction

The distribution of vehicles with electric engines grows continuously - not least as the increased importance of environmental measures makes the use of alternatives to the traditional combustion engines more interesting and necessary.
This growing distribution of electric machines calls for detailed investigations of the different types of behavior these machines may exercise.
Compared to the noise emission of a combustion engine, the sound level of an electric machine is considerably lower. Therefore, the engine sound is much less predominant in the overall noise emission of the vehicle. Nonetheless, the tonal character of the engine sound may be perceived to be annoying as the human auditory system reacts sensitive to high frequency tonal noise.
This fact makes it interesting to examine the sound emission of electric machines.
An examination by performing measurements on the vehicles is disadvantageous as the experiments can only be run after the prototypes have been created. The testing therefore takes place relatively late in the development process when structural changes for acoustic optimization may be difficult to implement.
These disadvantages call for the use of acoustic simulation.

Up to know, the properties for most structural dynamic and acoustic simulations are based on experimental data. The complex structure of the components is not trivial to model and calls for the use of homogenization techniques.
Provided the model for the simulation can be created sufficiently predictive, the acoustic behavior of the electric machine can be calculated in earlier development stages and improvement measures can better be included.
This work strives to perform an acoustic simulation of an electric machine and its different components in order to determine predictive modeling techniques for the basic modules of the machine and to assess their potential.

After performing literature research on the topic, the experimental of the examined components is analyzed in detail to gather information about their structural behavior.
Subsequently, the finite element models are built and structural dynamic computations are performed. A series of parameter studies is performed to investigate the influence of the different properties of the components. The results of the computations are validated using experimental data.
Lastly, the sound emission of the electric machine based on a subset of structural modes is investigated.

2 Literature Research

The first step of this work is to do research on the variety of relevant topics to gain a basic understanding for the subsequent modeling, calculations and analyses.

2.1 Eigenvalue Analysis

Definition Eigenvalue and Eigenvector Eigenvalues describe properties of linear projections. An eigenvector $\boldsymbol{\phi}$ is a vector that does not change its direction when projected using a linear operator $\mathbf{A}$. The scaling factor that is applied on the eigenvector is called the eigenvalue λ [1, p. 142]. $\mathbf{E}$ is the unit matrix.

$$\mathbf{A} \cdot \boldsymbol{\phi} = \lambda \cdot \boldsymbol{\phi} \tag{2.1}$$

$$(\lambda \mathbf{E} - \mathbf{A})\, \boldsymbol{\phi} = \mathbf{0} \tag{2.2}$$

Calculation of Eigenvalues. Now the equation above is solved for the eigenvalues.

$$\det(\mathbf{A} - \lambda \mathbf{E}) = \lambda^n + \alpha_{n-1}\lambda^{n-1} + \cdots + \alpha_1 \lambda + \alpha_0 = 0 \tag{2.3}$$

Equation 2.3 shows the characteristic polynomial. Its roots are the n eigenvalues of which k are different. k may be smaller than n. For each eigenvalue one can state its algebraic multiplicity $\mu_1 \cdots \mu_k$.

Calculation of Eigenvectors. When the eigenvalues are known, the corresponding n (right) eigenvectors can be calculated using equation 2.4. The eigenvectors form an orthonormal basis.

$$(\mathbf{A} - \lambda_i \mathbf{E})\, \boldsymbol{\phi}_i = \mathbf{0} \tag{2.4}$$

Eigenvalue Decomposition. The operator A can be decomposed using the eigenvalues and their corresponding eigenvectors, given it is a square matrix (equation 2.7).

$$\boldsymbol{\Lambda} = \operatorname{diag}[\lambda_1 \lambda_2 ... \lambda_n] \tag{2.5}$$

$$\boldsymbol{\Phi} = [bm\phi_1 \boldsymbol{\phi}_2 ... \boldsymbol{\phi}_n] \tag{2.6}$$

$$\mathbf{A} = \Phi \Lambda \Phi^{-1} \tag{2.7}$$

Numerical solution of the eigenvalue problem. Directly solving for the roots of the characteristic polynomial is very numerically expensive. Therefore, algorithms have been devised that iteratively decompose the operator $\mathbf{A}$ into either lower and upper triangular matrices or into an orthogonal matrix and an upper triangular matrix. The main diagonal entries of the upper triangular matrix correspond to the eigenvalues of $\mathbf{A}$ after the last iteration [2, p. 27].

2.2 Modal Analysis

Definition Eigenfrequency and Eigenform. The modal analysis is an application of the eigenvalue analysis for oscillating systems. The eigenfrequency is the oscillating frequency of a singularly excited system. It corresponds to the roots of the eigenvalues of the system matrix [2, p. 56].

The eigenform (also: mode shape) describes the stationary properties of a wave regarding its energy distribution in different directions. They are defined by the eigenvector ϕ of the system matrix.
When eigenvalues occur multiple times this indicates that the same mode shapes occur multiple times. This happens when the excited structure is symmetrical. When the symmetry is slightly broken, those identical eigenfrequencies drift apart to some degree, the resonance peak in the frequency response function is split.
When an eigenvalue equals zero this is an indicator for rigid body vibration modes, which means the system is not grounded physically.

Modal Analysis of a single degree of freedom system. The single degree of freedom (SDoF) system consists of three elements: the mass m, the spring with stiffness k and the damper with either viscous damping c or structural damping h. These elements are combined in the equation of motion (2.8) to describe the system.

$$m\ddot{x}(t) + c\dot{x}(t) + kx(t) = f(t) \tag{2.8}$$

This system is excited with a harmonic force $f(t) = F(\omega) \cdot e^{j\omega t}$. The response of the system is a harmonic function as well: $x(t) = X(\omega) \cdot e^{j\omega t}$.
In the case of zero damping $X(\omega)$ is real, otherwise it is a complex amplitude.
The frequency response function describes the relation between system response and system excitation and is obtained by transformation of the equation of motion into the Laplace domain and dividing by the excitation. When the response is expressed in terms of displacement, this frequency response function is called receptance $\alpha(\omega)$ and is displayed in equations 2.9 and 2.10.

$$\text{For viscous damping:} \qquad \alpha(\omega) = \frac{X(\omega)}{F(\omega)} = \frac{1}{k - \omega^2 \cdot m + j\omega c} \tag{2.9}$$

$$\text{For structural damping:} \qquad \alpha(\omega) = \frac{X(\omega)}{F(\omega)} = \frac{1}{k - \omega^2 \cdot m + jh} \tag{2.10}$$

The frequency response function can also be expressed in terms of velocity $\dot{X}(\omega) = j\omega \cdot X(\omega)$ or acceleration $\ddot{X}(\omega) = -\omega^2 \cdot X(\omega)$.
From the frequency response function the resonance frequency position and the modal damping can be derived.
The modal analysis is performed by calculating a curve fit that consists of the superposition of multiple SDoF systems (= harmonic oscillators) from which the resonance frequencies, modal dampings and mode shapes are calculated [2, pp. 79].

Modal Assurance Criterion. The modal assurance criterion (MAC) is a measure to assess how well different mode shapes match. It calculates the correlation between two different eigenvectors (equation 2.11). This criterion can be used to compare the mode shapes from simulation ($\boldsymbol{\phi}_{i,S}$) and measurement ($\boldsymbol{\phi}_{i,M}$) and is therefore a mean of validating the Finite-Element (FE) calculation.

$$\mathrm{MAC} = \frac{|\boldsymbol{\phi}_{i,M}^T \boldsymbol{\phi}_{i,S}^*|^2}{\left(\boldsymbol{\phi}_{i,M}^T \boldsymbol{\phi}_{i,M}^*\right)\left(\boldsymbol{\phi}_{i,S}^T \boldsymbol{\phi}_{i,S}^*\right)} \tag{2.11}$$

For the comparison each eigenvector of measurement and simulation are compared to each other. This way a matrix is created that shows how well the eigenforms match. A MAC value between 0.7 and 1 is considered a good match. For a good concordance between measurement and simulation, the MAC values on the main diagonal of the matrix should be in this range. Moreover, off diagonal elements should be close to zero. In case that the eigenvectors are complex (which is the case when damping effects are taken into account), the complex conjugation has to be regarded [3, p. 16].

2.3 Mechanics of Materials

Young's modulus. The Young's modulus E, also known as elastic modulus is a material property which describes the relation between stress σ_{el} and strain ε_{el} (equation 2.12). It is a measure for the material's stiffness and its unit is usually MPa or GPa (unit of pressure) [4, p. 77].

$$E = \frac{\Delta\sigma_{el}}{\Delta\varepsilon_{el}} \tag{2.12}$$

Poisson's ratio. If a body is exposed to a tensile load F, it gets longer and thinner. This is illustrated in figure 2.1. The light blue body is the undeformed one, the dark blue one is the one exposed to the tensile load. The Poisson's ratio ν is a material property that gives the negative relation between the relative deviation in thickness $\frac{\Delta d}{d}$ (perpendicular to load direction) to the relative deviation in length $\frac{\Delta l}{l}$ (parallel to load direction) as can be seen in equations 2.13 and 2.14. The Poisson's ratio is without unit [4, p. 79] [5].

$$\nu = -\frac{\frac{\Delta d}{d}}{\frac{\Delta l}{l}} \tag{2.13}$$

$$\nu_{zx} = -\frac{\varepsilon_{xx}}{\varepsilon_{zz}} \tag{2.14}$$

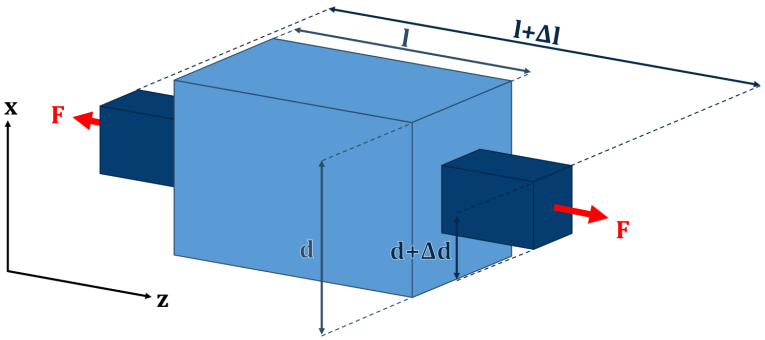

Figure 2.1 – Illustration Poisson's ratio

Shear modulus. The shear modulus G is a material property that describes the relation between shear stress τ and shear strain γ (equations 2.15 and 2.16). These types of stress and strain are illustrated in figure 2.2.
The shear modulus can also be calculated using the Young's modulus and the Poisson's ratio as can be seen in equation 2.17.
The shear modulus' derived unit is MPa (unit of pressure) [4, pp. 81] [6].

$$G = \frac{\tau}{\gamma} = \frac{\frac{F}{A}}{\tan(\varphi)} = \\ = \frac{\frac{F}{A}}{\frac{\Delta z}{l}} = \frac{F \cdot l}{A \Delta z} \tag{2.15}$$

$$G_{zx} = \frac{\tau_{zx}}{\gamma_{zx}} \tag{2.16}$$

$$G = \frac{E}{2(1+\nu)} \tag{2.17}$$

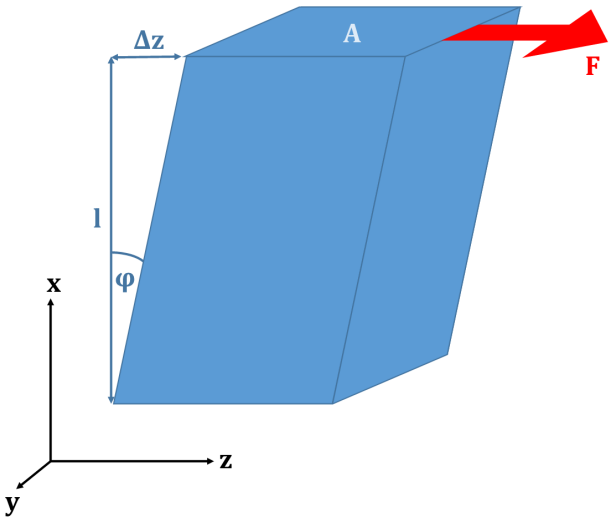

Figure 2.2 – Illustration shear modulus

2.4 Electric Machines

Permanent magnet excited synchronous machine. The object of investigation is a certain type of electric machine, a permanent magnet excited synchronous machine (PMSM). It consists of different stationary and rotating parts. In the following its components will be explained.

Stator. As the name suggests the stator builds the stationary part of the machine. Its core consists of laminated steel sheets. These thin ($< 1\,\mu m$) steel sheets are made of specific electric steel and the individual sheets are insulated using a synthetic resin varnish. In the processing the sheets are first coated with the varnish on both sides and then baked together under pressure until the desired thickness of the package is accomplished.
The package exhibits rotational symmetry and is made from a yoke on the outside and teeth on the inside.
The slots in between the teeth are filled with windings usually made from copper. The windings are wound around the teeth, the part of the winding outside the slot is called end winding. To prevent a short circuit between the windings and the grounded iron core an insulating paper is positioned between them. A schematic cross section of the stator core and a sketch of the slot filling are displayed in figure 2.3.

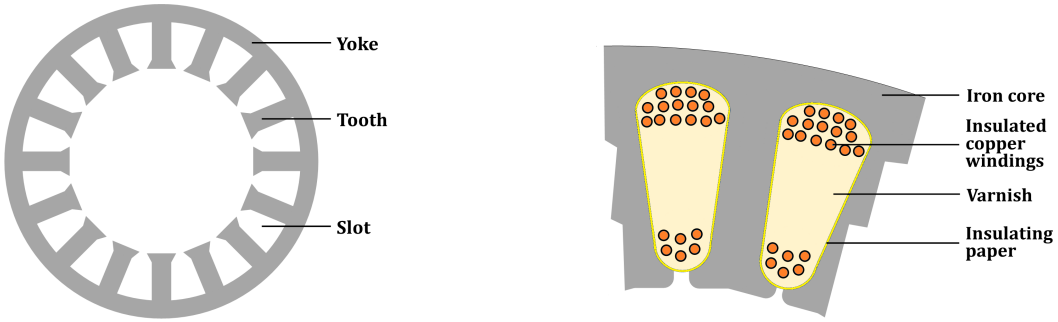

(a) Sketch of stator iron core cross section

(b) Sketch of stator slot cross section

Figure 2.3 – Cross sections of the stator

Rotor. The rotor is the rotating part of the electric machine. Its core is made of steel sheets as well. On its surface permanent magnets are glued on and fixated using a band. Between rotor and stator there is a small air gap.
When appropriate current flows through the stator windings a rotating magnet field is created which moves the rotor [7, pp. 598]. The rotor has only little influence on eigenfrequencies [8] and is therefore excluded from the subsequent analyses.

Housing. The chassis keeps the components together and ensures their axial alignment [9, p. 11]. The displacement of the surface of the chassis is the main source of airborne noise created by the machine [10]. Due to weight reasons the chassis is made of aluminum.

2.5 Modeling of Electric Machines

Several publications have dealt with the modeling of the components of electric machines. For the simulation, appropriate stiffness properties have to be applied to the different

parts as those influence the resulting sound power [11].
As the components are quite complex, homogenized material settings are usually used to reduce computation time [12]. Often these homogenized settings are determined from experimental data [10–17].
This work strives to achieve predictability, therefore analytical homogenization techniques are used to determine the material properties for the different components.

Modeling of the laminated sheets The base material of the electric machine consists of thin layers of iron sheets that are baked together using a synthetic resin. Therefore, it consists of alternating layers of iron and varnish. The two different materials have significantly different properties regarding density ρ, Young's modulus E, Poisson's ratio ν, and shear modulus G. The arrangement in layers leads to different mechanical behavior in axial direction (index z) and perpendicular (index p) to it. This is called transverse isotropy which is a special case of orthotropy.
In some publications the transverse isotropic behavior is neglected and the sheets are modeled isotropically [18], but it has been shown, that the isotropic modeling is not sufficiently precise [19, 20].
Therefore, transverse isotropic and orthotropic modeling has been established in the simulation of electric machines [8, 10–14, 16, 17]. The basic idea here is to model the layers as a serial connection of springs in axial direction (z axis in figures), respectively a parallel connection of springs in perpendicular direction (axes p_1 and p_2 in figures) in order to describe their Young's Modulus in the different directions. The axes p_1 and p_2 are interchangeable and merged in index p in the following equations. This modelling method is called rule of mixtures and illustrated in figure 2.4. The formulas used for the calculation of the different parameters are listed below. ϕ_{St} is the percentage of steel sheets taken of the whole components volume. The rest of the volume is filled with varnish [21].

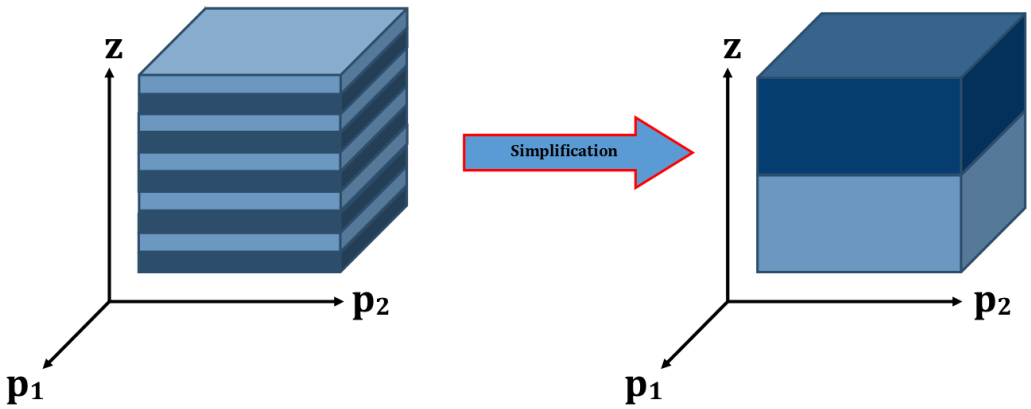

Figure 2.4 – Illustration of the structural model for laminated sheets

$$\rho = \rho_f \phi_{St} + \rho_m (1 - \phi_{St}) \tag{2.18}$$

$$E_z = \left(\frac{\phi_{St}}{E_f} + \frac{1 - \phi_{St}}{E_m} \right)^{-1} \tag{2.19}$$

$$E_p = E_f \phi_{St} + E_m (1 - \phi_{St}) \tag{2.20}$$

$$\nu_p = \nu_f \phi_{St} + \nu_m (1 - \phi_{St}) \tag{2.21}$$

$$\nu_{zp} = \nu_p \frac{E_z}{E_p} \tag{2.22}$$

$$G_p = \frac{E_p}{2 \cdot (1 + \nu_p)} \tag{2.23}$$

$$G_{zp} = \frac{G_m G_f}{G_m \phi_{St} + G_f (1 - \phi_{St})} \tag{2.24}$$

Modeling of the impregnated windings [16] and [22] only consider the windings as an additional mass without the respective stiffness properties. But several publications have proven that the windings along with their stiffness properties have a considerable influence on the vibration behavior [14, 18, 23–28]. Only in the case of no impregnation and therefore a missing elastic coupling the neglecting of the windings' stiffness behavior is tolerable [23].
A homogenized transverse isotropic model of the windings is used in [14, 17, 24, 29]. The equations 2.18 to 2.24 do not suffice to describe the mechanical behaviour of the impregnated copper windings that run through the slots of the stator. The equations above have to be extended in order to model the copper windings [30].
While the windings can still be modelled as a parallel connection of springs in the direction of the wires (equation 2.19), perpendicular of that direction there is a combination of a parallel and a serial connection. The used equations are based on the method of Halpin-Tsai which is an empirical extension of the rule of mixtures. [9] investigated the reliability of this homogenization method and concluded that the accordance to the measured stiffness values of impregnated windings was sufficiently good.

The indices in the following equations denote the material properties of windings (w) and insulation (i) in axial direction θ and in radial directions z and r [1] as illustrated in figure 2.5.

The Young's moduli of winding and insulation material, and their respective volume ratios, the homogenized values for the Young's modulus in r and z direction can be calculated (equations 2.26 and 2.27) using the adjustment factor ξ_E. This factor weights the relation between parallel and serial connection and allow for adjustment to the measurement.

1. In [30] a different arrangement of the coils was displayed which called for the use of cylindrical coordinates. Although the model used in this thesis is altered, the axes denominations have been adopted from literature.

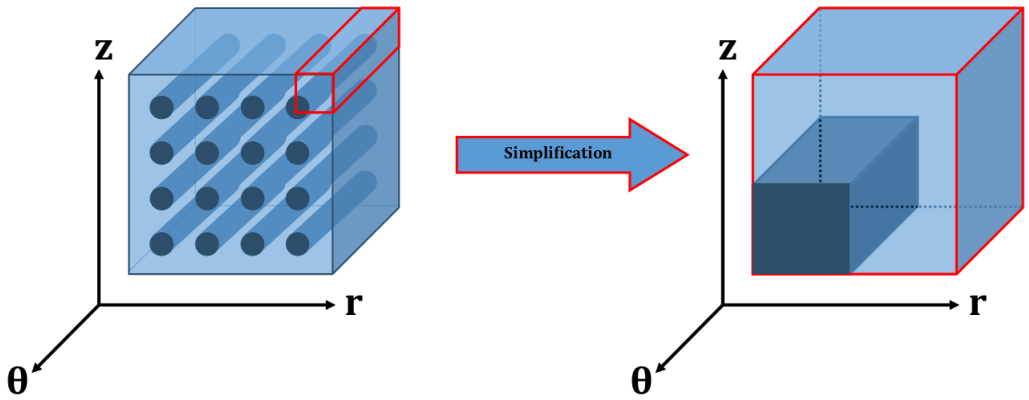

Figure 2.5 – Illustration of the structural model for sealed windings

$$\eta_E = \frac{E_w - E_i}{E_w + \xi_E \cdot E_i} \tag{2.25}$$

$$E_z = \left(\phi_r \cdot \frac{1 + \xi_E \cdot \eta_E \cdot \phi_z}{1 - \eta_E \cdot \phi_z} + (1 - \phi_r)\right) \cdot E_i \tag{2.26}$$

$$E_r = \left(\phi_z \cdot \frac{1 + \xi_E \cdot \eta_E \cdot \phi_r}{1 - \eta_E \cdot \phi_r} + (1 - \phi_z)\right) \cdot E_i \tag{2.27}$$

In analogy to the calculation of the Young's modulus, the shear modulus is calculated as can be seen in equation 2.29.

$$\eta_G = \frac{G_w - G_i}{G_w + \xi_G \cdot G_i} \tag{2.28}$$

$$G_{rz} = \frac{1 + \xi_G \cdot \eta_G \cdot \phi_r \cdot \phi_z}{1 - \eta_G \cdot \phi_r \cdot \phi_z} \cdot G_i \tag{2.29}$$

[31] provides values for the adjustment factors $\xi_E = 2$ and $\xi_G = 1$.

This homogenization method also provides the means for calculating the Poisson's ratios in the different directions of space. They are listed in equations 2.31 to 2.33.

$$\mu = \frac{(E_w + \xi_E E_i) + \xi_E \phi_r (E_w - E_i)}{(E_w + \xi_E E_i) - \phi_r (E_w - E_i)} \tag{2.30}$$

$$\nu_{\theta z} = (1 - \phi_z)\nu_i + \phi_z \frac{\phi_r \nu_w E_w + (1 - \phi_r)\nu_i E_i}{\phi_r E_w + (1 - \phi_r) E_i} \tag{2.31}$$

$$\nu_{\theta r} = (1 - \phi_r)\nu_i + \phi_r \frac{\phi_z \nu_w E_w + (1 - \phi_z)\nu_i E_i}{\phi_z E_w + (1 - \phi_z) E_i} \tag{2.32}$$

$$\nu_{rz} = \frac{\nu_i (1 - \phi_r)[\phi_z E_w + (1 - \phi_z) E_i] + \mu \phi_r E_i [\phi_z \nu_w + (1 - \phi_z)\nu_i]}{[(\mu \phi_r + (1 - \phi_r)] \{\phi_r E_i + [1 - \phi_r][\phi_z E_w + (1 - \phi_z) E_i]\}} \tag{2.33}$$

2.6 Wave Based Technique

The Wave Based Technique (WBT) is a method for the numerical solution of partial differential equations. It can be used for structural, acoustic and coupled vibroacoustic problems.
The application of this method for the sound radiation simulation of a combustion engine has been validated up to 3 kHz in [32].

Problem description The emitted sound pressure field in a fluid is determined by the Helmholtz equation (equation 2.34).

$$\nabla^2 p(\mathbf{r}) + k^2 p(\mathbf{r}) = -f(\mathbf{r}) \tag{2.34}$$

This applies only under the following conditions.
- — linear system
- — inviscid fluid (no resistance to shear stress)
- — adiabatic process (no transfer of heat or matter)

The model for the calculation is determined by the physical boundary Γ of the noise emitting object and the fluid domain Ω outside the boundary. An illustration can be seen in figure 2.6.

The physical boundary consists of three separate contributions (equation 2.35):

Γ_p ... pressure boundary condition
Γ_v ... normal velocity boundary condition
Γ_Z ... normal impedance boundary condition

$$\Gamma = \Gamma_p \cup \Gamma_v \cup \Gamma_Z \tag{2.35}$$

The fluid domain is partitioned into a bounded domain Ω_B bordering Γ and an unbounded domain Ω_U extending to infinity. They are separated by the artificial boundary Γ_T at the truncation radius r_T.

The bounded domain is divided into several subdomains. Adjacent bounded subdomains share a common coupling interface Γ_I which determines - along with the respective

pressure, velocity and impedance boundary conditions - the boundary of the individual subdomains.
The nodal velocities of the structural mesh are mapped onto Gauss quadrature points on the boundary using interpolation functions. [32]

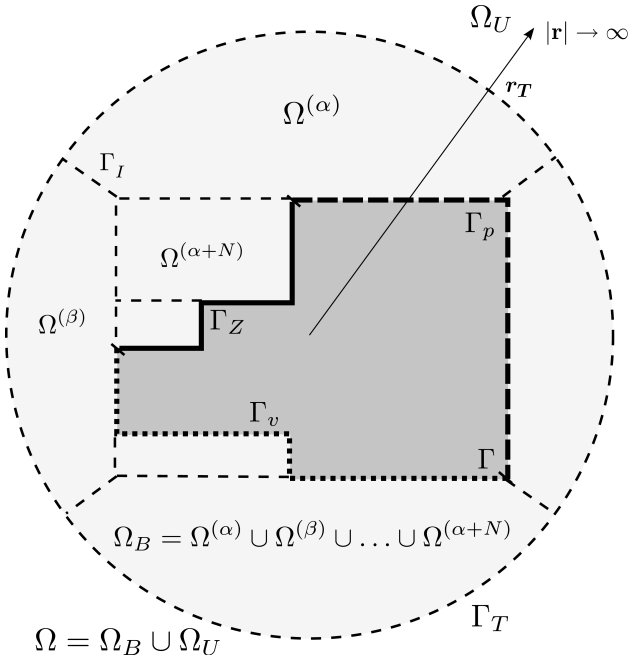

Figure 2.6 – Model of the exterior acoustic problem (adapted from [33])

To approximate the solution of the inhomogeneous Helmholtz equation, trial functions that fulfill the homogeneous Helmholtz equation are used.
The acoustic pressure field is approximated using the pressure expansion presented in equation 2.36.

$$p^{(\alpha)}(\mathbf{r}) \approx \hat{p}^{(\alpha)}(\mathbf{r}) = \sum_{w=1}^{n_w^{(\alpha)}} p_w^{(\alpha)} \phi_w^{(\alpha)}(\mathbf{r}) \qquad \mathbf{r}\epsilon\Omega_B^{(\alpha)} \tag{2.36}$$

The used trial functions $\phi_w^{(\alpha)}(\mathbf{r})$ differ between the bounded and the unbounded domain.

Solution within bounded subdomains The solution within a bounded subdomain is calculated using the wave sets $\phi_{w_r}^{(\alpha)}$, $\phi_{w_s}^{(\alpha)}$ and $\phi_{w_t}^{(\alpha)}$.

$$\phi_w^{(\alpha)}(\mathbf{r}) = \begin{cases} \phi_{w_r}^{(\alpha)}(\mathbf{r}_{xyz}) = \cos\left(k_{x_{w_r}}^{(\alpha)} x\right) \cos\left(k_{y_{w_r}}^{(\alpha)} y\right) \exp^{-jk_{z_{w_r}}^{(\alpha)} z} \\ \phi_{w_s}^{(\alpha)}(\mathbf{r}_{xyz}) = \cos\left(k_{x_{w_s}}^{(\alpha)} x\right) \exp^{-jk_{y_{w_s}}^{(\alpha)} y} \cos\left(k_{z_{w_s}}^{(\alpha)} z\right) \\ \phi_{w_t}^{(\alpha)}(\mathbf{r}_{xyz}) = \exp^{-jk_{x_{w_t}}^{(\alpha)} x} \cos\left(k_{y_{w_t}}^{(\alpha)} y\right) \cos\left(k_{z_{w_t}}^{(\alpha)} z\right) \end{cases} \tag{2.37}$$

The wave numbers corresponding to these wave sets are defined to satisfy the homogeneous Helmholtz equation (equations 2.38 to 2.40).

$$\left(k_{x_{w_r}}^{(\alpha)}, k_{y_{w_r}}^{(\alpha)}, k_{z_{w_r}}^{(\alpha)}\right) = \left(\frac{n_{x_r}^{(\alpha)}\pi}{L_x^{(\alpha)}}, \frac{n_{y_r}^{(\alpha)}\pi}{L_y^{(\alpha)}}, \pm\sqrt{k^2 - \left(k_{x_{w_r}}^{(\alpha)}\right)^2 - \left(k_{y_{w_r}}^{(\alpha)}\right)^2}\right) \tag{2.38}$$

$$\left(k_{x_{w_s}}^{(\alpha)}, k_{y_{w_s}}^{(\alpha)}, k_{z_{w_s}}^{(\alpha)}\right) = \left(\frac{n_{x_s}^{(\alpha)}\pi}{L_x^{(\alpha)}}, \pm\sqrt{k^2 - \left(k_{y_{w_s}}^{(\alpha)}\right)^2 - \left(k_{z_{w_s}}^{(\alpha)}\right)^2}, \frac{n_{z_s}^{(\alpha)}\pi}{L_z^{(\alpha)}}\right) \tag{2.39}$$

$$\left(k_{x_{w_t}}^{(\alpha)}, k_{y_{w_t}}^{(\alpha)}, k_{z_{w_t}}^{(\alpha)}\right) = \left(\pm\sqrt{k^2 - \left(k_{x_{w_t}}^{(\alpha)}\right)^2 - \left(k_{z_{w_t}}^{(\alpha)}\right)^2}, \frac{n_{y_t}^{(\alpha)}\pi}{L_y^{(\alpha)}}, \frac{n_{z_t}^{(\alpha)}\pi}{L_z^{(\alpha)}}\right) \tag{2.40}$$

The dimensions of the subdomain $\Omega^{(\alpha)}$ are considered in $L_y^{(\alpha)}$,$L_y^{(\alpha)}$ and $L_y^{(\alpha)}$.
$n_{x_i}^{(\alpha)}$, $n_{y_i}^{(\alpha)}$ and $n_{z_i}^{(\alpha)}$ (where $i = r, s, t$) refer to the degrees of freedom of the truncated, finite-sized computational model.

Solution within the unbounded domain Within the unbounded domain, the acoustic solution has to satisfy the Helmholtz equation and the Sommerfeld-radiation condition. The Sommerfeld conditions states that there are no sources of energy (e. g. because of reflections) at infinity [32].

The radiation function expressed in terms of spherical coordinates can be seen in 2.41.

$$p^{(\Omega_U)}(r, \phi, \theta) = \sum_{l=0}^{N_{RF}} \sum_{m=-l}^{l} p_{lm} h_l(kr) Y_{lm}(\phi, \theta) \tag{2.41}$$

$h_l(kr)$ denotes the spherical Hankel functions, $Y_{lm}(\phi, \theta)$ is the spherical harmonics.

For a larger truncation radius, more wave functions are required in the bounded and unbounded regions.

Application of boundary conditions Apart from the boundary conditions, continuity conditions have to be applied at the coupling interfaces between adjacent subdomains. This is realized by an impedance coupling.
The boundary and continuity conditions are transformed into residual error functions.

They describe the error between the pressure approximation and the boundary conditions.
The residuals are orthogonalized using the Galerkin weighting which leads to system of linear equations. The corresponding system matrix is dense, non-symmetric, complex-valued and frequency dependent [33].

3 Modal Analysis

The final goal of the simulation is to lose the necessity for expensive measurements. The advantage of simulations is that they can be performed in earlier stages of development and also design changes can be examined more easily. But in order to replace the measurement, it has to be made sure that the simulation mirrors the reality. Therefore the simulation has to be validated using measurement results.
For this thesis measurement results from two different electric machines including different components have been provided. The first examined machine in the following is the generator of a Range Extender. The surveyed components were the pure lamination stack (made just of sheets and varnish) and the stator. For the second machine (HM 132) data from the stator as well as the whole electric machine are available.

3.1 Analysis Process

The Frequency Response Functions (FRFs) are available from the measurements. These FRFs are used to perform the modal analysis using the software tool ME'scope [34]. After the modal analysis the mode frequencies, the modal damping, and the mode shapes could be exported for detailed analysis in Octave/MATLAB. The analysis in Octave includes the animated display of the mode shapes, calculation of the Modal Assurance Criterion with subsequent comparison of resonance frequencies, and display of coherence, damping, and the FRFs.

3.2 Lamination Stack (Range Extender)

The first object of examination are five packages of laminated sheets. These represent the base material from which the electric machine is built. The main purpose of this investigation is to find out how to model the lamination stack layers by comparing the simulation to the measurement. Before this comparison can be done, the measurement results have to be analyzed in detail.

3.2.1 Measurement Objects

A sketch of the package can be seen in figure 3.1.

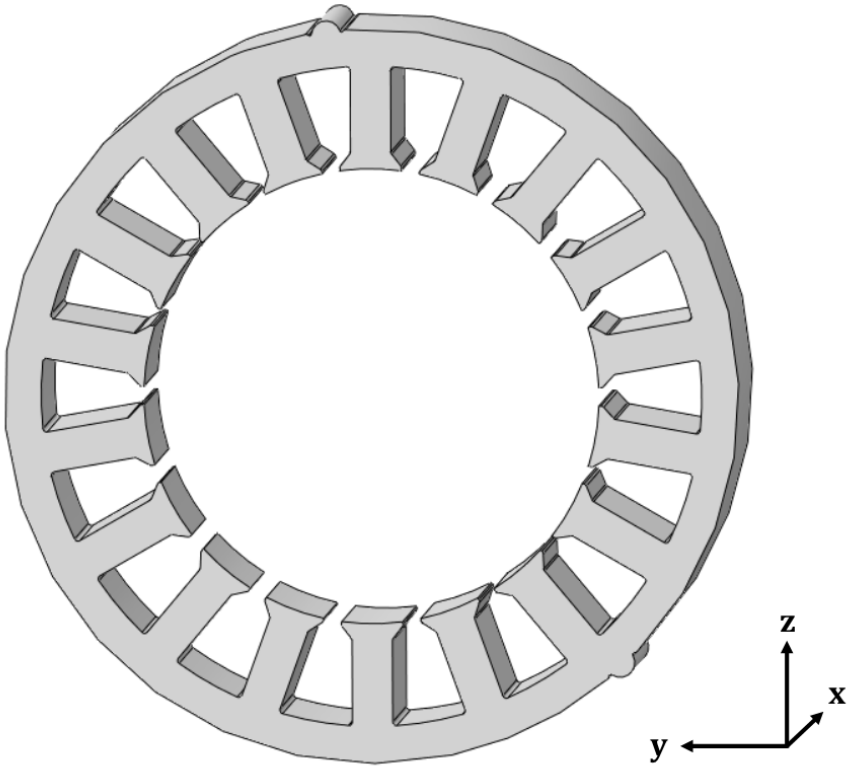

Figure 3.1 – Geometry of the lamination stack

The five packages are not exactly identical, there are two groups of packages. The production variance can already be seen in the package thickness and the number of layers that are still within the the specified tolerance (table 3.1).

Packages	Thickness	No. of Sheets
No. 1/2	50.2 mm	144
No. 3/4/5	50.0 mm	143

Table 3.1 – Material data lamination stack

3.2.2 Measurement Set-up

During the measurement the packages were hung on elastic ropes to ensure a free oscillation.
The excitation was performed using an impulse hammer. The packages were struck in different directions in order to see whether the same modes are excited when the excitation comes from a different direction. The excitation directions were X,Y,Z and XYZ (aslant so that all three directions of space are excited as equally as possible).

For one of the packages the excitation was performed also on three different force levels in order to examine the linearity of the vibration behavior. These three levels are denoted by (+) for the lowest excitation force, (++) for the medium excitation force and (+++) for the highest excitation force in the following.

3.2.3 Coherence

The coherence between two signals provides information whether their amplitudes change in the same manner apart from a constant shift in phase [35]. The higher the coherence between excitation signal and sensor signal, the better the measurement quality.
The coherence data include the coherences of every single of the 54 measurement points for one measurement run. To simplify the analysis, the mean over all these measurement points for each run was calculated and plotted.
In the frequency range where the coherence lies above the value of 0.9 (marked by the horizontal red line in the figures), the measurement data is deemed reliable. For the display the whole measurement frequency range from 0 Hz to 12.8 kHz is chosen. The ordinate is limited to the range between 0.6 and 1 as only the signal parts above the threshold are of interest.

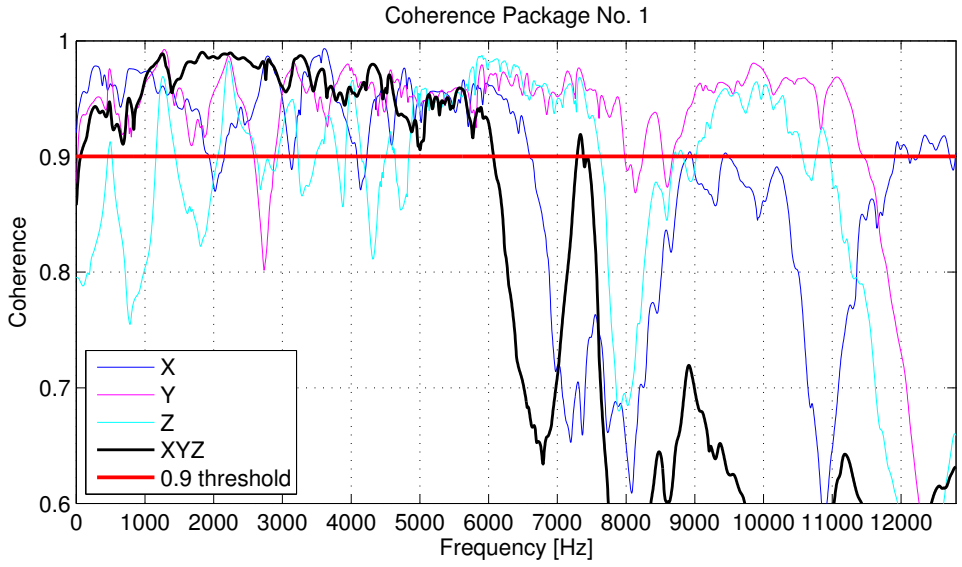

Figure 3.2 – Coherence Package No. 1

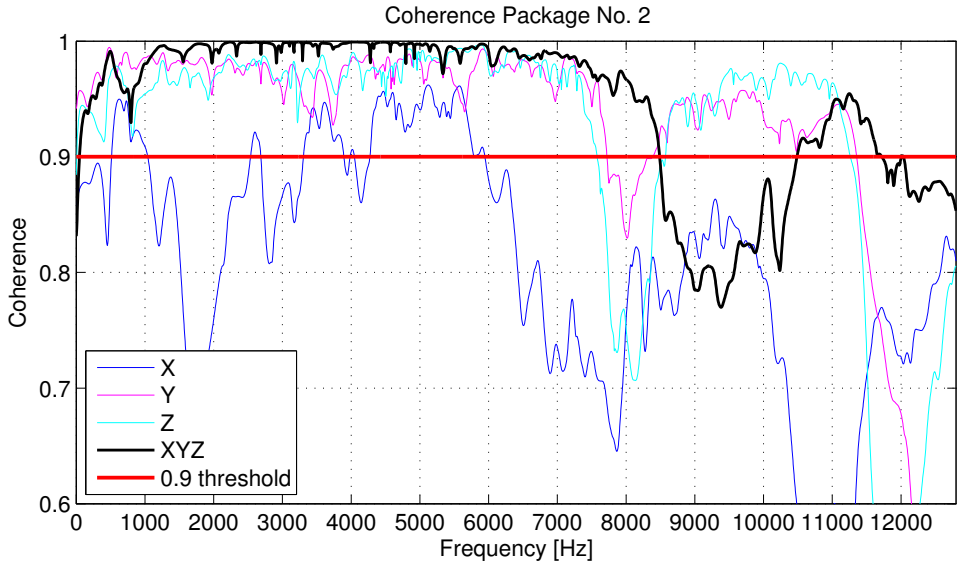

Figure 3.3 – Coherence Package No. 2

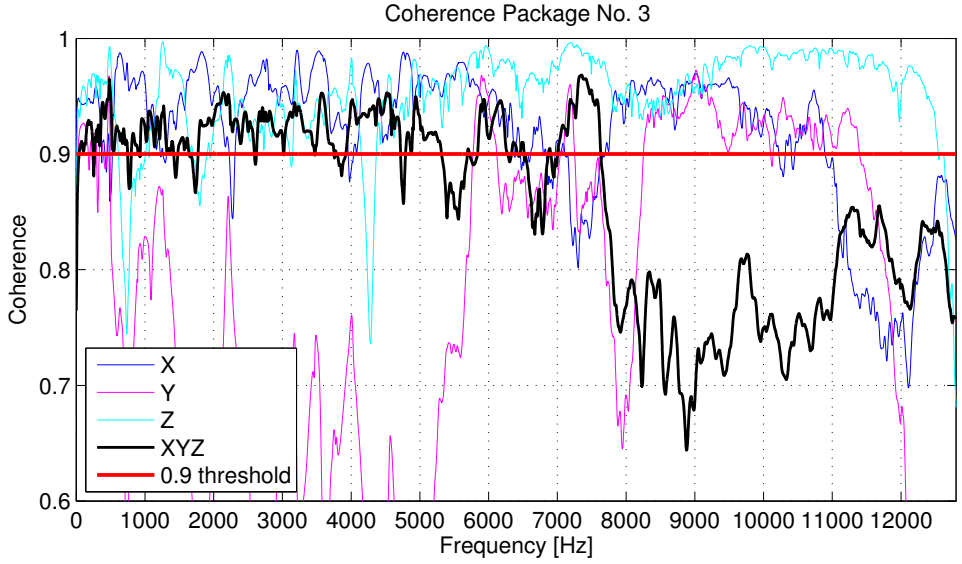

Figure 3.4 – Coherence Package No. 3

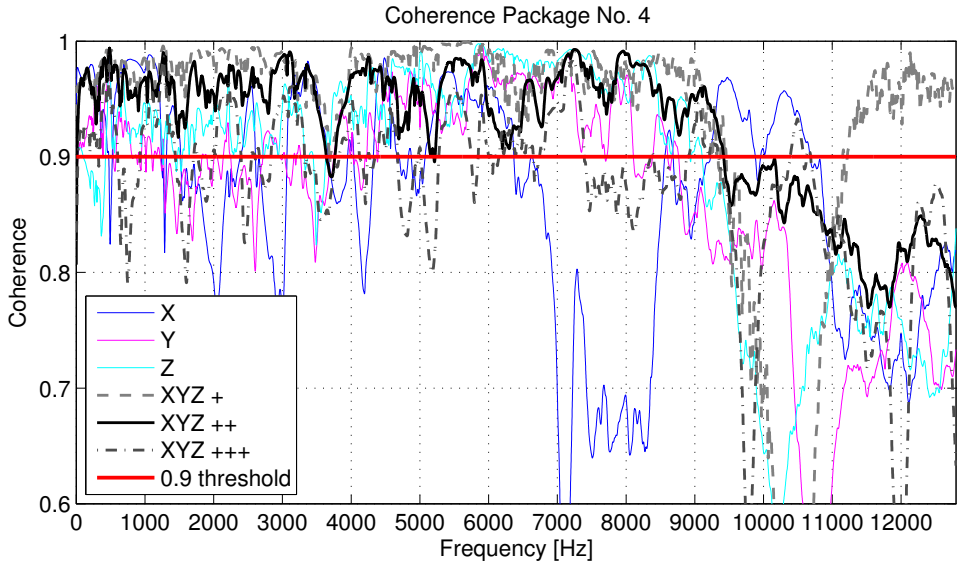

Figure 3.5 – Coherence Package No. 4

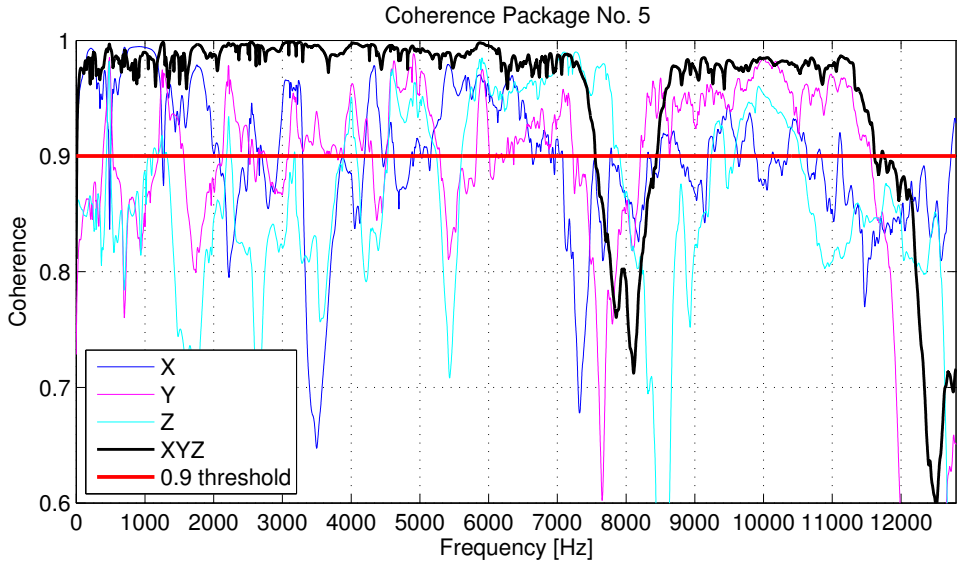

Figure 3.6 – Coherence Package No. 5

For the different packages and the different excitation directions the frequency range of coherence above 0.9 varies a lot. For example the coherence lies generally below the other packages for Package No.3 (figure 3.4) . A possible explanation for that is, that the excitation force was low in this measurement compared to the other measurement runs. In general the excitation forces vary greatly from measurement run to measurement run, as can be seen in table 3.2. This leads to a limited comparability in the analysis process and calls for measurement methods that ensure a more constant excitation force level. The issue of the varying excitation force levels will be broached in the following sections.

Package	Maximum Force (XYZ)
No. 1	0.5 N
No. 2	0.9 N
No. 3	0.2 N
No. 4+	0.05 N
No. 4++	0.1 N
No. 4+++	0.2 N
No. 5	0.15 N

Table 3.2 – Approximate maximum force excitation for each of the packages for the XYZ excitation measurement runs

Table 3.3 shows the approximated upper limit of the frequency range in which the coherence lies above 0.9 for the measurements with XYZ excitation direction.

Package	Coherence > 0.9
No. 1	6000 Hz
No. 2	8500 Hz
No. 3	7600 Hz
No. 4	9300 Hz
No. 5	7500 Hz

Table 3.3 – Approximate frequency range in which the coherence of the XYZ-measurement lies above 0.9

For most of the packages the coherence is above 0.9 up to 7.5 kHz. Therefore, the following analysis is limited to the frequency range from 10 Hz to 7500 Hz. The lower limit of 10 Hz is chosen, because this way rigid body movement can be omitted.

3.2.4 Quality of Sensor Positioning

The next question is whether the number and placement of the sensors can resolve all the modes in the frequency range of interest. Because of the finite number of sensors the spatial resolution is limited.
In order to determine the quality of the sensor locations to appropriately resolve the mode shapes, support by simulation of the package is necessary. In this simulation an eigenvalue extraction using nominal material parameters based on data sheet values was performed - these parameters will be explained in detail in 4.2.3.
A characteristic of the eigenvalue extraction is that all of the mode shapes that correspond to these eigenvalues are orthogonal. Therefore, if the mode shapes are compared with themselves using the MAC (AutoMAC), the result would be the unit matrix.
But this only applies, when one takes into account all 183660 nodes belonging to the FE-model. When one picks out a smaller set of nodes - which happens by looking only

at the sensor positions - the eigenvectors are not perfectly orthogonal any more. When too few examination points are chosen and the MAC does not resemble the unit matrix anymore, there is the danger that the different mode shapes can no longer be distinguished - the spatial resolution is too low.
Therefore, the AutoMAC is a measure for the quality of the sensor positioning.

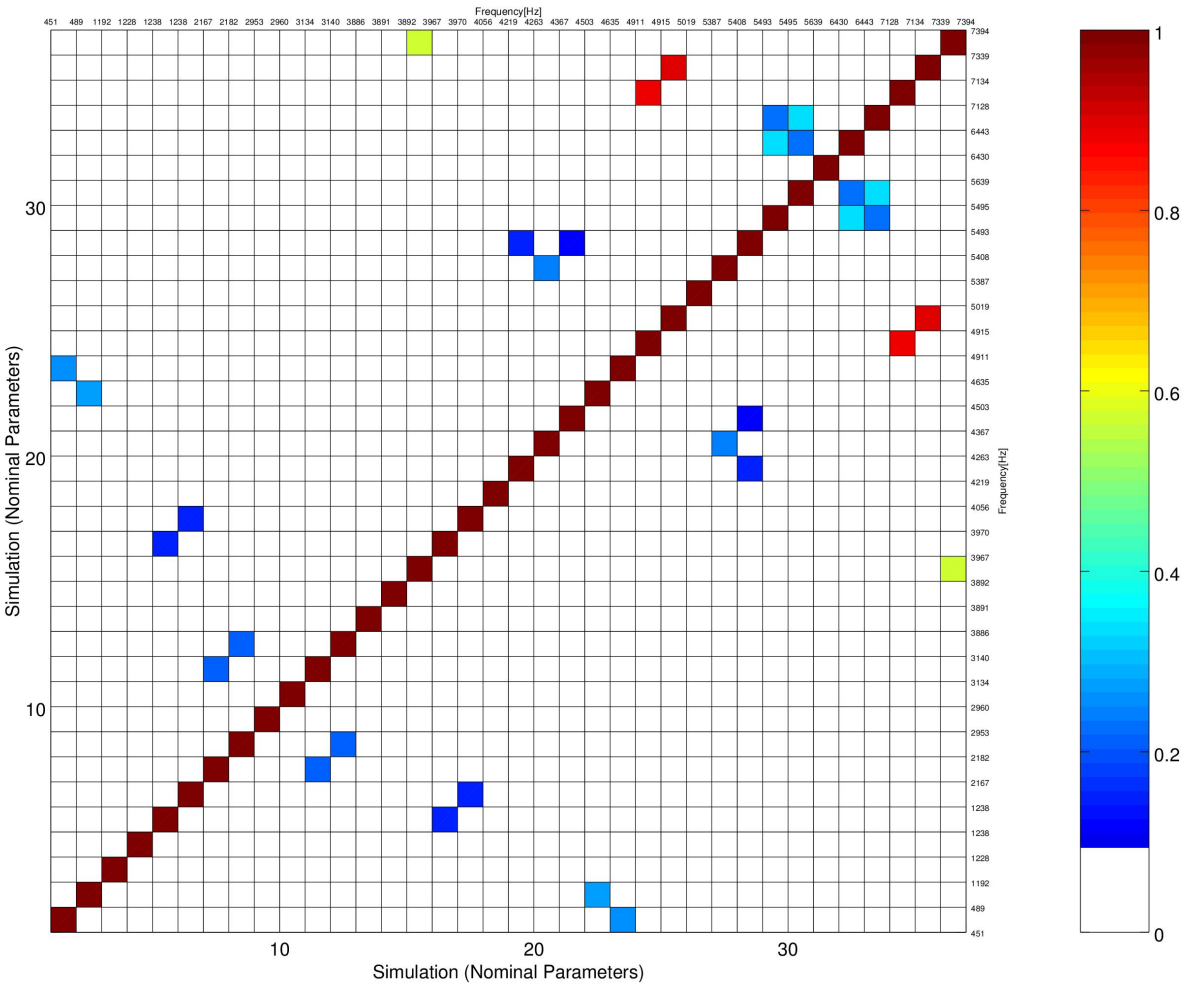

Figure 3.7 – AutoMAC of the simulated lamination stack using the nominal parameters

Figure 3.7 shows the AutoMAC for the sensors positioned on the lamination stacks. Each field of the matrix contains the MAC value for one pair of modes. The secondary axes name the respective eigenfrequencies, starting at the first mode at 451 Hz and ending at the highest mode within the frequency band of sufficiently good coherence at 7394 Hz. The AutoMAC is indeed close to the unit matrix, there are very few higher values off the main diagonal. Merely a pair of modes at 7.1 kHz can not be resolved well anymore. In general it can be said that the selection of measurement points is appropriate and

trustworthy.

3.2.5 Directions of Excitation

The different directions of excitation were compared using the MAC calculation. This comparison is intended to show how well the different modes are excited when exciting the structure in different directions of space.
There is not much agreement between the single excitation directions (figure 3.8). Not even the comparison between the single excitation directions X,Y,Z and the combined excitation XYZ showed considerable agreement (figure 3.9). This poor performance does not fulfill the expectations.

Because of the structure's symmetry there usually are two manifestations of the shapes that look the same but are rotated differently in space. A problem in the determination of mode shapes using the modal analysis software is that only one manifestation of the mode shape is output. Due to the different excitation directions, the respective manifestations might be pronounced with varying intensity and therefore the shape output differs. The different manifestations lead to a poor MAC result for those shapes.
Yet the overall MAC result in the comparison of excitation directions should be better. The reason for the poor result is not fully settled.

Nonetheless, for the further analysis the measurement data from the XYZ measurement runs were chosen, as in this case there is the highest probability that all possible modes are excited.

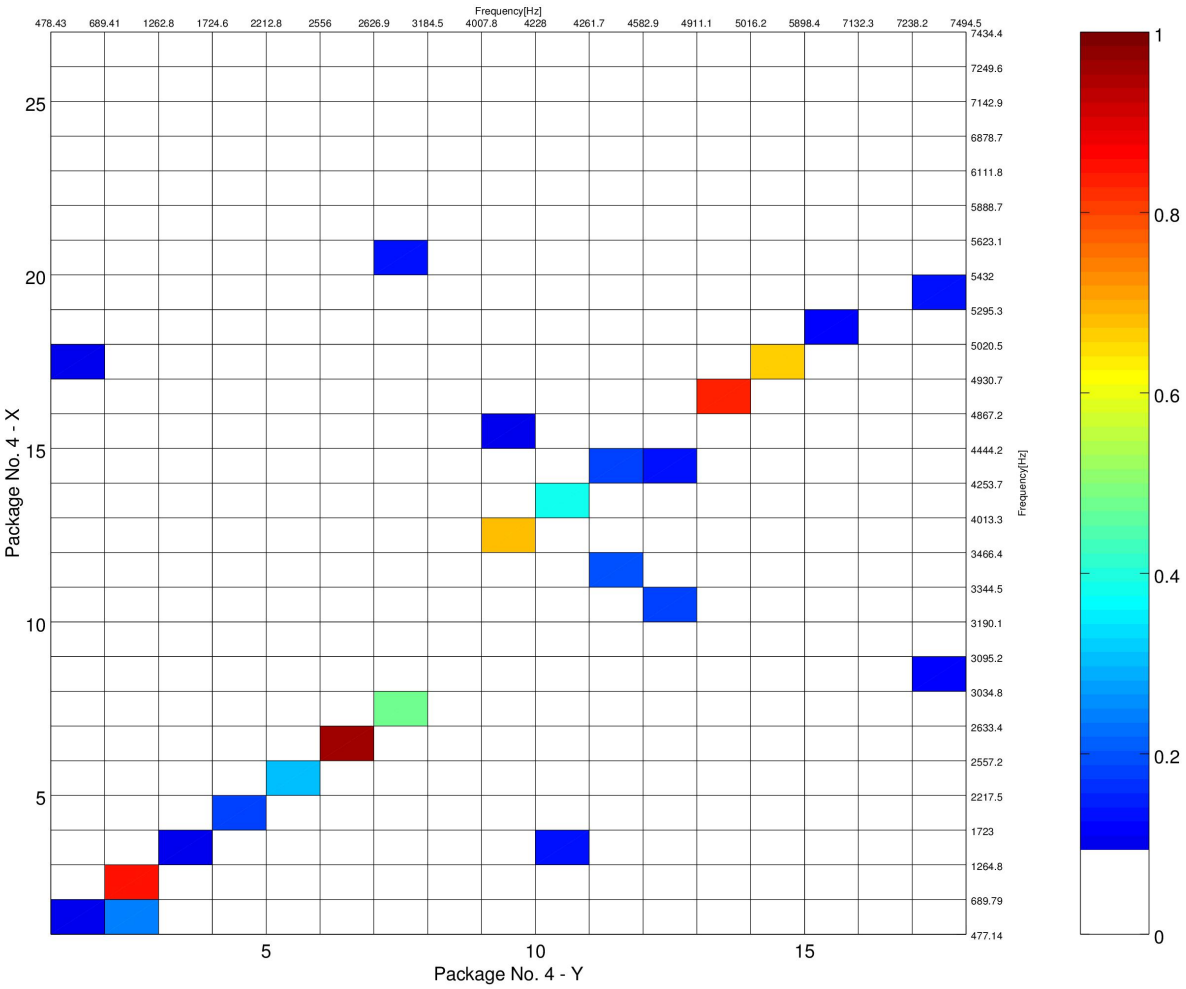

Figure 3.8 – MAC of the measurements with excitation in X and Y direction for Package No. 4

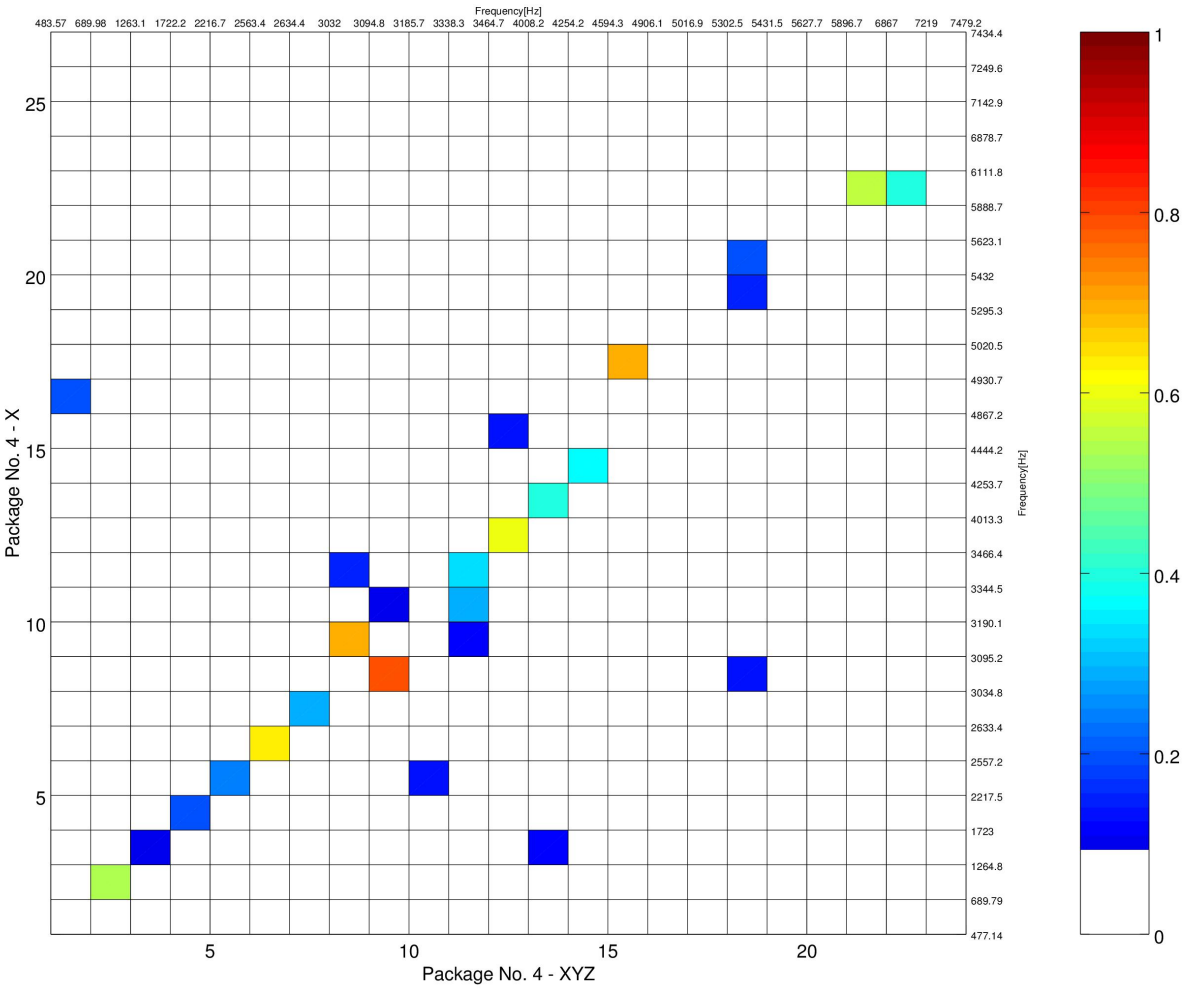

Figure 3.9 – MAC of the measurements with excitation in X and XYZ direction for Package No. 4

3.2.6 Influence of Angle and Positions of Sensors and Excitation

The positioning of sensors and the excitation of the structure is a delicate matter.
To analyze the influence of uncertainties in the mounting of the sensors regarding spacial position and angle, forced response simulations are executed.
Therefore, an instantaneous load of 1 N is applied on the FE-model of the lamination stack. The response of the structure is analyzed in one sensor position. The chosen sensor is positioned on the yoke in radial direction.
In order to examine the influence of the sensor position, a cross wire of evaluation positions around the sensor is used. In both, axial and in-plane direction, two further nodes are chosen for the assessment, each of them two FE-nodes away from the original sensor position. This corresponds to a distance of 3.45 mm for the nodes in axial direction

and a distance of 3.66 mm for the nodes in in-plane direction.
The result is displayed in figure 3.10. As the model used for this analysis is not the final model from the adaptation process executed in section 4.2.3, only a limited frequency range up to 7 kHz is shown. Yet the display allows for an analysis of positioning influences. A shift of the sensor's position leads to a change in the frequency response function. This applies to shifts in axial and in-plane direction and more so for higher frequencies. Especially the course in the valleys between the resonance peaks differs depending on the sensor position, but also the peak height shows some deviation. Depending on whether the analyzed node is closer to the respective mode's oscillation maximum or nodal point, the peak is more or less pronounced.

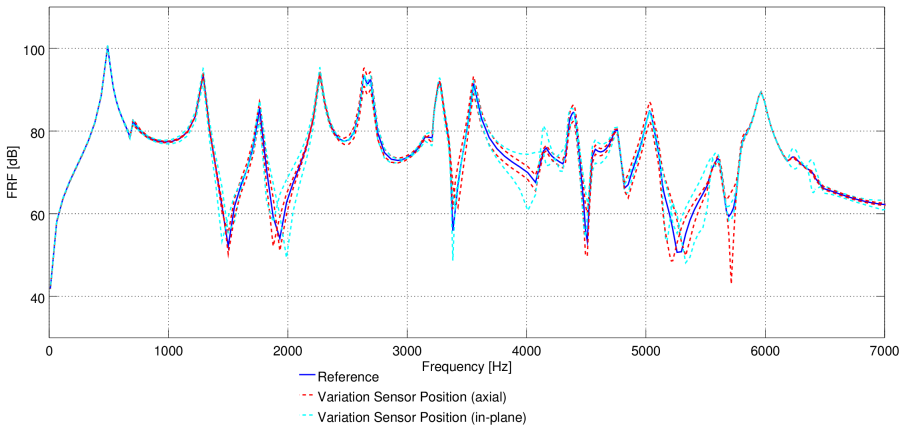

Figure 3.10 – Frequency response functions with varied sensor positions

In the next step, the influence of the sensor angle is examined. When the positioning of the sensors is not perfectly normal to the yoke surface, but aslant in some way this influences the measurement quality. To assess the impact of the sensor angle, the three dimensional simulation result is projected on different unit vectors corresponding to different sensor directions. The reference in figure 3.11 denotes the normal-to-surface direction, Angle 1 and Angle 2 are rotations of the sensor in in-plane direction by 5°, Angle 3 is a rotation by 5° in axial direction.
The sensor angle has a slight influence on the frequency response function. A rotation in axial direction leads to larger differences than a rotation in in-plane direction.

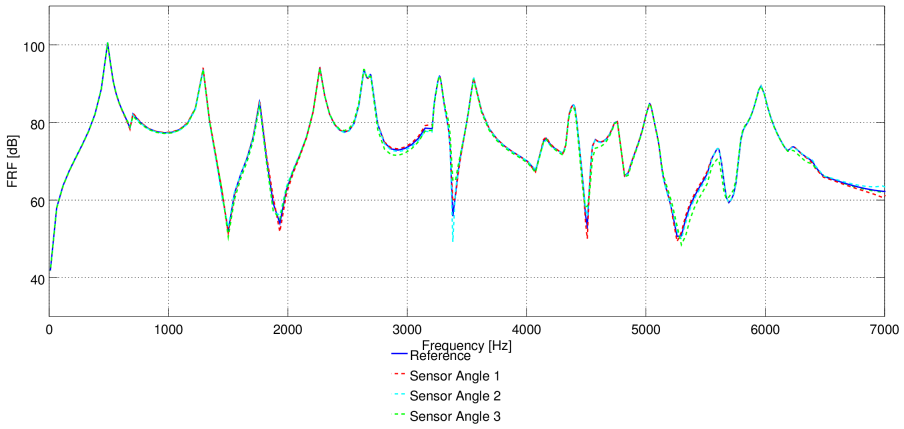

Figure 3.11 – Frequency response functions with varied sensor angles

Not only the position of the sensor, but also the position and angle of the excitation influence the structure's response. As the excitation in the measurement is performed by hand using an impulse hammer, a perfect reproduction of the excitation is impossible. Therefore, it is important to examine the influence of excitation position and angle.
In figure 3.12 a study on excitation positions is performed. Position 1 and Position 2 are shifts in opposite directions by two nodes in in-plane direction, which corresponds to a distance of 3.45 mm.
A changed excitation position influences the frequency response function as can be seen in figure 3.12. When the excitation happens close to the oscillation maximum of a mode, much energy is yielded and the respective mode is excited strongly. When the excitation happens close to a nodal point, the opposite is the case.

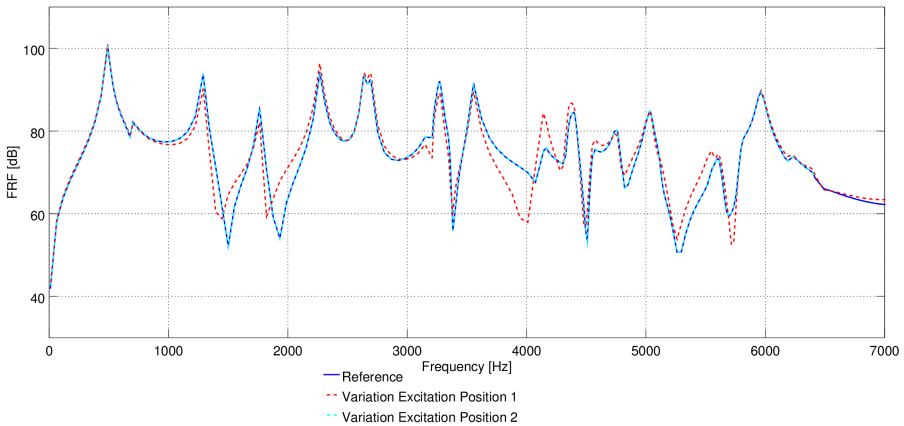

Figure 3.12 – Frequency response functions with varied excitation positions

Lastly, the influence of the excitation angle is studied, figure 3.13 shows the results. For the reference, the three directions of space are weighted equally strong. Angle 1 and

Angle 2 correspond to rotations by 5° in the in-plane components, Angle 3 is a rotation by 5° in axial direction.
A changed excitation angle does influence the frequency response function, especially in the course of the valleys between the resonance peaks.

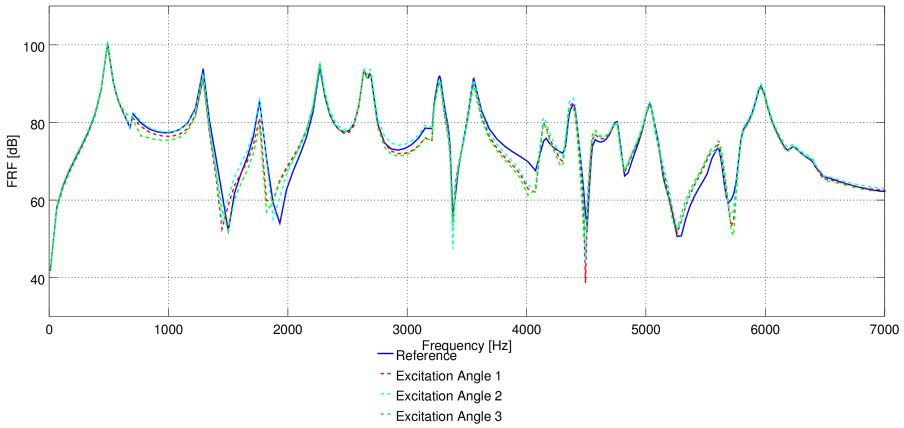

Figure 3.13 – Frequency response functions with varied excitation angles

3.2.7 Linear Behavior

Now it is of interest whether the structural dynamic behavior of the packages is linear. This means to investigate whether the behavior is dependent on the excitation magnitude or not. In order to find that out, for one of the packages the excitation was performed on three different force levels. Here it should be noted, that the range of different excitation levels is not very large. As was noted in table 3.2, the excitation force that was used in the measurements on Packages No. 1 and No. 2 was considerably higher than any of the forces in the linearity test runs. The force was reduced later on because the higher excitation force exhibited in the experiments with the packages No. 1 and 2 caused dents on the surface of the components and further destruction was to be avoided. Therefore the linearity study does not cover a large range of excitation levels.
Learning from this, a recommendation for future structural measurements is, to orient the excitation on the load in operating state. This is not an easy task, as the load in operating state is mainly applied on the teeth and consists of different force portions in radial and azimuthal direction as well as a moment. The yielded forces vary highly depending on the revolution order. Further investigations to improve the measurement set-up may be worthwhile.

MAC comparison. The degree of linearity was examined on multiple levels. The first method was to calculate the MAC between the different force levels. The figures 3.14, 3.15 and 3.16 show that the MAC is very close to the unit matrix which means the mode shapes fit very well up to 7 kHz. Only in the calculations including the lowest force level the first two modes are missing. The reason for that is that on the lowest

force level there was not enough energy in that frequency range to excite these mode shapes. The occurrence of the same mode shapes is an indicator for high linearity.

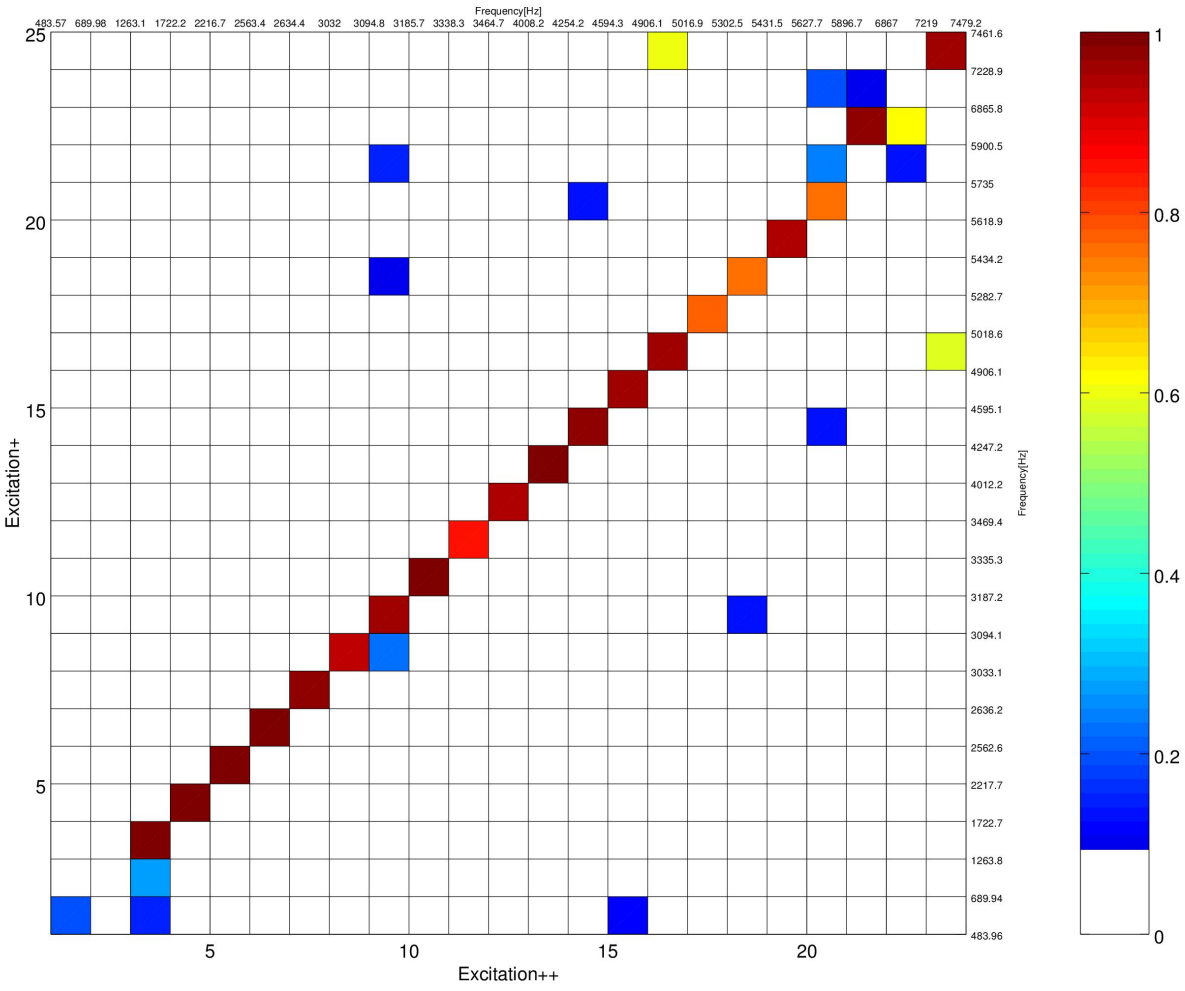

Figure 3.14 – MAC of the measurements with low (+) and medium (++) excitation force in XYZ direction for Package No. 4

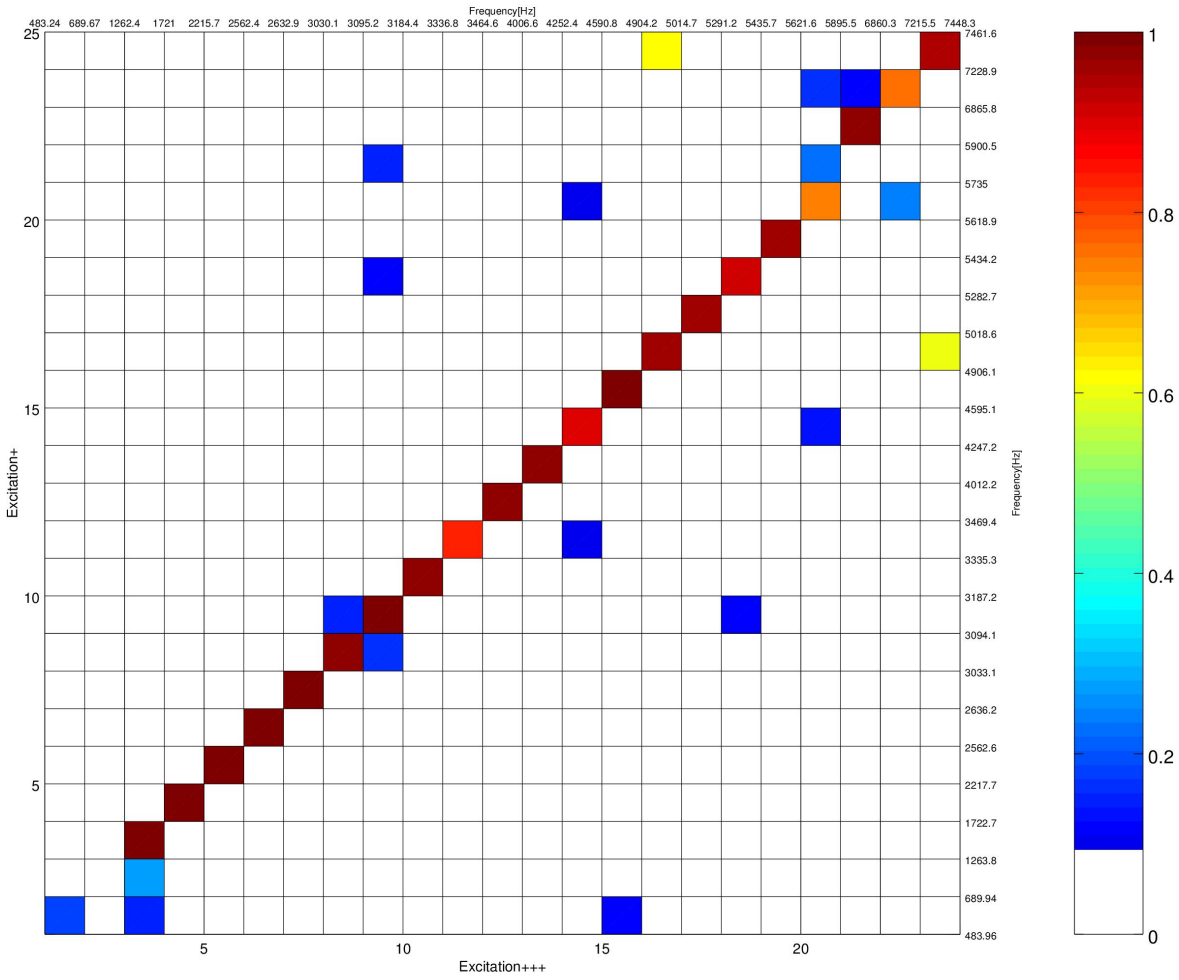

Figure 3.15 – MAC of the measurements with low (+) and high (+++) excitation force in XYZ direction for Package No. 4

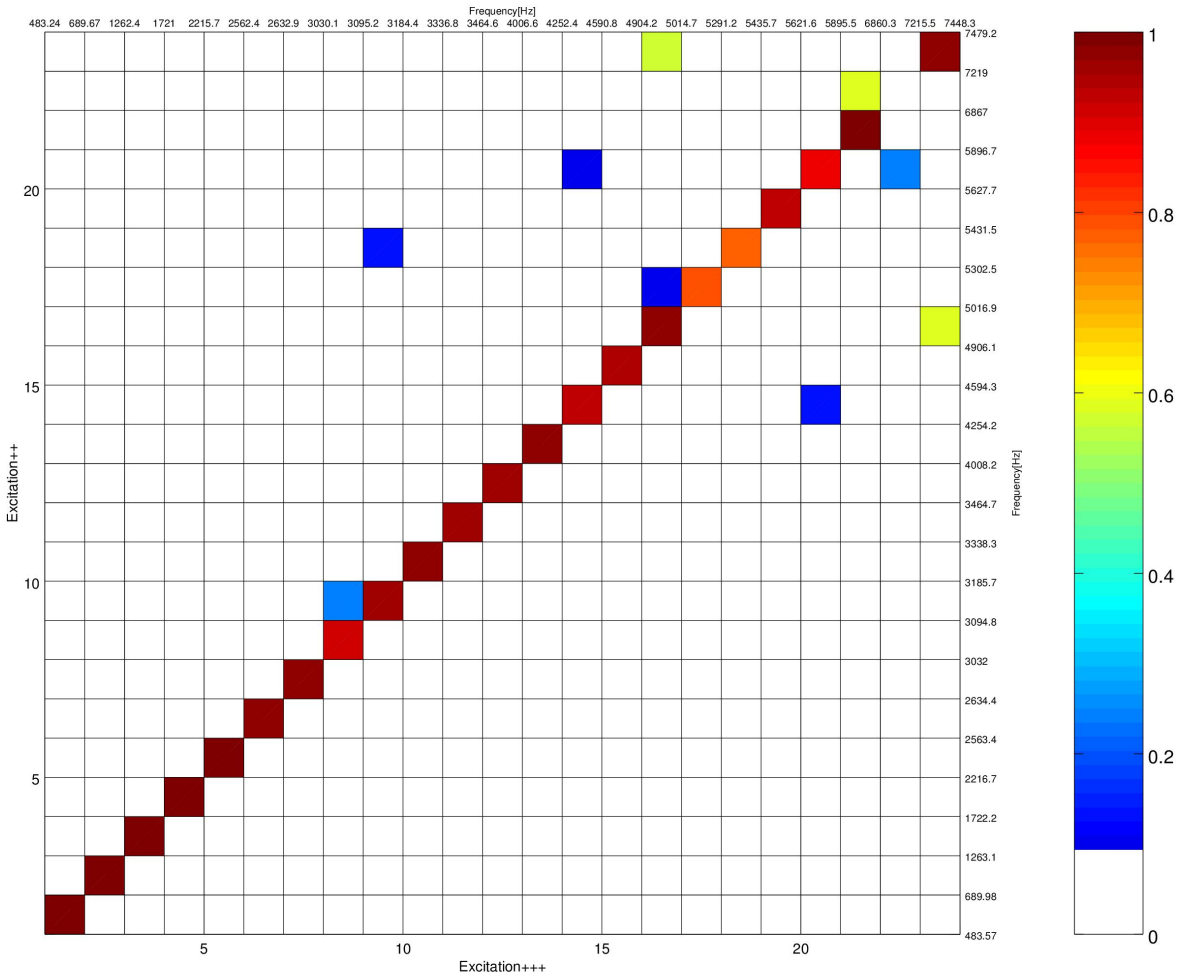

Figure 3.16 – MAC of the measurements with medium (++) and high (+++) excitation force in XYZ direction for Package No. 4

Frequency comparison. After checking whether the mode shapes fit, the next step is to evaluate whether the frequencies of the mode shapes deemed fitting by the MAC are close to each other. Therefore, the frequencies of all mode pairs that had MAC values above 0.7 are compared. These modes can be seen in the figures as blue circles. The black lines indicate modes that had no matches with MAC values above 0.7. Horizontal lines belong to mode frequencies on the ordinate - meaning that the eigenform at the marked frequency only occurs in the measurement on the respective axis. Vertical lines correspond to mode frequencies on the abscissa. It can be seen in figures 3.17, 3.18 and 3.19 that the frequencies lie very close to the diagonal which means that they are equal or nearly equal. Again, this indicates linearity.

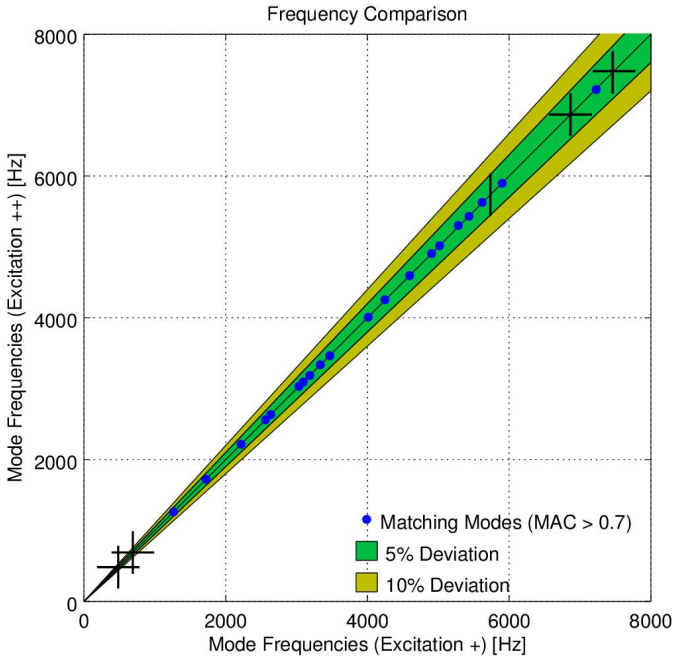

Figure 3.17 – Frequency comparison of the measurements with low (+) and medium (++) excitation force in XYZ direction for Package No. 4

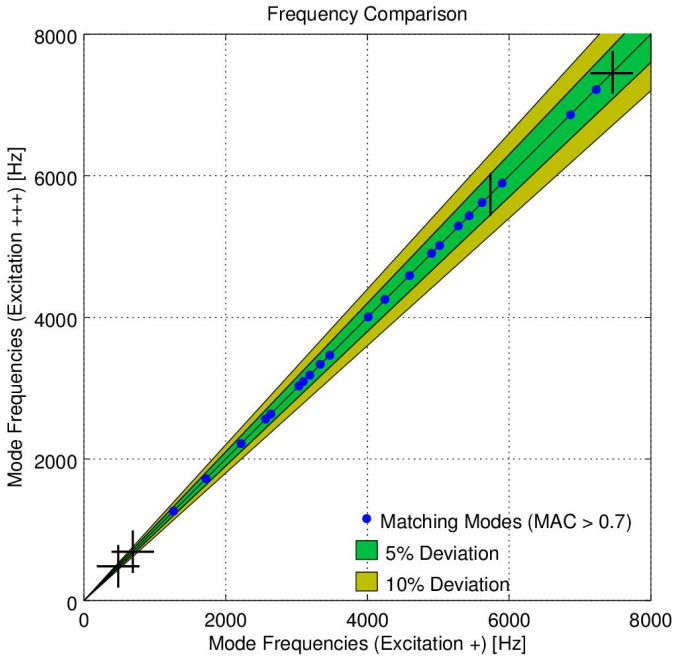

Figure 3.18 – Frequency comparison of the measurements with low (+) and high (+++) excitation force in XYZ direction for Package No. 4

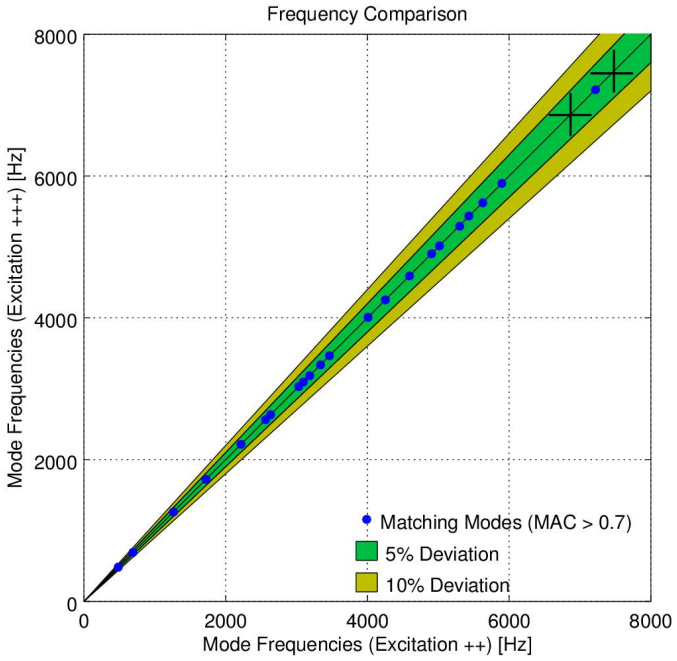

Figure 3.19 – Frequency comparison of the measurements with medium (++) and high (+++) excitation force in XYZ direction for Package No. 4

Frequency response functions. The next parameter to review the linearity with, is a comparison of frequency response functions (FRFs). The frequency response functions of three different sensors were compared for the three force levels of excitation.
The chosen sensor positions can be seen in figure 3.20.

Sensor vR2_80:
on the front side of the upper end of a tooth
Sensor vR3_120:
on the outside of the yoke
Sensor vR4_240:
on the outside of the yoke

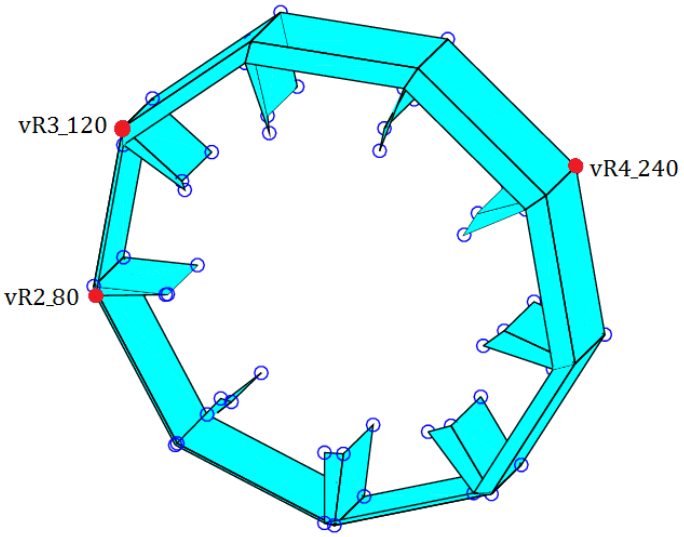

Figure 3.20 – Sensor positions used for the comparison of FRFs (Lamination stacks)

When comparing the different FRFs for the different excitation levels, it can be seen that the curves coincide quite well (figure 3.21). Especially the positions and height of the resonance peaks match very well.
The valleys in between the peaks show some deviation. A possible explanation for this is that the excitation position could not be reproduced perfectly. The level in the valleys changes depending on whether the excitation position was closer to a node or a maximum of the respective mode shape. When the excitation position is close to the maximum, the force can be yielded well into the structure at that frequency, for an excitation position close to the node the opposite is the case.
In general, the linear behavior can also be seen in the frequency response functions.

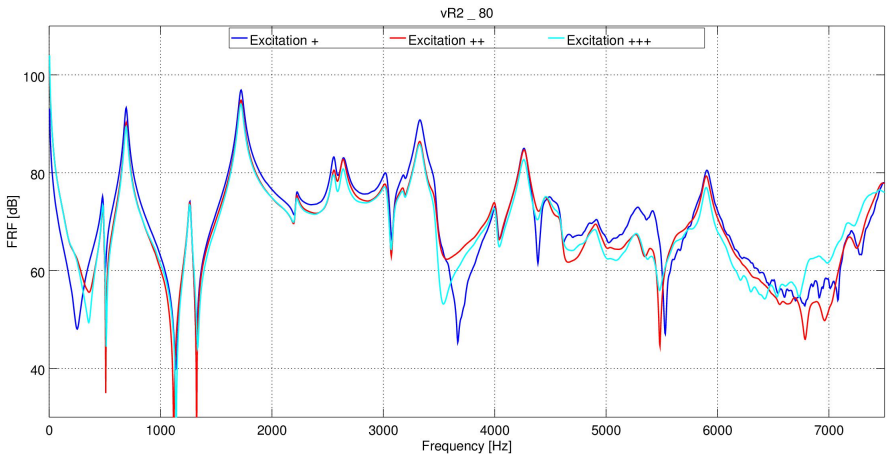

(a) FRFs at sensor vR2_80

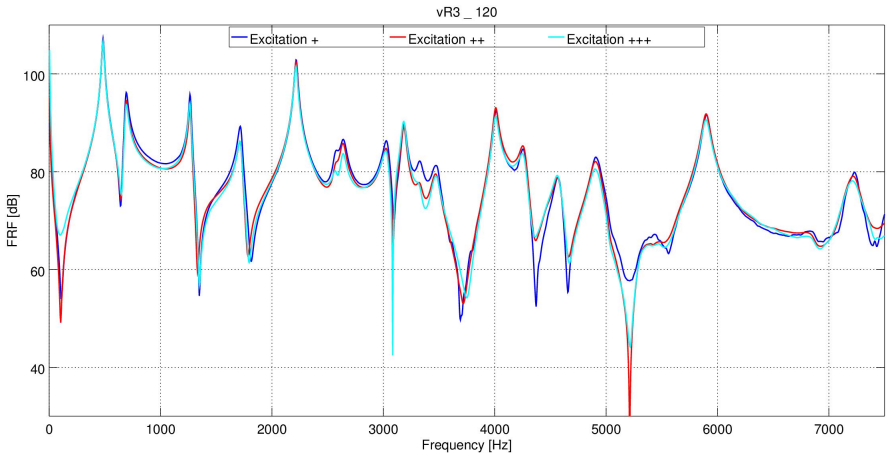

(b) FRFs at sensor vR3_120

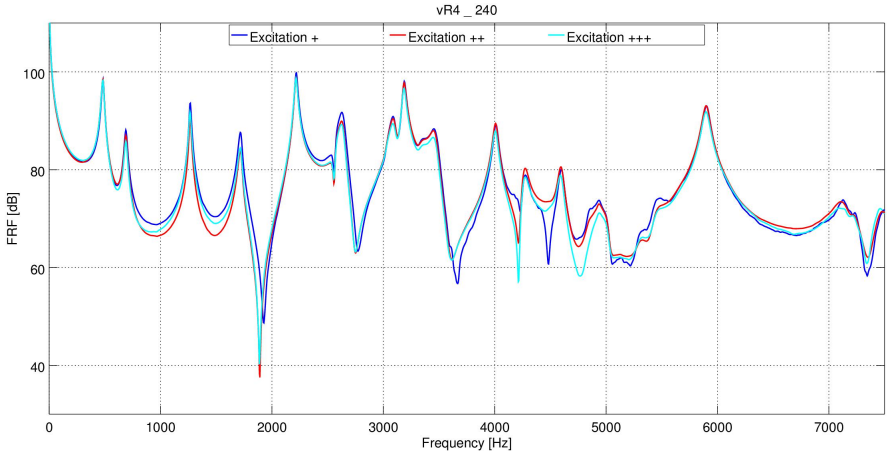

(c) FRFs at sensor vR4_240

Figure 3.21 – FRFs for three different excitation force levels at three different sensor positions

Modal damping. The last indicator that is investigated regarding the linear behavior is the modal damping.
In figure 3.22 the modal damping for each of the eigenfrequencies is scattered, as well as a curve fit to make the comparison easier. The curve fit was calculated using the MATLAB function `polyval`. Damping can be described by equation 3.1, where ζ is the damping ratio. As `polyval` only evaluates coefficients for polynomials with non-negative exponents, a multiplication by ω had to be performed in order to execute the curve fit. After the curve fit was done, the fitted curve was again divided by ω to get the correct dimension. The curve fit outputs the polynomial coefficients which can be used to calculate the factors α, β and γ. α denotes the mass proportional damping, β denotes the velocity proportional damping, and γ denotes the material damping.

$$\zeta = \frac{\alpha}{2}\frac{1}{\omega} + \frac{\beta}{2} + \frac{\gamma}{2}\omega \tag{3.1}$$

The modal damping results from the three excitations lie very close to each other, meaning the linearity is given.

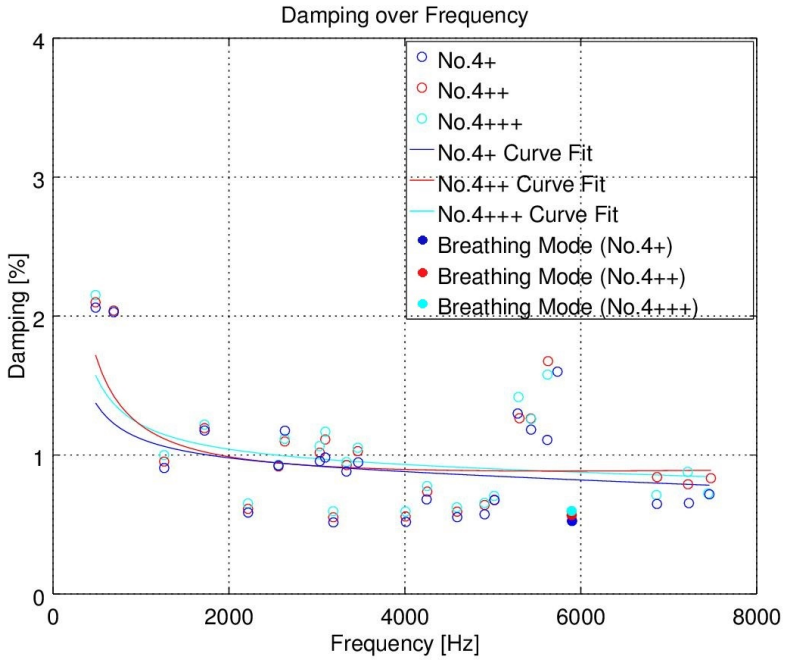

Figure 3.22 – Modal Damping for three excitation force levels and respective curve fits

In conclusion it can be said that the lamination stack exhibits linear behavior in the frequency range between 10 and 7000 Hz.

3.2.8 Production Tolerance

Fortunately, the opportunity to examine five different lamination stacks is given. This makes it possible to investigate the influence of production tolerances on the results. As table 3.1 showed, not all of the packages are identical. Two of them are thicker by 0.2 mm and also there is one sheet more. This leads to the assumption that the percentages of steel and varnish differ from package to package. These different material percentages lead to different vibration behavior. The extent of these differences is now investigated.

MAC comparison. As with the linear behavior, the first step of the investigation is to calculate the MAC to compare the mode shapes of the different lamination stacks. The comparison was performed for all possible combinations between the five packages, but for the sake of conciseness only a few representative examples are included in this work. For package No. 4 only the medium excitation force level was used for the comparison. When comparing Package No. 1 to the other four packages it is evident, that only the first five modes match acceptably. This cannot be explained by the higher excitation force level, as for Package No. 2 the excitation force was even higher, yet the MAC yields good results there. In respect to mode shapes, the force level exceeding the range of the previous linearity examination does not lead to non-linear deviations.
Above the fifth mode there is not much agreement apart from one mode at 5.9 kHz

which is the so called breathing mode. This breathing mode is of considerable relevance as this shape corresponds to an acoustic monopole source which is very efficient in noise emission. These first five modes and the breathing mode are shown in figure 3.23 along with their classification explained in the following.
The modes are classified by a specific scheme inspired by [36, p. 33]. The first number tells how many maxima there are around the perimeter normal to the axial direction. The second number indicates whether there is ($\rightarrow 1$) or is not ($\rightarrow 0$) a deformation along the axial direction. This classification is illustrated in figure 3.23.

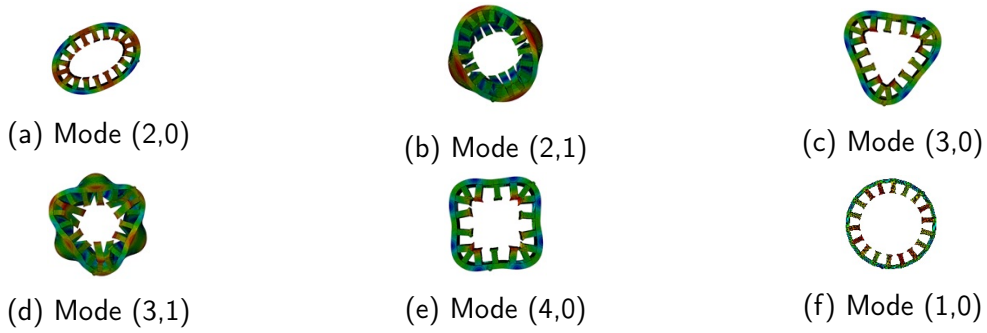

(a) Mode (2,0) (b) Mode (2,1) (c) Mode (3,0)

(d) Mode (3,1) (e) Mode (4,0) (f) Mode (1,0)

Figure 3.23 – First five mode shapes (a-e) and breathing mode (f)

When comparing the other packages apart from No.1, there is considerably more agreement between the mode shapes. There are higher MAC values also for higher frequencies, especially in the comparison between the packages No.2, No.4 and No.5. Package No.3 shows a little bit more deviation which might be caused by the fact that the coherence in this measurement was a bit lower than for the other runs.
Nonetheless, the production variation is quite noticeable. The differences here are a lot larger than for the comparison of different force levels.
The fact that for package No. 1 the deviation is noticeably higher above the fifth mode leads to the assumption that this measurement run was not executed in the same way as the others. Therefore, the measurement data from this measurement run cannot be deemed trustworthy above the fifth mode.

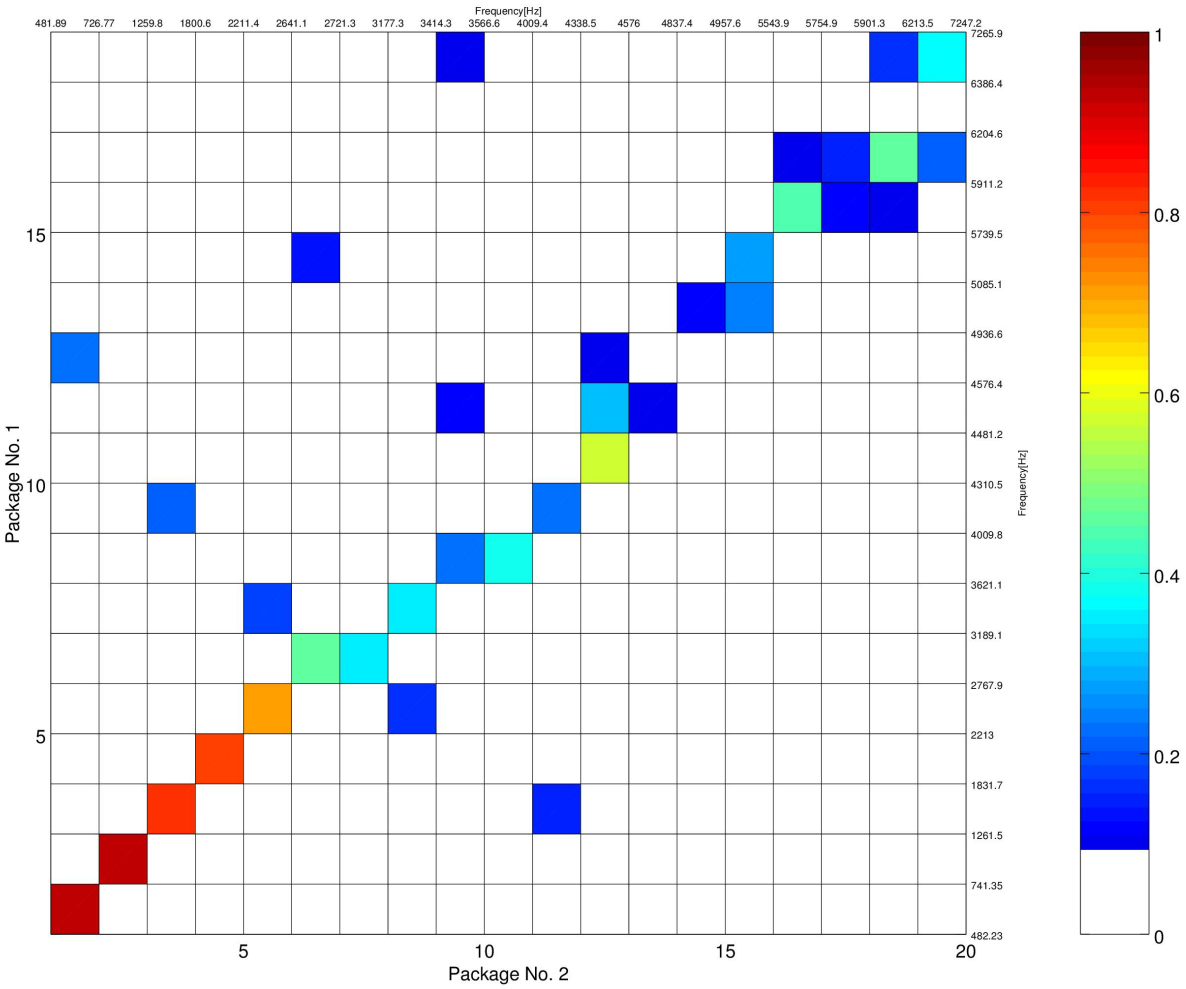

Figure 3.24 – MAC of the measurements of Package No.1 and No.2 with excitation in XYZ direction

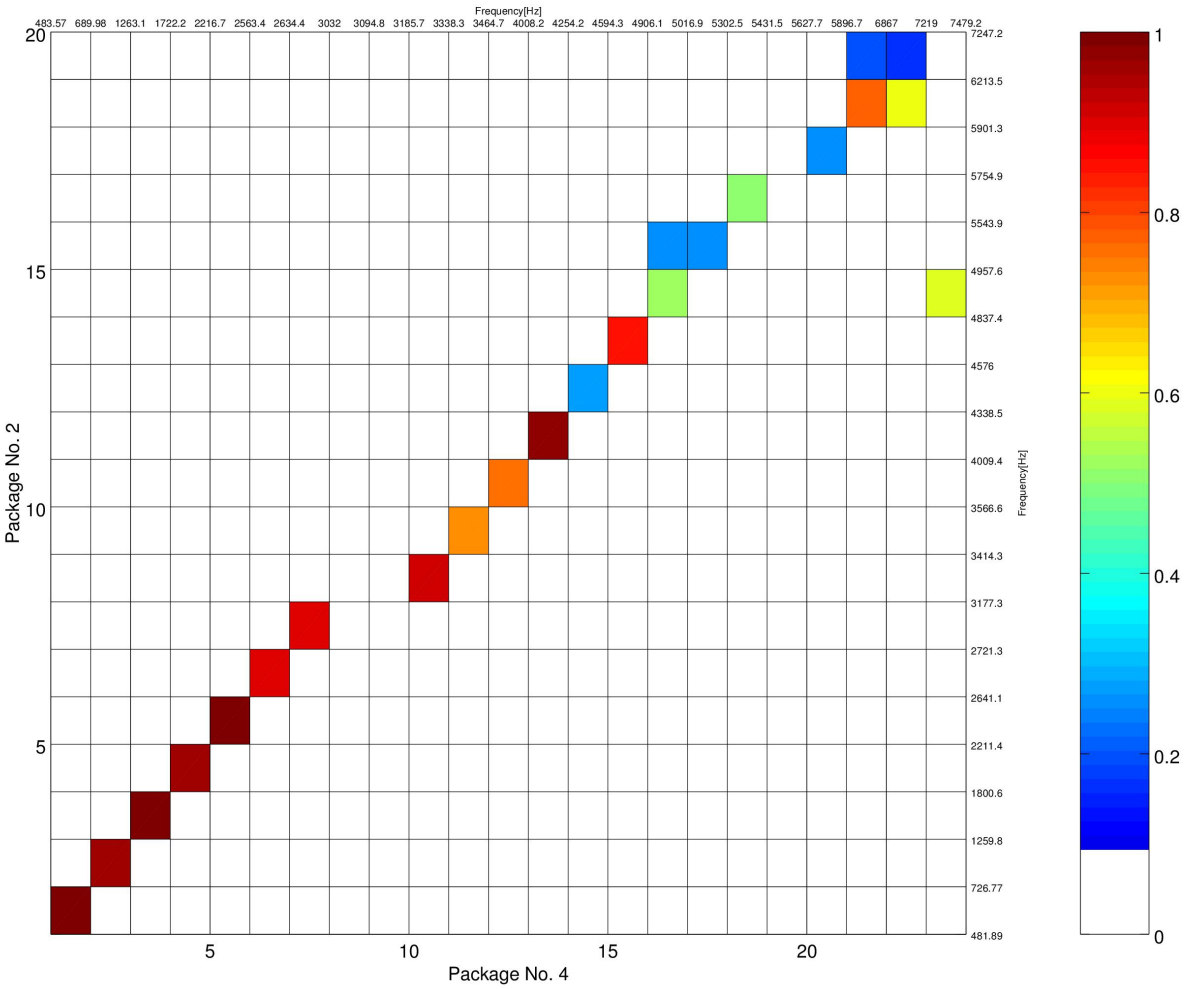

Figure 3.25 – MAC of the measurements of Package No.2 and No.4 with excitation in XYZ direction

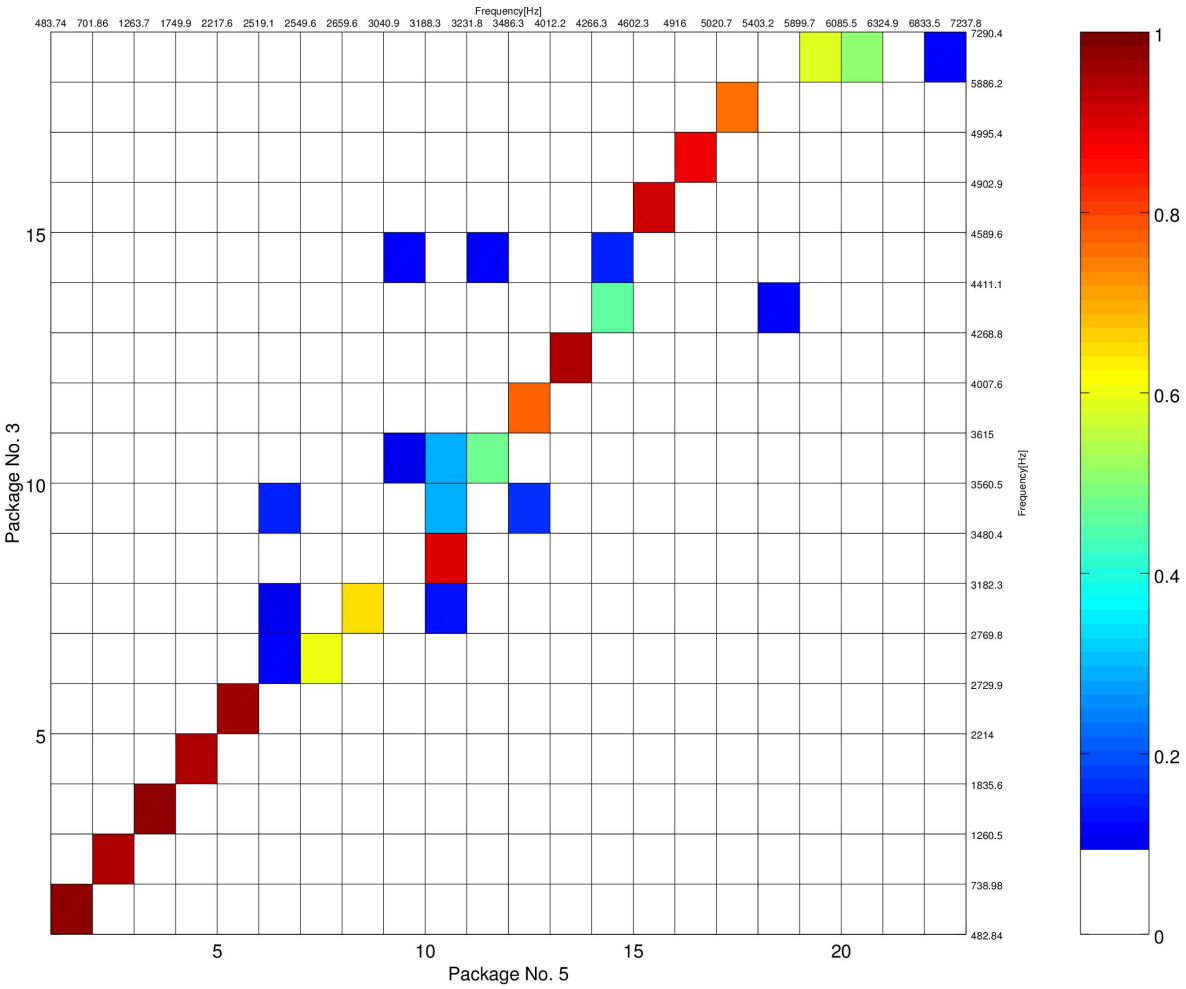

Figure 3.26 – MAC of the measurements of Package No.3 and No.5 with excitation in XYZ direction

Frequency comparison After comparing the mode shapes, the eigenfrequencies of matching mode shapes are looked at.
The frequencies do not lie perfectly on the diagonal, but they are still close to it, they are all within the band of $\pm 5\,\%$ deviation. This tells that in the case that the mode shapes match, the frequencies match as well, but also here the production variation is visible.
An influence of the varying excitation force levels is not evident regarding the eigenfrequencies.

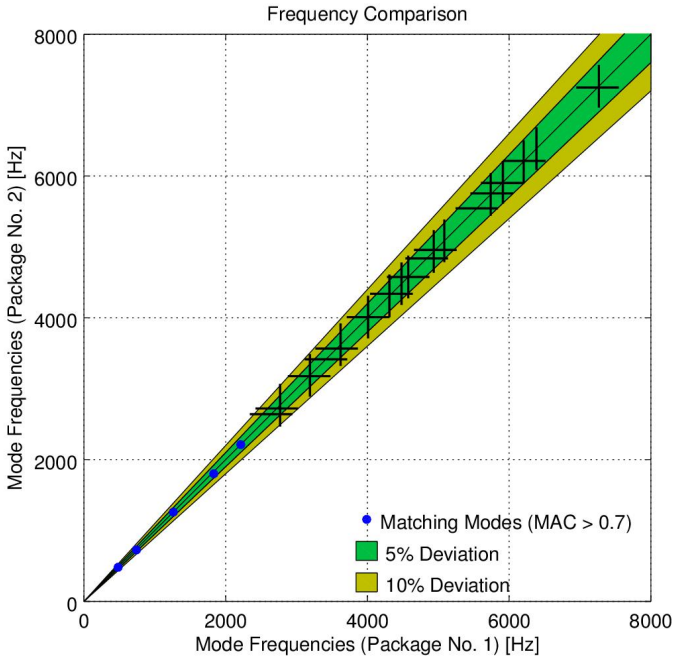

Figure 3.27 – Frequency comparison of the measurements of Package No.1 and No.2 with excitation in XYZ direction

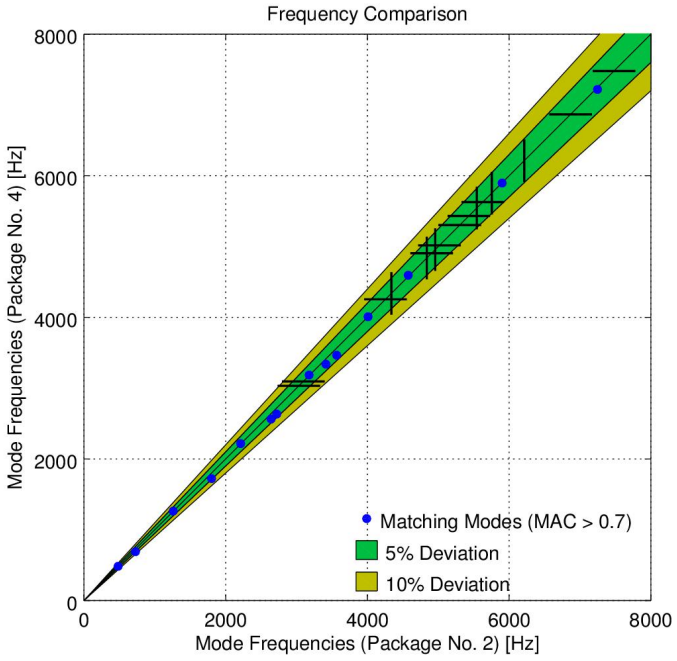

Figure 3.28 – Frequency comparison of the measurements of Package No.2 and No.4 with excitation in XYZ direction

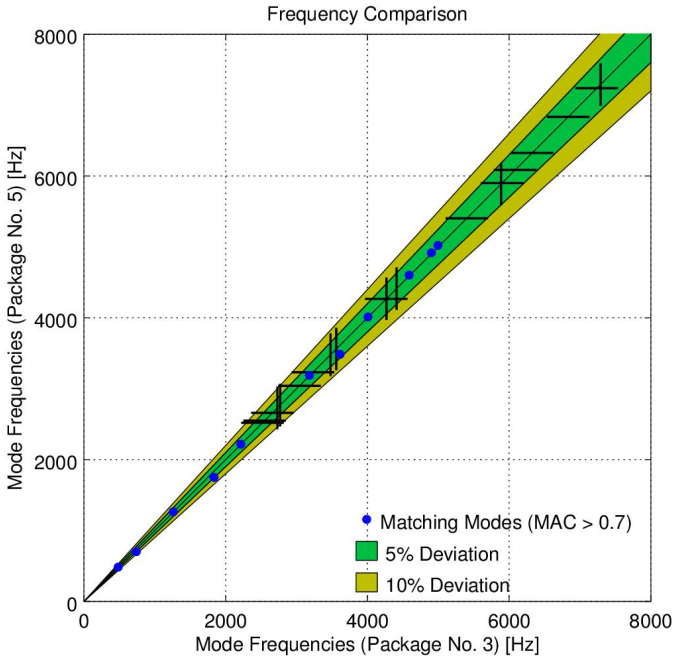

Figure 3.29 – Frequency comparison of the measurements of Package No.3 and No.5 with excitation in XYZ direction

As the deviations of the frequencies are noticeable, a closer look is taken on them. Therefore, in table 3.4 all the matching modes for all of the packages along with their frequency [2] and their shape classification are listed. For every mode the maximal deviation using equation 3.2 is calculated [3].

$$\text{Deviation} = \frac{f_{max} - f_{min}}{f_{max} + f_{min}} \cdot 100\,\% \tag{3.2}$$

The results from this calculation could be divided into two groups. One group with deviation above 1 % (red) and one group with deviation below 1 % (blue). This coincides very well with the mode shape types. Modes of type 0 (blue) without deformation along the axial direction show considerably less deviation than modes of type 1 (red). The modes of type 0 are mainly determined by the material properties of steel. A little change in steel percentage does not have much influence on the overall E_p (equation 2.20). Therefore, these modes are less sensitive to the production variance. The modes of type 1 on the other hand are mainly determined by the varnish. A variation in the percentage of the varnish has a noticeable influence on E_z (equation 2.19). Therefore, the production tolerances are more visible for this type of modes.

2. Mode frequencies are rounded to an accuracy of 1 Hz
3. Deviations in percent are rounded to an accuracy of 0.01%

No. 1 [Hz]	No. 2 [Hz]	No. 3 [Hz]	No. 4 [Hz]	No. 5 [Hz]	Deviation [%]	Shape (-,-)
482	482	483	484	484	0.19	(2,0)
741	727	739	690	702	3.59	(2,1)
1262	1260	1261	1263	1264	0.15	(3,0)
1832	1800	1836	1722	1750	3.19	(3,1)
2213	2211	2214	2217	2218	0.14	(4,0)
	2641	2730	2563	2550	3.42	(2,1)
	2721		2634	2660	1.62	(4,1)
			3095	3041	0.88	(1,1)
	3177	3182	3186	3188	0.17	(5,0)
	3414		3338		1.13	(1,1)
	3567	3615	3465	3486	2.12	(5,1)
	4009	4008	4008	4012	0.06	(6,0)
	4576	4590	4594	4602	0.29	(7,0)
	4837	4903	4906	4916	0.81	(8,0)
		4995	5017	5021	0.25	(9,0)
	5901		5897	5900	0.04	(0,0)
	7247	7294	7219		0.49	(1,0)

Table 3.4 – Mode frequencies of matching mode shapes - systematic difference in deviation of frequencies between 0-type modes (blue) and 1-type modes (red)

Frequency response functions. The comparison of frequency response functions is performed for the same sensor positions as for the investigation of linearity (figure 3.30).
Here a considerable deviation can be seen. The positions of the resonance peaks fit relatively well, although for the point on the tooth (vR2_80) there is a larger deviation. As this sensor pointed in axial direction, the same explanation as for the higher deviation of the frequencies for type-1 mode shapes can be given. The movement in this sensor is more determined by the varnish and therefore the production variance gets more obvious at this point.
Still, the points on the outside of the packages do not have well fitting FRFs either. Neither the height of the peaks nor the course of the valleys match. These differences can partly be explained by differences in the damping caused by varying varnish percentages. Also there might be an influence of imperfect reproduction of the excitation position as could already be seen at the linearity assessment. The curves for the five packages create quite a wide band of possible results.

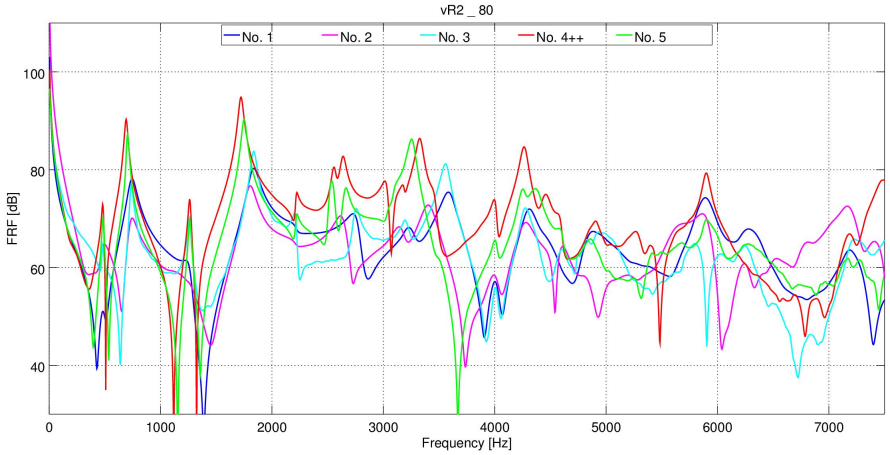

(a) FRFs at sensor vR2_80

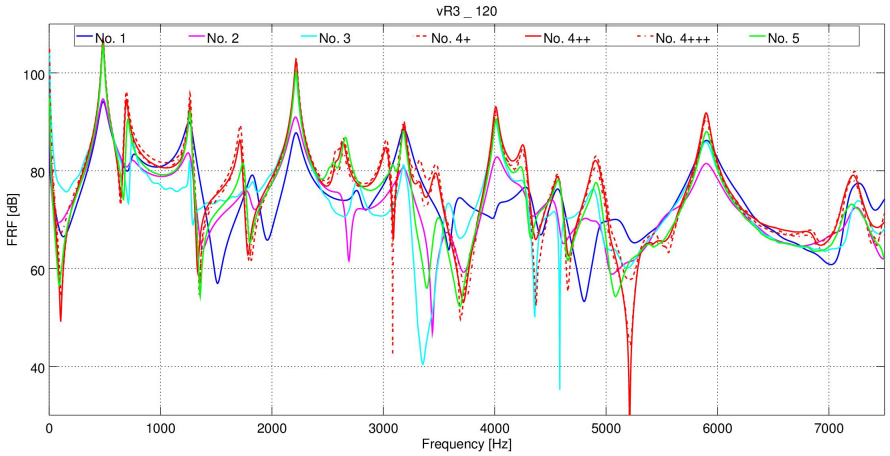

(b) FRFs at sensor vR3_120

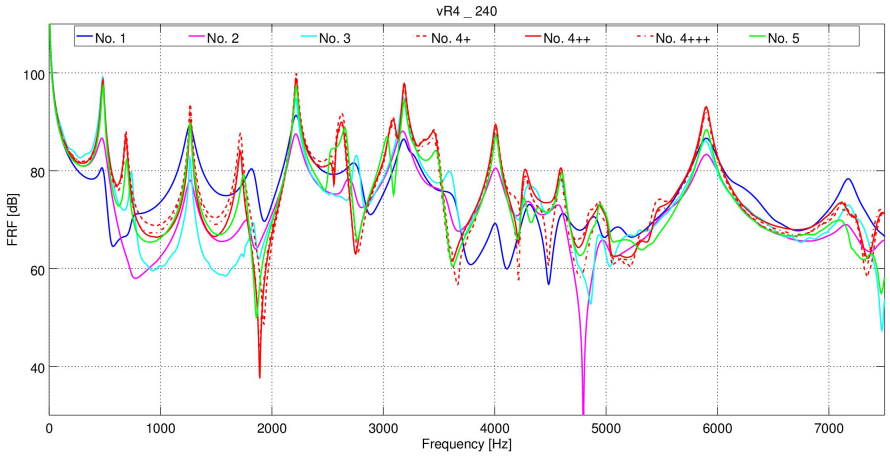

(c) FRFs at sensor vR4_240

Figure 3.30 – FRFs for the five different packages in three different sensor positions and with different excitation forces

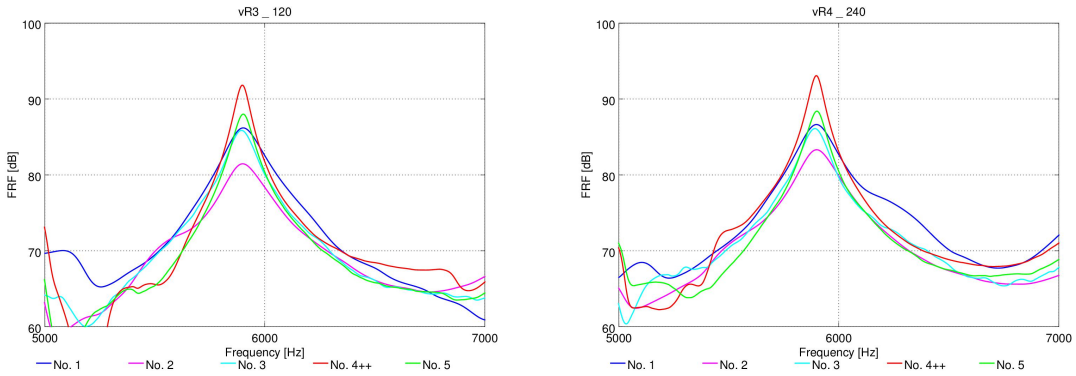

(a) FRFs at sensor vR3_120 (b) FRFs at sensor vR4_240

Figure 3.31 – FRFs for the five different packages at two different sensor positions - zoomed on the frequency range around the breathing mode

The difference in peak height is illustrated in detail in figure 3.31. Here the resonance peak of the breathing mode is shown at two of the sensor positions. The sensor $vR2\_80$ is left out in this display because the breathing mode is not well pronounced in its FRF. This can be again explained by the 1D-sensor's positioning in axial direction.
In the height of the peaks there is a deviation of 10dB. This will make comparison with the simulation more difficult, as there cannot be something like the perfect fit.

Modal Damping. The last step is to compare the modal damping of the five packages.

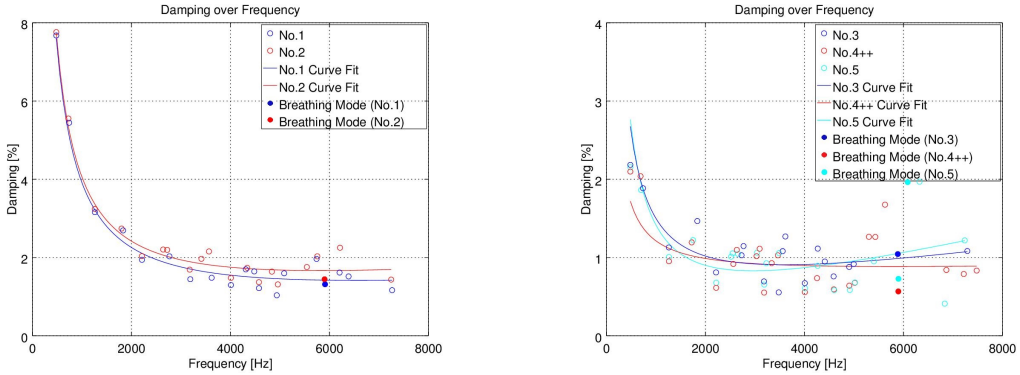

(a) Modal damping of packages No.1 and No.2 (b) Modal damping of packages No.3, No.4 and No.5

Figure 3.32 – Modal damping for the five different packages

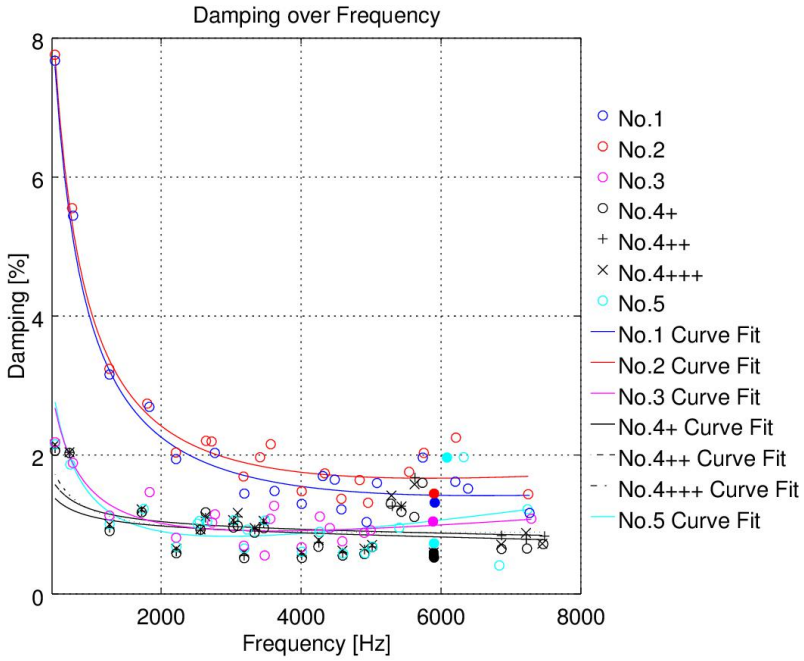

Figure 3.33 – Modal damping for the five different packages

It can be clearly seen in figure 3.33 that the damping for the packages No.1 and No.2 is considerably higher than for the other three packages. This cannot be explained solely by the production variation. For packages No.1 and No.2 the percentage of varnish should be lower, meaning that there should be less damping.
The difference might also be explained by the fact that the excitation force was higher for the first two packages. Because of the higher force there were dents in the surface of the packages. This deformation could have absorbed some energy of the excitation which leads to seemingly higher damping.
In figures 3.32 and 3.33 the breathing mode is denoted by filled markers. There is a wide variation of the damping for this one mode. This explains why the peak height in the FRFs (figure 3.31) is several dB apart.

For all of the packages, the damping of the breathing mode lies beneath the respective curve fit. This suggests a connection between mode type and damping value. In order to investigate whether this is the case, the damping for the packages No.3, No.4 (++), and No.5 is examined in detail. Figure 3.34 shows the individual damping values for the three chosen packages. The color of the markers denotes the mode types - blue for 0-type modes, red for 1-type modes. The curve fit is built from the mean of the three curve fits from the single packages, which have already been close together.
In the majority of cases the damping of 0-type modes lies beneath the curve fit, for 1-type modes the opposite is the case. This behavior is present up to 5.5 kHz.

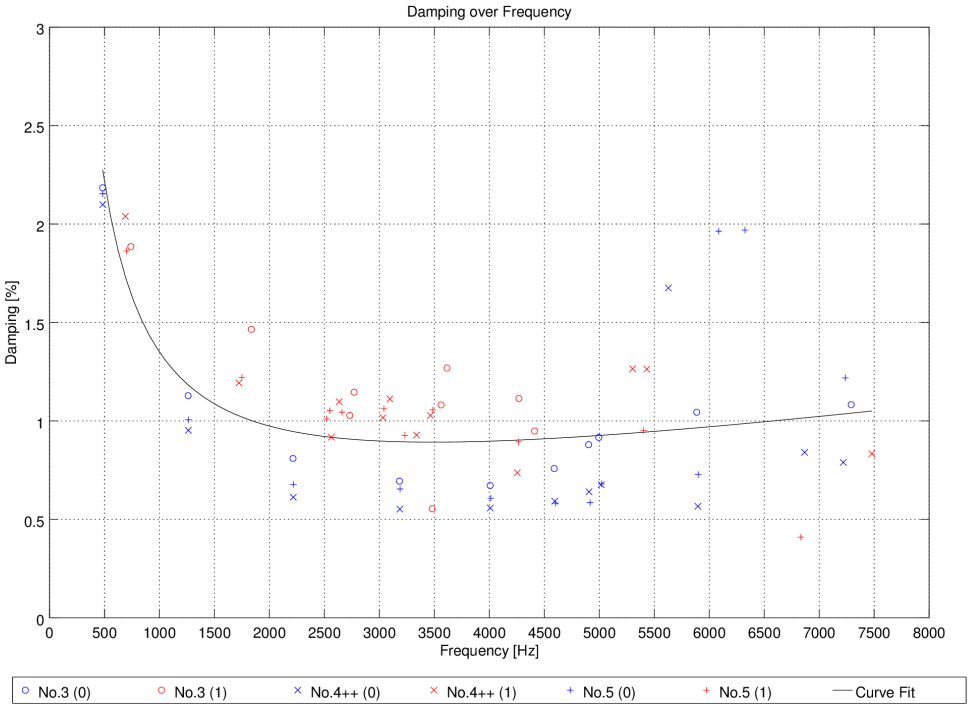

Figure 3.34 – Systematic deviation in damping for different mode types

The deviation of the damping from the curve fit for the different mode types is analyzed using a box plot (figure 3.35).
The median (horizontal red line) of the 0-type modes at -20.88% ($N_0 = 34$) is significantly lower than the median of the 1-type modes at 14.66% ($N_1 = 32$). The overall median of the deviation lies at -0.47% ($N_a = 66$).
For the 0-type modes there are more extreme outliers (outside 3 times the interquartile range) and a larger interquartile range than for the 1-type modes.

The 0-type modes are determined mostly by the vibration behavior of the steel sheets, whereas for the 1-type modes the behavior of the resin has more influence. The resin has a higher material damping than the steel sheets, therefore the respective modes exhibit an increased modal damping.

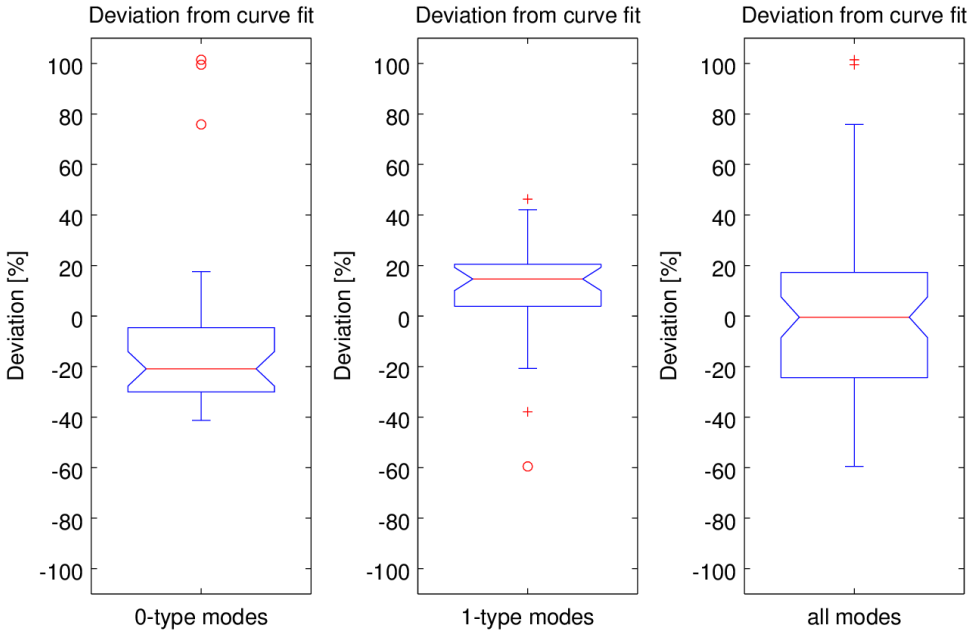

Figure 3.35 – Deviation in damping from curve fit for different mode types

3.2.9 Summary of the Results

As the analysis of the coherence showed, the measurements are trustworthy up to 7500 Hz. Therefore, the validation of the simulation can only be performed up to this frequency.
The components exhibit linear behavior which makes linear modeling possible. Forces exceeding the range examined in respect to linearity, still lead to reliable results regarding mode shapes and eigenfrequencies. An improvement in measurement set-up regarding the excitation method may yield further results and is to be investigated.
There is a considerable production tolerance that should be kept in mind. When the simulation matches one of the packages it does not necessarily fit with the other packages.
Parameter studies in the following simulations confirm that a small variation in steel percentage leads to considerable changes in mode frequencies depending on their classification type.
A systematic difference in damping could be observed between the modes of different classification types.

3.3 Stator (Range Extender)

3.3.1 Measurement Object

The stator of the range extender is built from one package of laminated sheets. A sketch of the stator can be seen in figure 3.36.

The teeth of the package (light grey) are wrapped with insulated copper windings (orange) that are separated from the core with an insulating paper (green). The windings are fully coated using synthetic resin (anthracite).

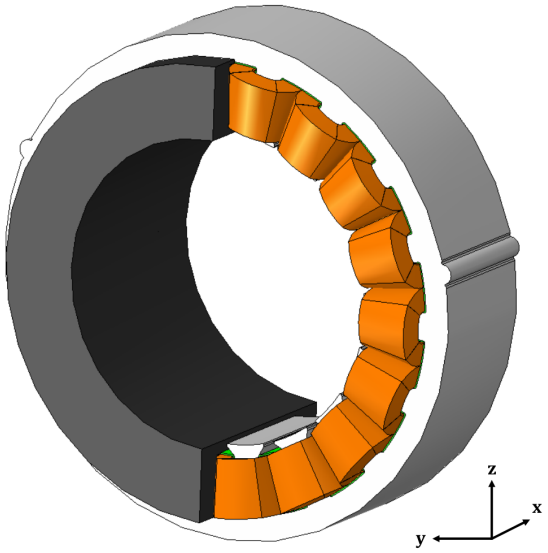

Figure 3.36 – Geometry of the stator

3.3.2 Measurement Set-up

As with the other measurement objects, the stator is hung on elastic ropes for a free oscillation.
The excitation was performed using an impulse hammer on different force levels. The measurement was also performed in different directions of space but due to lack of time only the XYZ excitation could be analyzed.
The measurement was conducted using 51 1-D acceleration sensors.

3.3.3 Coherence

The coherence data are the coherences of every single of the 51 measurement points for one measurement run. To simplify the analysis, the mean over all these measurement points is calculated and plotted for each run.
In the frequency range where the coherence lies above the value of 0.9 (marked by the horizontal red line in the figure), the measurement data is deemed reliable. For the display the whole measurement frequency range from 0 Hz to 12.8 kHz is chosen.

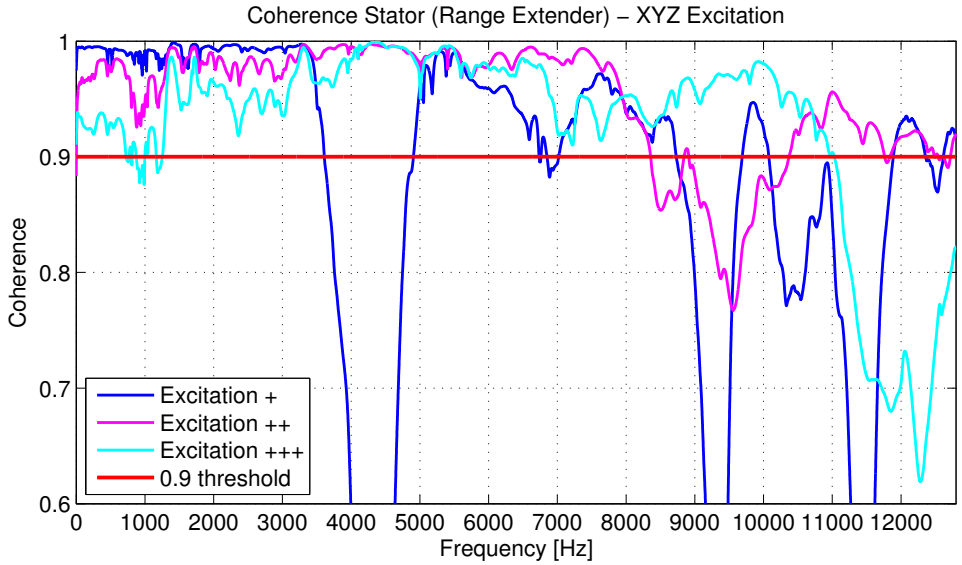

Figure 3.37 – Coherence stator - excitation XYZ with three different levels of excitation force

For the measurement runs with medium and high excitation force in XYZ direction the coherence is above 0.9 up to 8.5 kHz as can be seen in figure 3.37. The measurement run with low excitation force shows a severe drop in the coherence at about 4.3 kHz. The results of this measurement runs have to be regarded with caution.
The following analyses are limited to the frequency range from 1000 Hz to 8500 Hz. The lower limit of 1000 Hz is chosen because below that frequencies no modes apart from rigid body modes appear.

3.3.4 Quality of Sensor Positioning

The quality of the sensor positions is assessed as before. Figure 3.38 shows the AutoMAC of the stator simulation. The MAC resembles the unit matrix very well, the mode shapes in the desired frequency range can be resolved well.

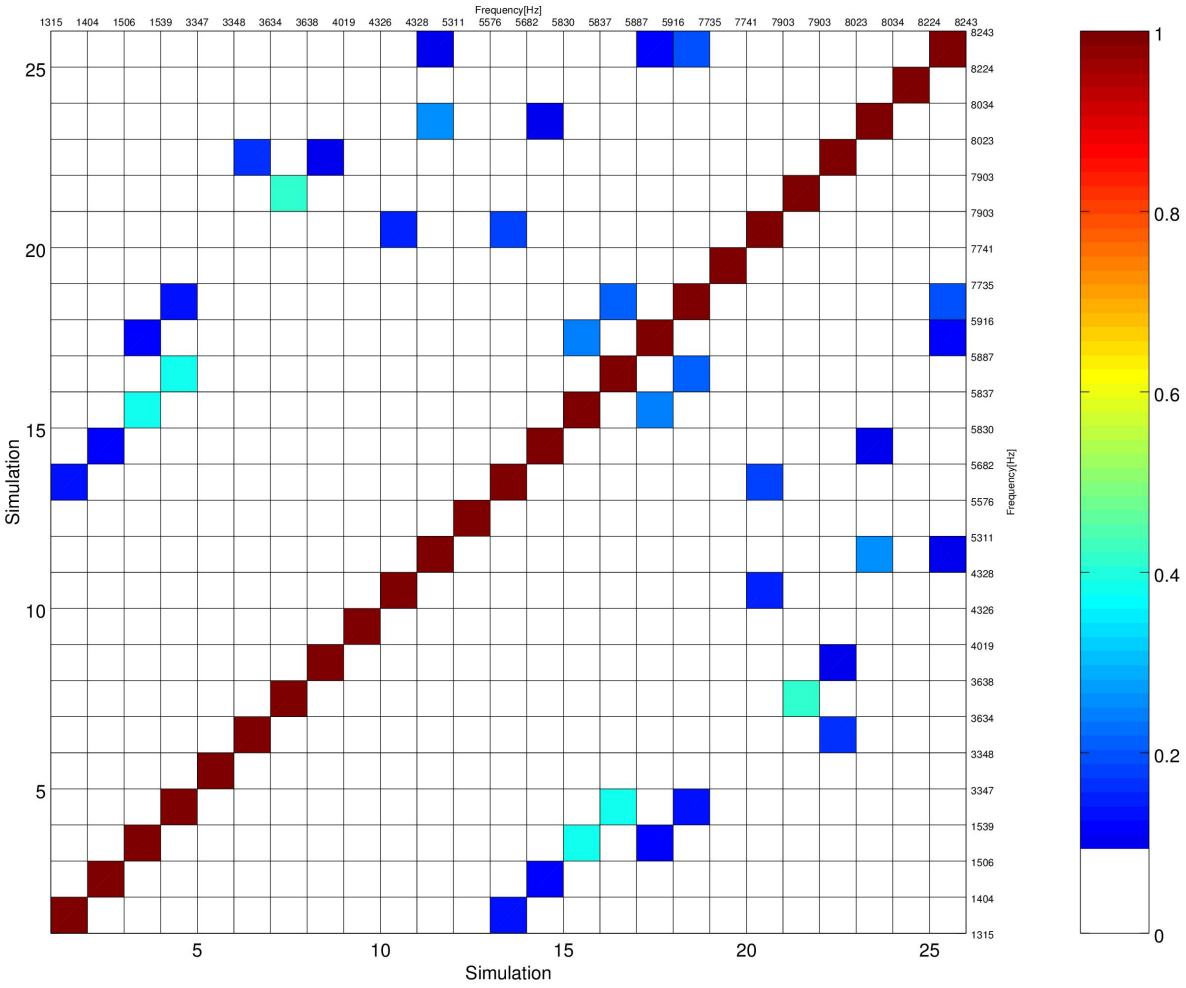

Figure 3.38 – AutoMAC of the simulation of the stator using nominal parameters

3.3.5 Linear Behavior

MAC comparison. As with the lamination stacks, the linearity of the oscillation behavior is examined using different measures. Initially the mode shapes of the measurement runs are compared using the MAC. The figures 3.39, 3.40 and 3.41 show this comparison. There can be seen that most of the mode shapes in the desired frequency range match well. But for the comparisons including the lowest excitation force, the

concordance is lower than for the comparison between medium and high force. This may be explained by the lower coherence in the low excitation measurement run.

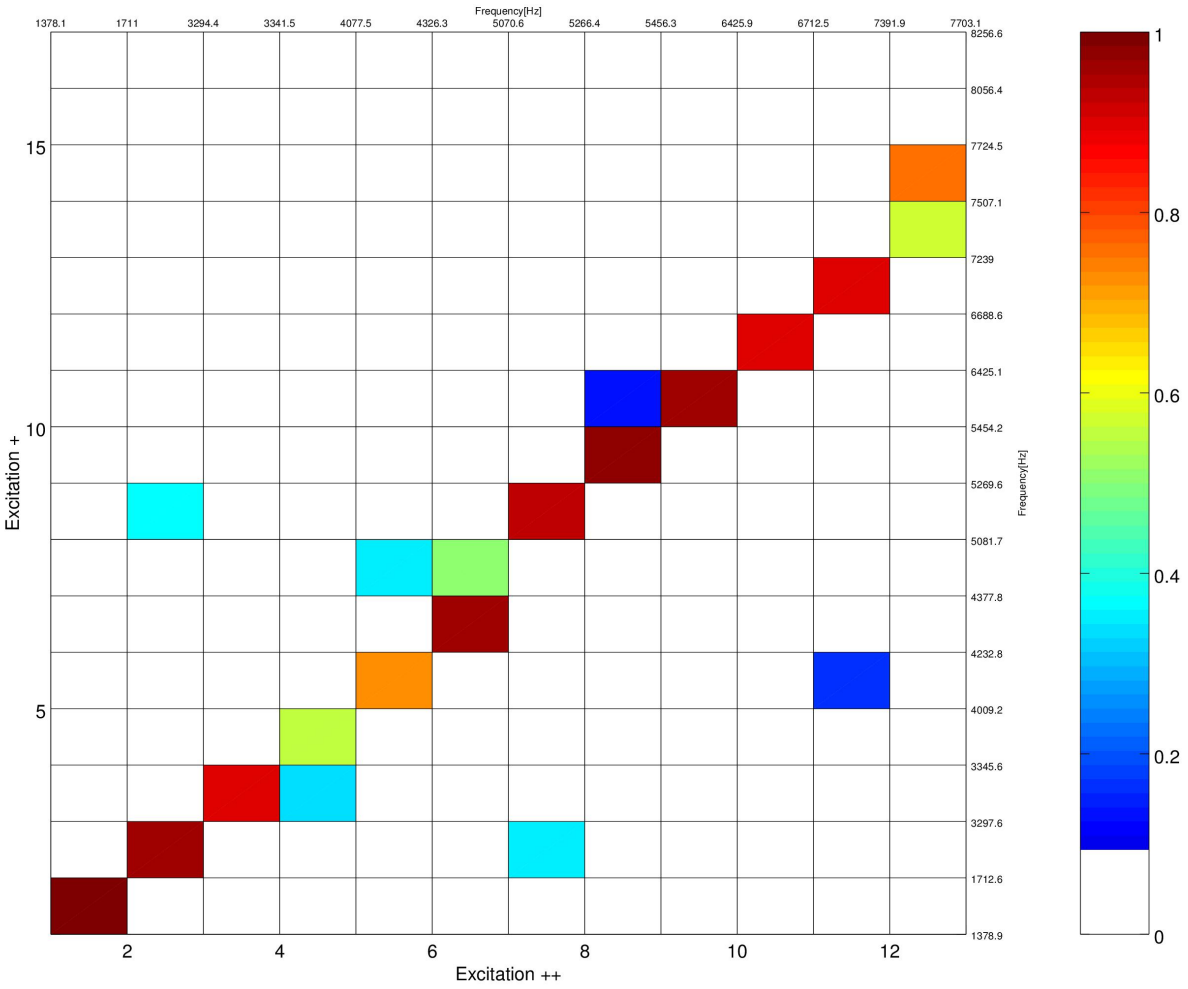

Figure 3.39 – MAC of the measurements with low (+) and medium (++) excitation force in XYZ direction for the stator

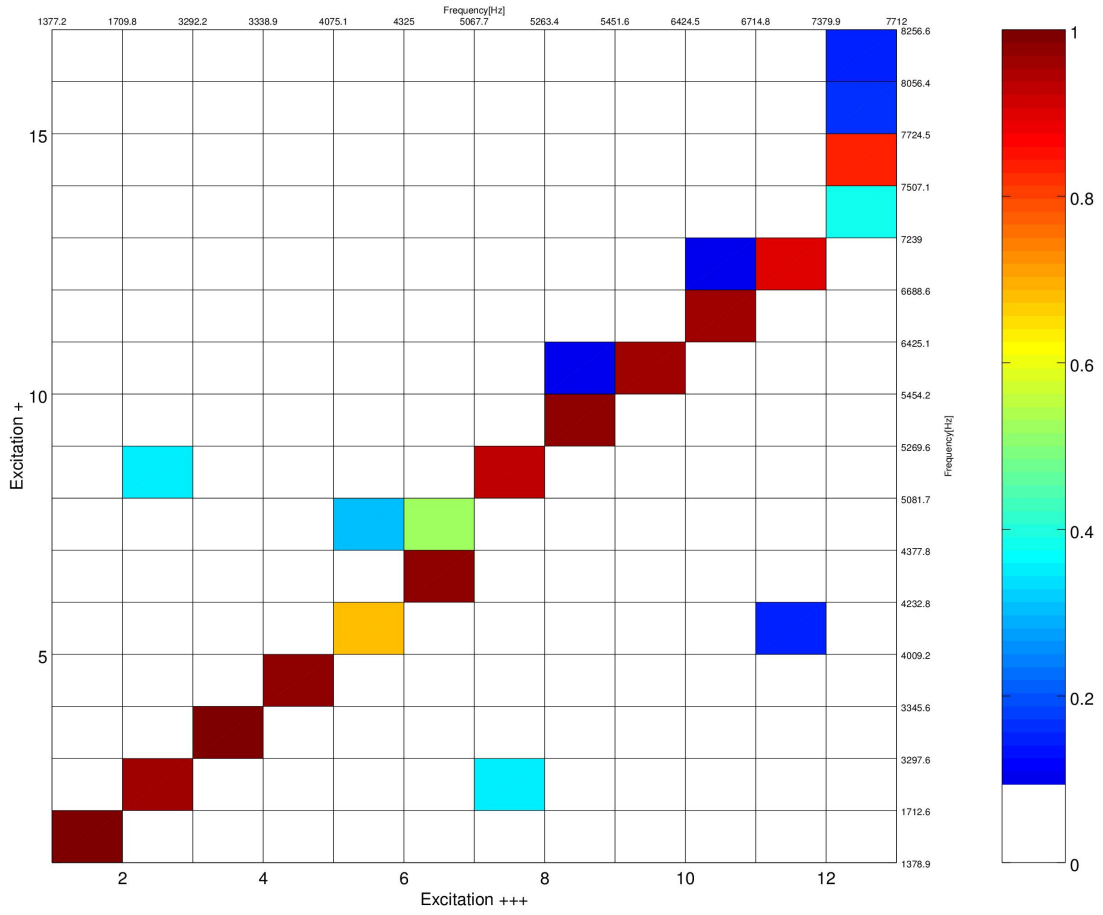

Figure 3.40 – MAC of the measurements with low (+) and high (+++) excitation force in XYZ direction for the stator

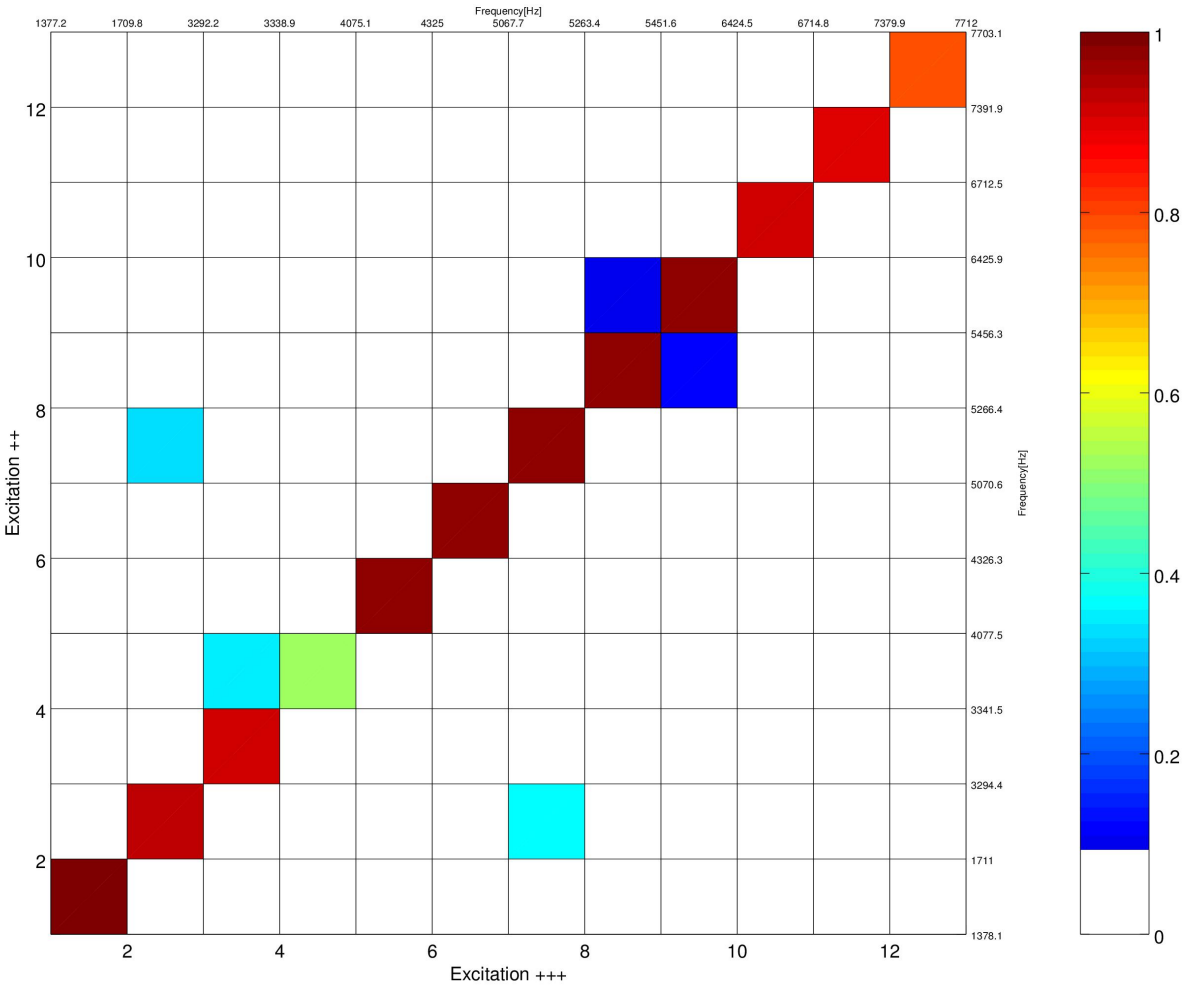

Figure 3.41 – MAC of the measurements with medium (++) and high (+++) excitation force in XYZ direction for the stator

Frequency comparison. After comparing the mode shapes, the corresponding mode frequencies are compared. As can be seen in figures 3.42, 3.43 and 3.44 all the matching modes can be found very close to the diagonal which means the mode frequencies of matching shapes are close to each other. This argues for linearity.

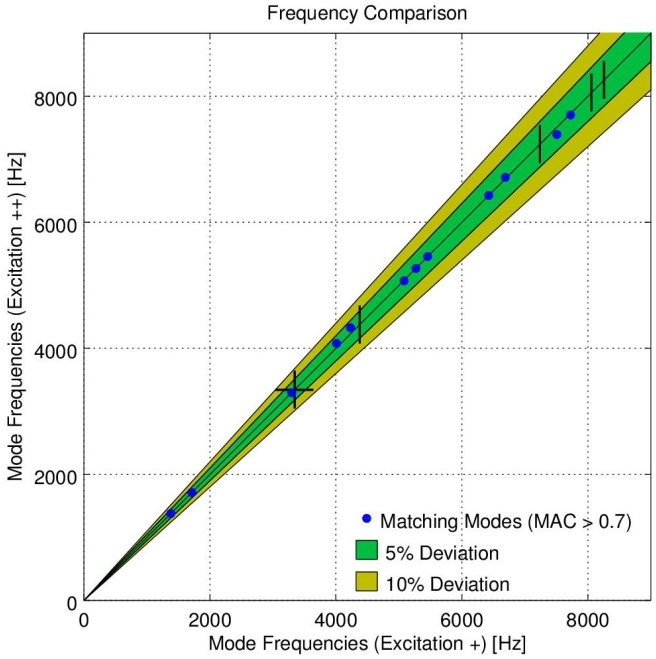

Figure 3.42 – Frequency comparison of the measurements with low (+) and medium (++) excitation force in XYZ direction for the stator

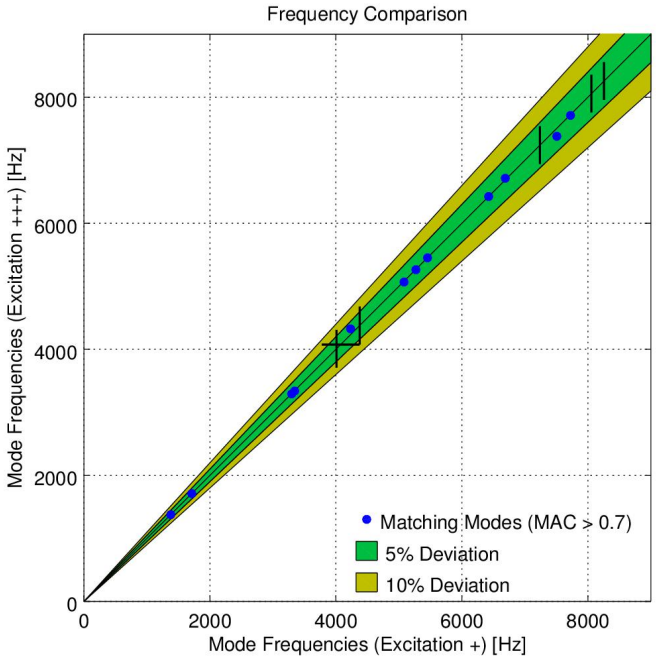

Figure 3.43 – Frequency comparison of the measurements with low (+) and high (+++) excitation force in XYZ direction for the stator

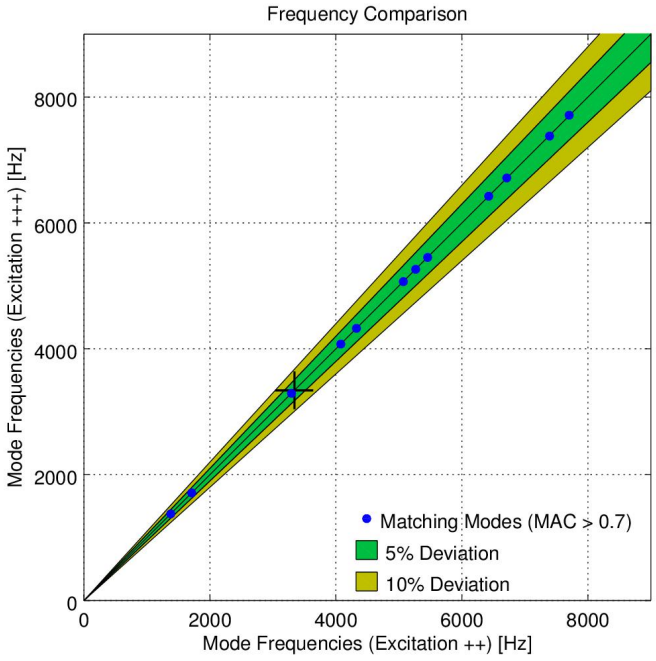

Figure 3.44 – Frequency comparison of the measurements with medium (++) and high (+++) excitation force in XYZ direction for the stator

Frequency response functions. A comparison of frequency response functions is performed in four different sensor positions that can be seen in figure 3.45.

Sensor vR2_180:
on the coating in radial direction

Sensor vR3_80:
on the yoke in axial direction

Sensor vR5_120:
on the yoke in radial direction

Sensor vR7_240:
on the inside of the stator in radial direction

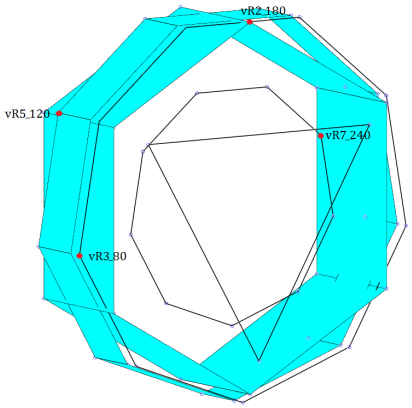

Figure 3.45 – Sensor positions used for the comparison of FRFs

When analyzing figure 3.46 it can be seen that the positions and the height of the resonance peaks match quite well although the low excitation differs from the other two measurement runs. Especially around 4.5 kHz, where the coherence of the low excitation had a drop, the deviation is eye-catching. This applies to all four chosen sensor positions. The course of the valleys differs for the three excitations which may again be explained by imprecisions in the reproduction of the excitation positions.

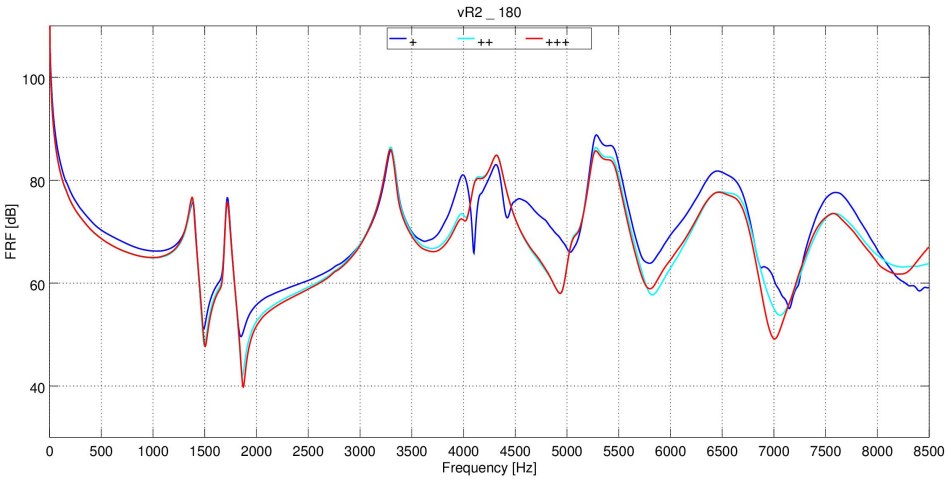

(a) FRFs at sensor vR2_180

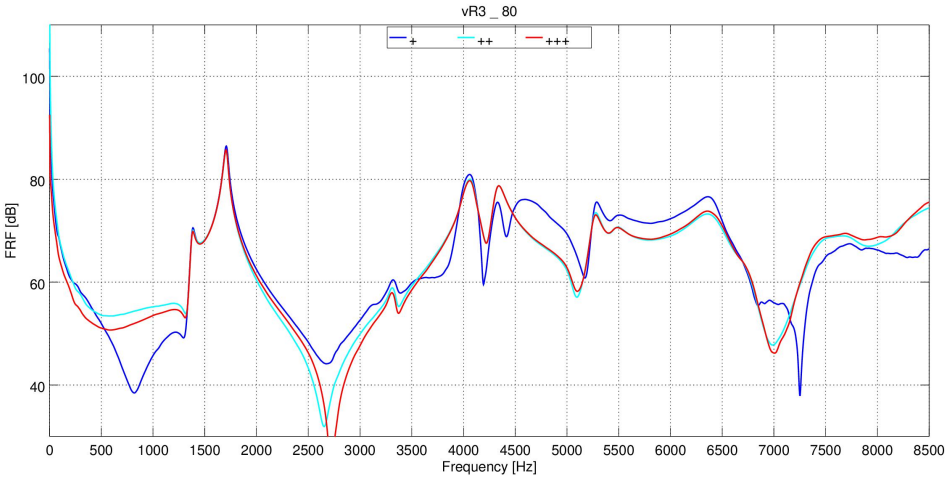

(b) FRFs at sensor vR3_80

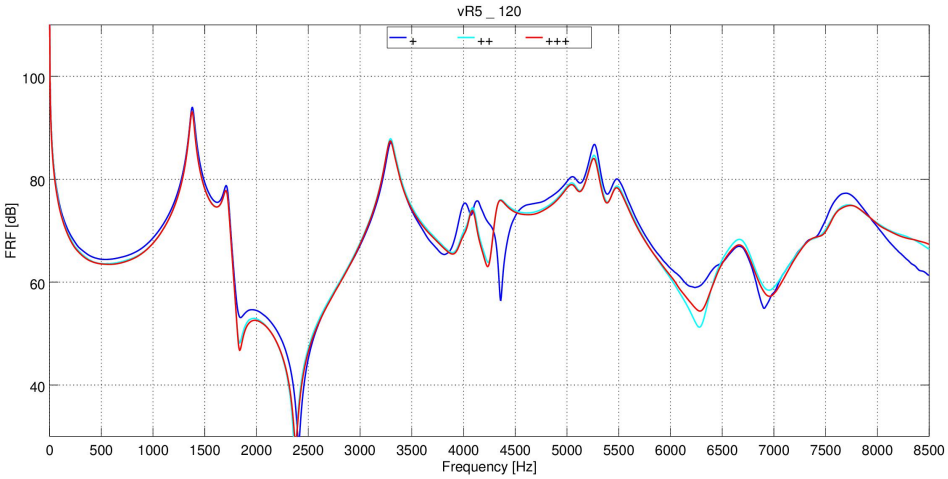

(c) FRFs at sensor vR5_120

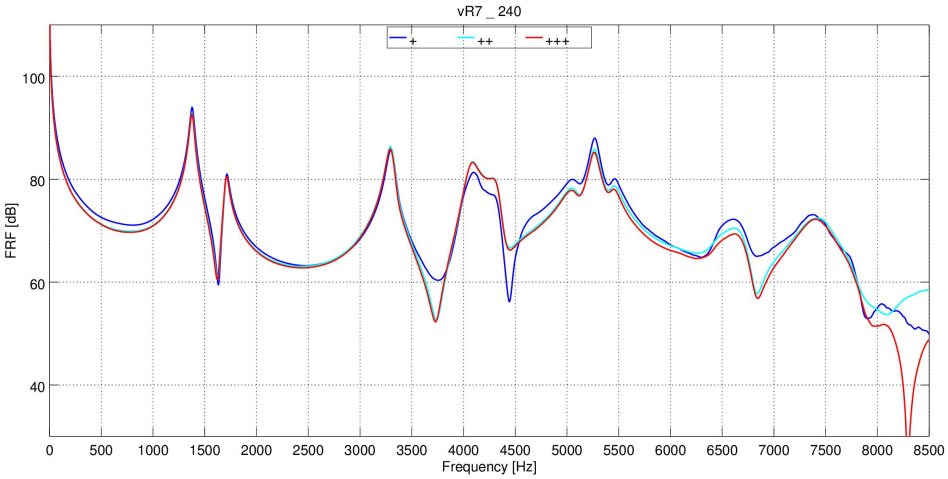

(d) FRFs at sensor vR7_240

Figure 3.46 – FRFs for three different excitation force levels in four different sensor positions

Modal Damping. Also the modal damping can be analyzed. As before, the curve fit is performed using the procedure described in 3.2.7. It is palpable that the curve fit for the lowest excitation has a completely different course than the other two curve fits which indicates that the measurement data are not trustworthy.
The curve fits for the medium and the high excitation force are very similar, this confirms the linearity of the oscillation behavior.

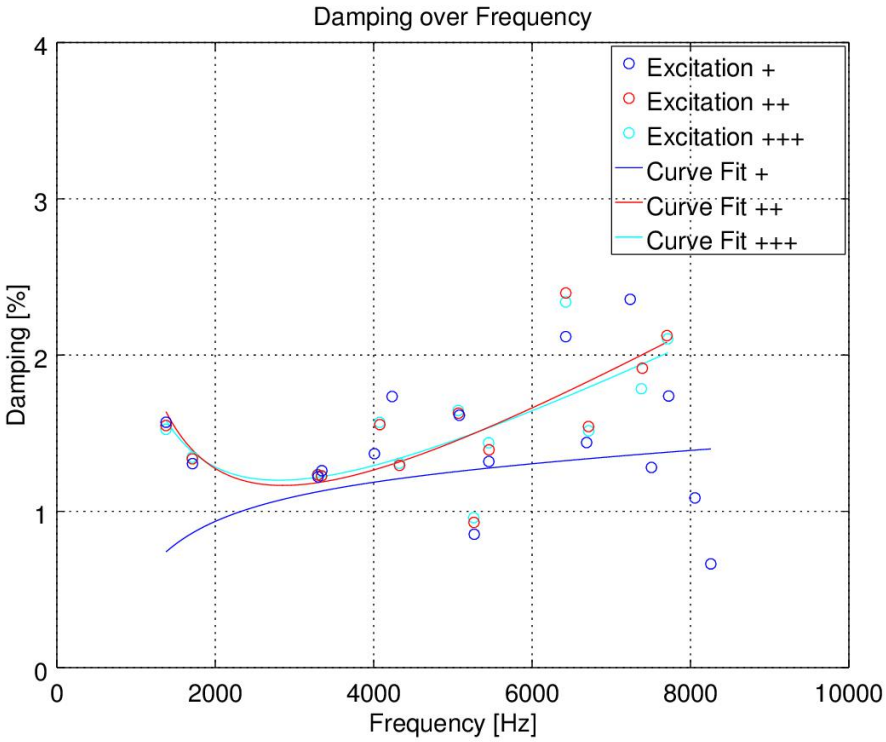

Figure 3.47 – Modal damping

For the lamination stack, there is a palpable deviation in damping between the different mode types. Now it is investigated whether this also applies to the stator. The damping values for the different mode types can be seen in figure 3.48. No clear difference in damping level can be seen between the two different types. It can only be said that the 0-type modes lie closer to the curve fit, apart from the breathing mode. The breathing mode has considerably lower damping.

The deviation of damping values from the curve fit is again analyzed using a box plot (figure 3.49). As for the lamination stack, the median of the 0-type modes at -1.68% ($N_0 = 14$) is lower than the median for the 1-type modes at 4.63% ($N_1 = 12$). But the notches around the medians which denote an estimate for the uncertainty about the median overlap for the different mode types, which indicates that the deviation do not differ significantly.
The interquartile range of the 1-type modes is larger than for the 0-type modes. For the 1-type modes, the different components of winding, coating and insulation paper have an influence which may lead to the larger deviation range.
The overall median lies at -1.43% ($N_a = 26$).

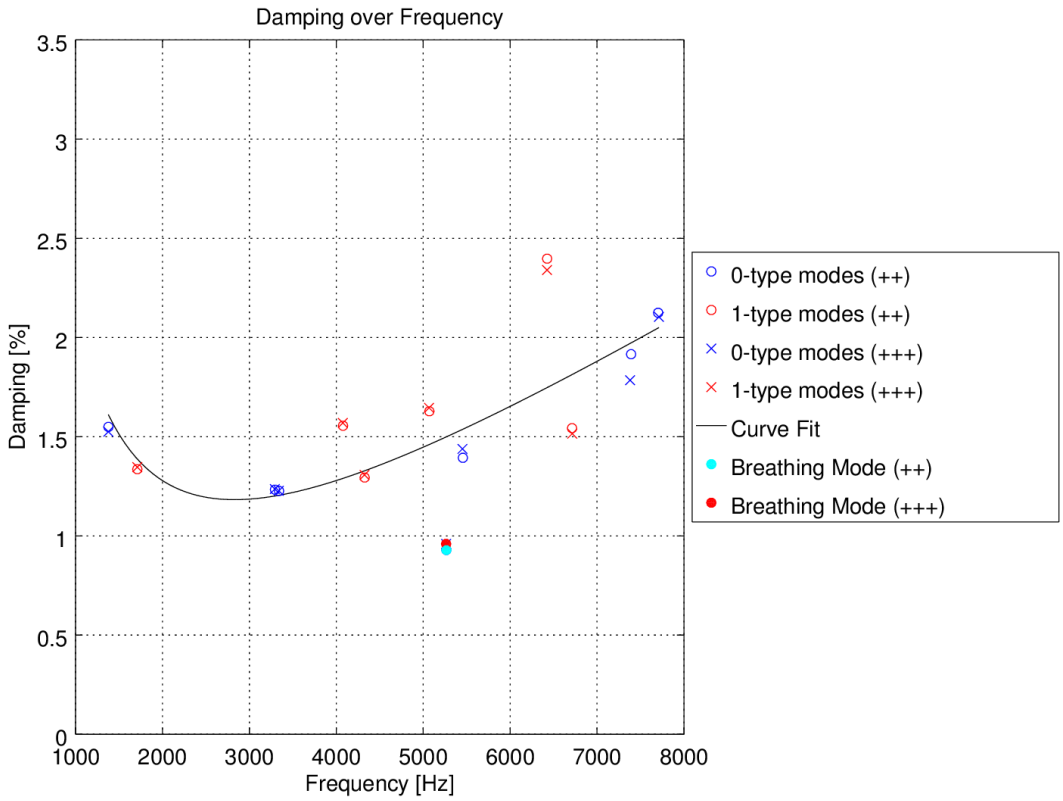

Figure 3.48 – No systematic deviation in damping for different mode types

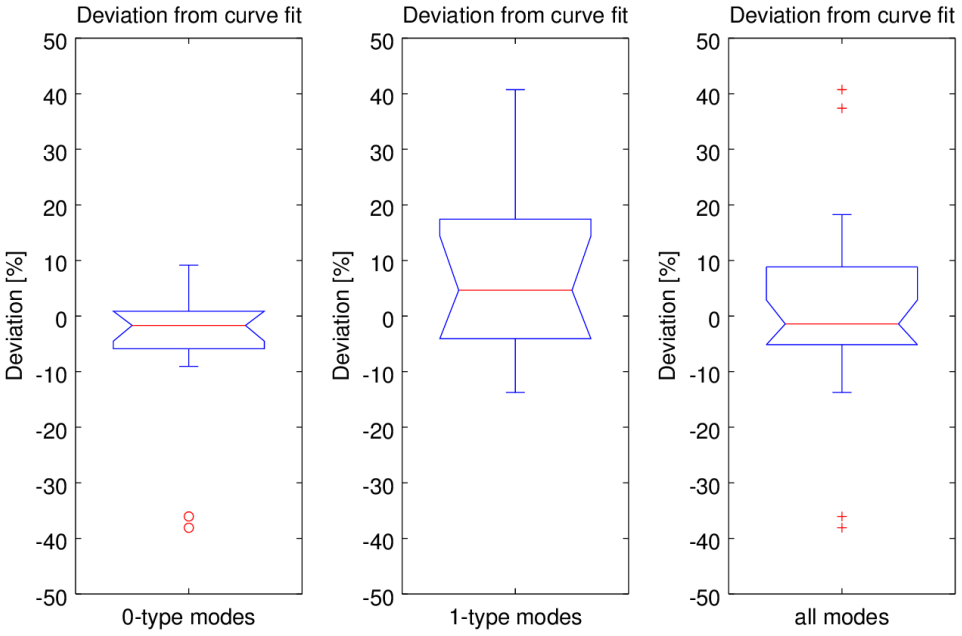

Figure 3.49 – Deviation in damping from curve fit for different mode types

3.3.6 Summary of the Results

The measurement results for the medium and high excitation are coherent and linear up to 8.5 kHz. The low excitation measurement run shows considerable deviations from the other two measurement runs and should therefore be omitted from the validation process of the simulation.

3.4 Stator (HM132)

3.4.1 Measurement Object

Apart from the stator of the range extender, the stator of a second electric machine is examined. Figure 3.50 shows a sketch of the stator
The iron core again consists of laminated sheets (light grey) with slightly different mechanical properties. The copper windings (orange) run through the slots and are wound together at both ends of the stator to build the end windings. The windings are fixated with a paper bandage (yellow) and coated in varnish.

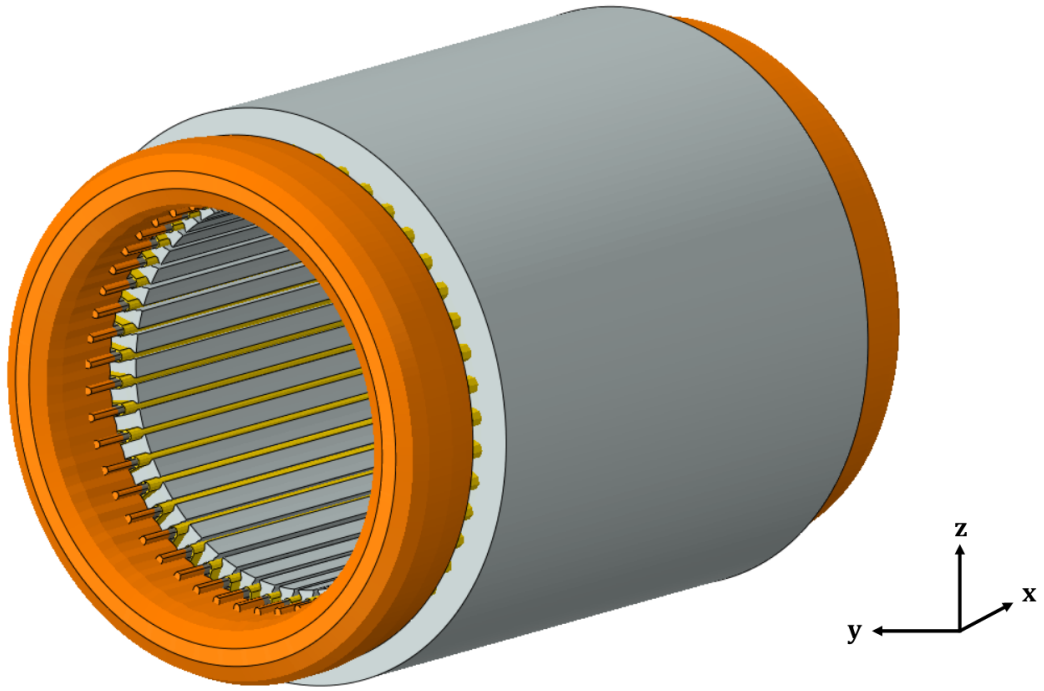

Figure 3.50 – Geometry of the stator

3.4.2 Measurement Set-up

The measurement object is hung on elastic ropes to create a free oscillation.
The excitation was performed using an impulse hammer in different directions of space. In Y directions two different excitation positions were used - one at the middle of the stator (Y2) and one near the end (Y1). Unfortunately, there are no measurements on different force levels available.
The measurement was conducted using 53 1-D acceleration sensors and one 3-D acceleration sensor.

3.4.3 Coherence

As with the other measurement objects, the mean over the coherence from all measurement points for the different measurement runs was calculated to assess the overall coherence. The frequency range in which the coherence lies over 0.9 (marked by the horizontal red line in the figures) is of interest for subsequent analysis.
For the display the whole measurement frequency range from 0 Hz to 12.8 kHz is chosen. Regarding figure 3.51 it can be seen that the coherence lies above 0.9 in the frequency range up to about 5.5 kHz for the XYZ excitation. As this range is rather small for the subsequent validation, the frequency range is expanded for the further measurement analyses up to 8.5 kHz where the coherence is above 0.8. In the course of the analysis it will be determined whether the data above 5.5 kHz can be used for simulation validation.

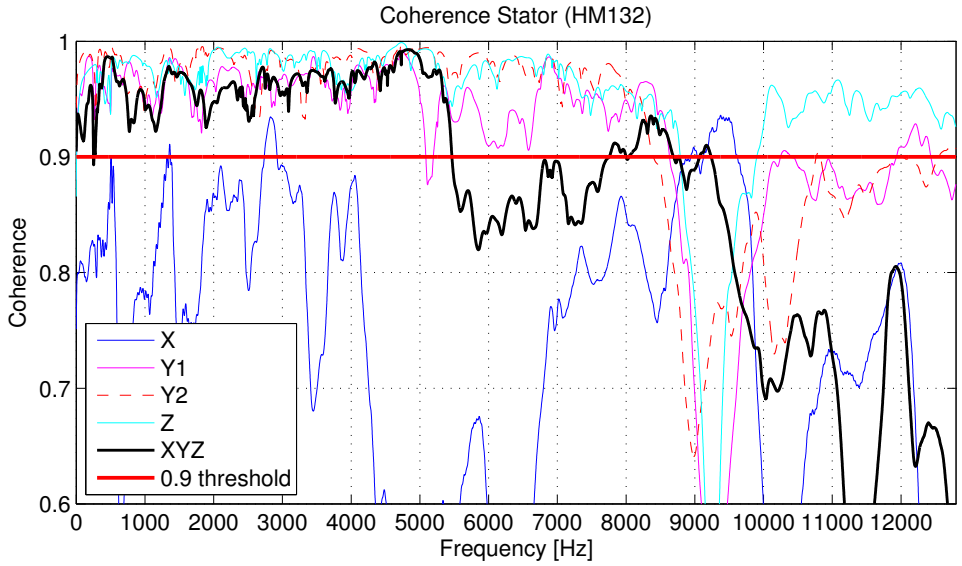

Figure 3.51 – Coherence stator

3.4.4 Quality of Sensor Positioning

Whether the chosen sensor positions can resolve all mode shapes of interest, is assessed using the AutoMAC of a simulation run. As in the simulation a very high number of modes are found, the MAC table is very large which makes scaling the diagram difficult. The frequency axes show only every seventh frequency value in order to increase readability. The compared mode frequencies lie in the range from 544 Hz to 8008 Hz. Nonetheless, it can be seen in figure 3.52 that the AutoMAC resembles the unit matrix with some higher MAC values off the main diagonal. Therefore, not all possible mode shapes can be resolved. Especially at higher frequencies, the spatial resolution of the sensors does not suffice to measure the mode shapes aliasing-free.

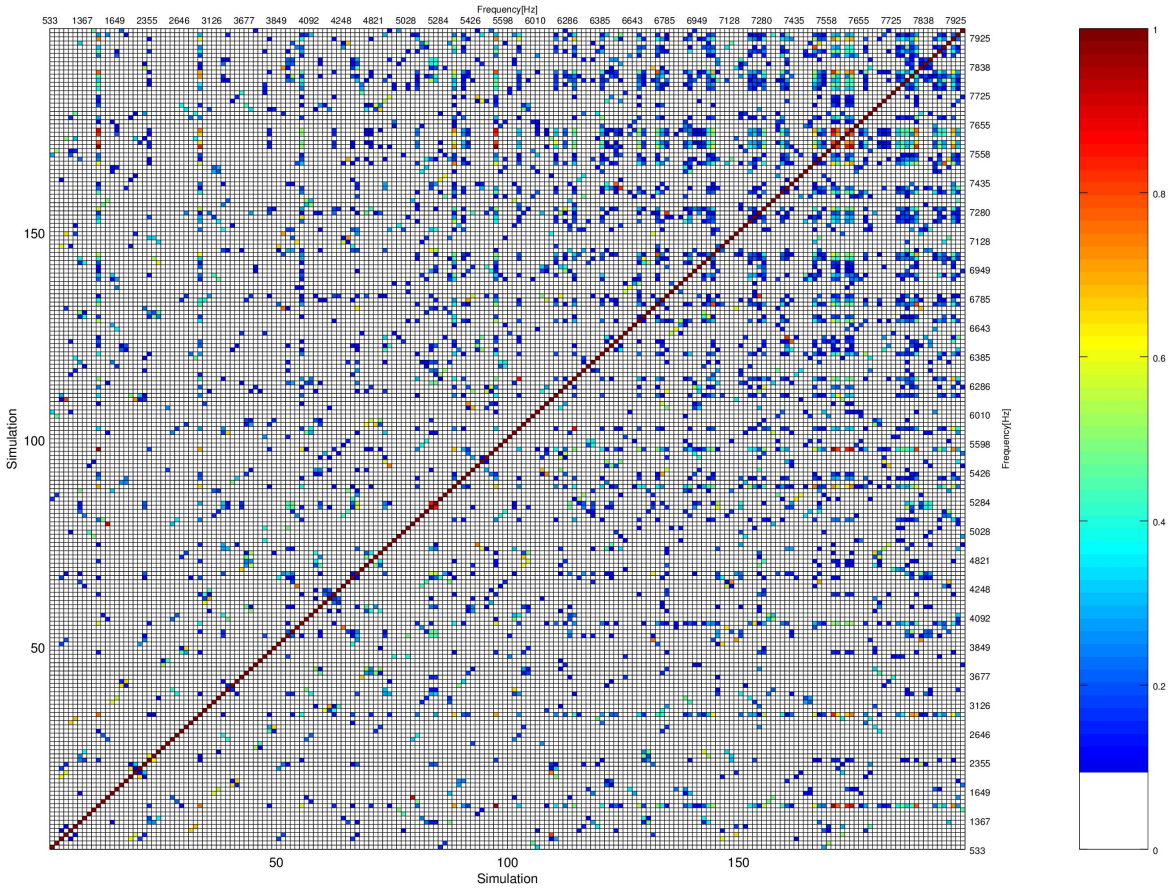

Figure 3.52 – AutoMAC stator

To definitely distinguish the mode shapes, they should have no values above 0.3 outside the main diagonal in the AutoMAC. When limiting the AutoMAC to the range up to 7 kHz and looking at the values off the main diagonal, only three modes conform to the 0.3 criterion. When relaxing the constraint to 0.4, there are 19 modes that can be clearly distinguished.
The chosen sensor positions do not suffice to uniquely identify all possible mode shapes.

3.4.5 Directions of Excitation

MAC comparison. The mode shapes excited by the different excitation directions are compared using the MAC.
The figures 3.53, 3.54 and 3.55 show the comparison between each of the single excitation directions and the combined excitation XYZ. It can be seen that there is not much agreement in the mode shapes between the different measurement runs. Especially the comparison of Y and XYZ excitation lacks compatible modes.

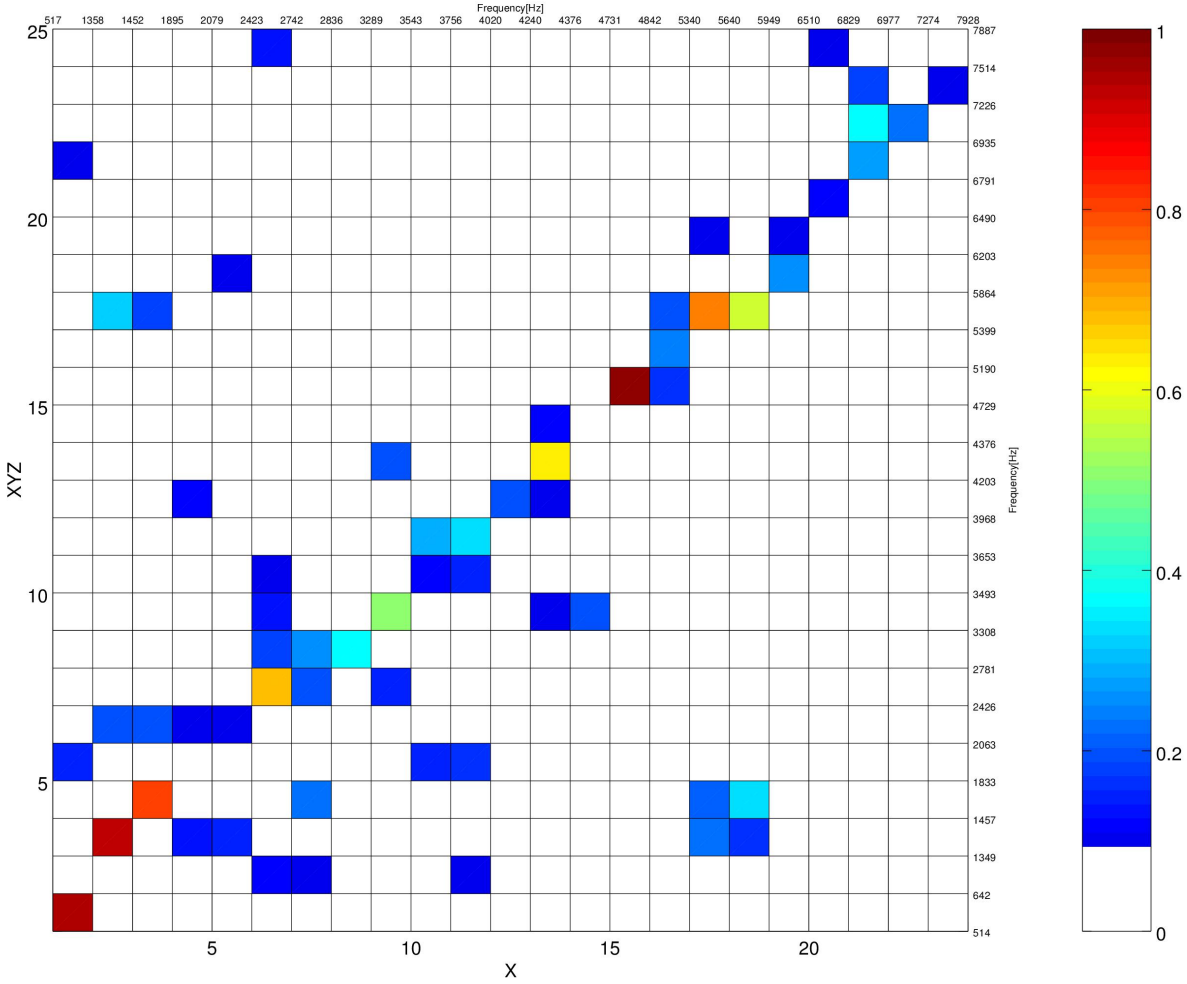

Figure 3.53 – MAC of the measurements with excitation in X and in XYZ direction for the stator

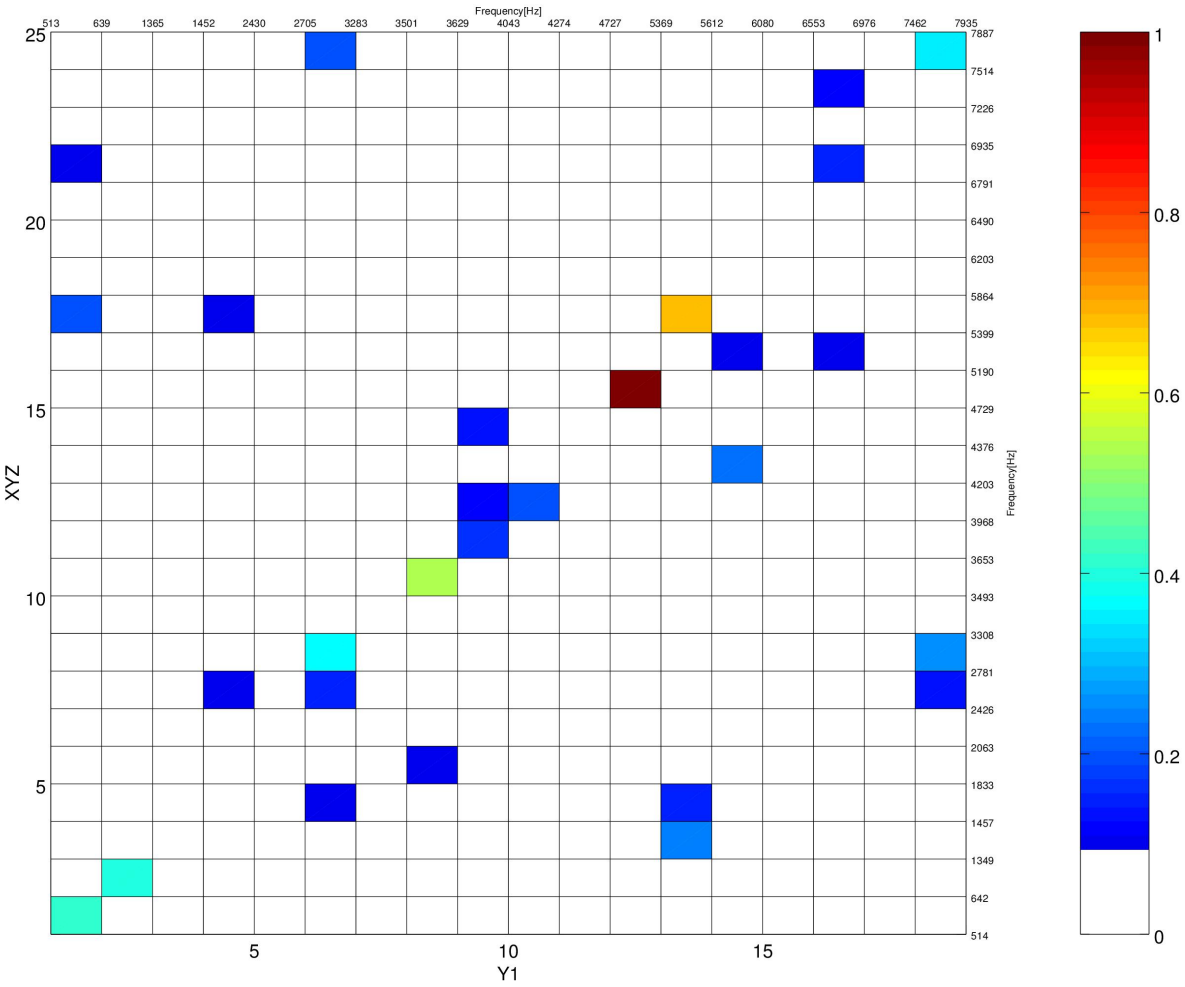

Figure 3.54 – MAC of the measurements with excitation in Y (position 1) and in XYZ direction for the stator

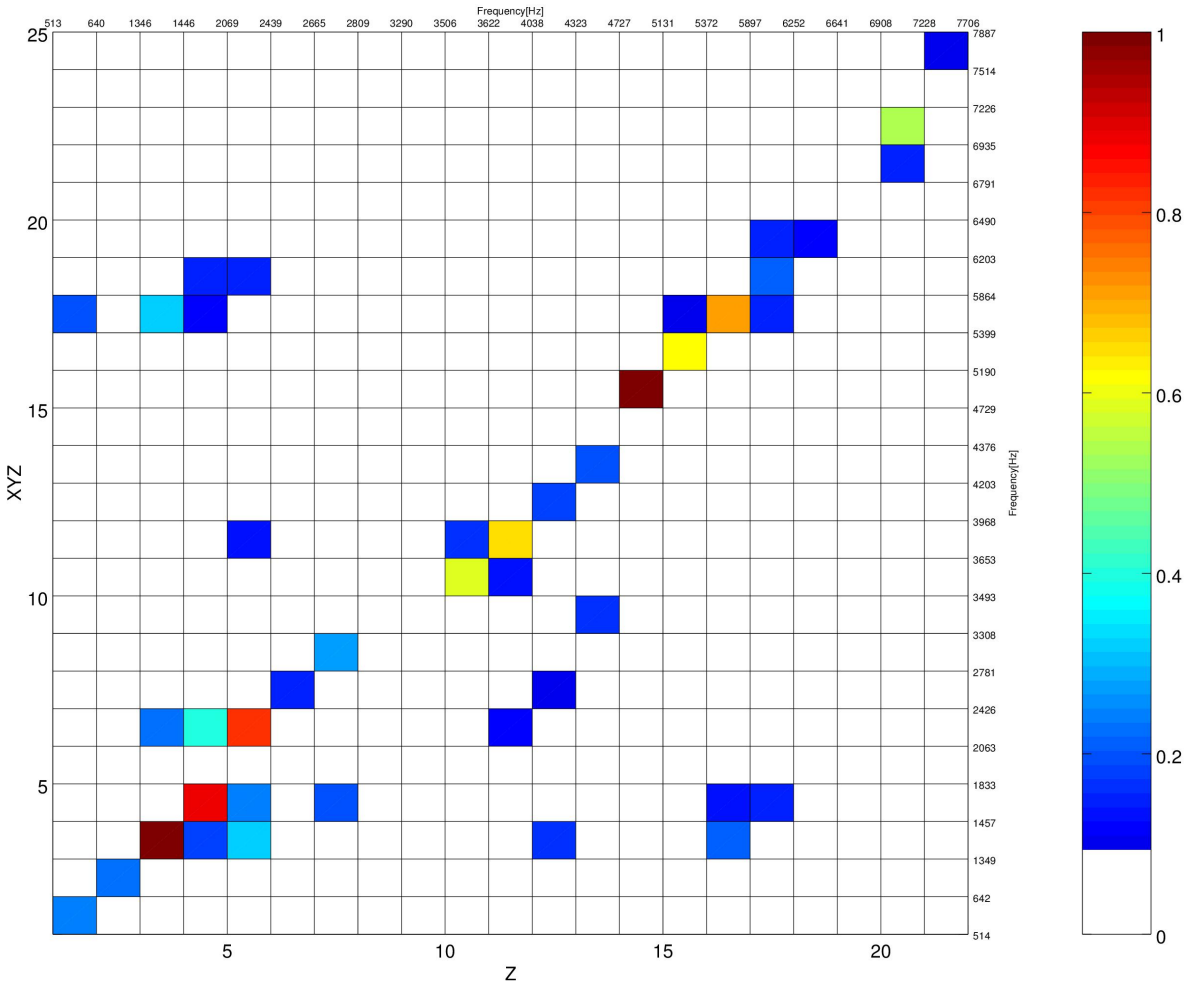

Figure 3.55 – MAC of the measurements with excitation in Z and in XYZ direction for the stator

Figure 3.56 compares the mode shapes of the two measurement runs with Y excitation with different hammer positions. The agreement among these two runs is higher but there are still not many matches.

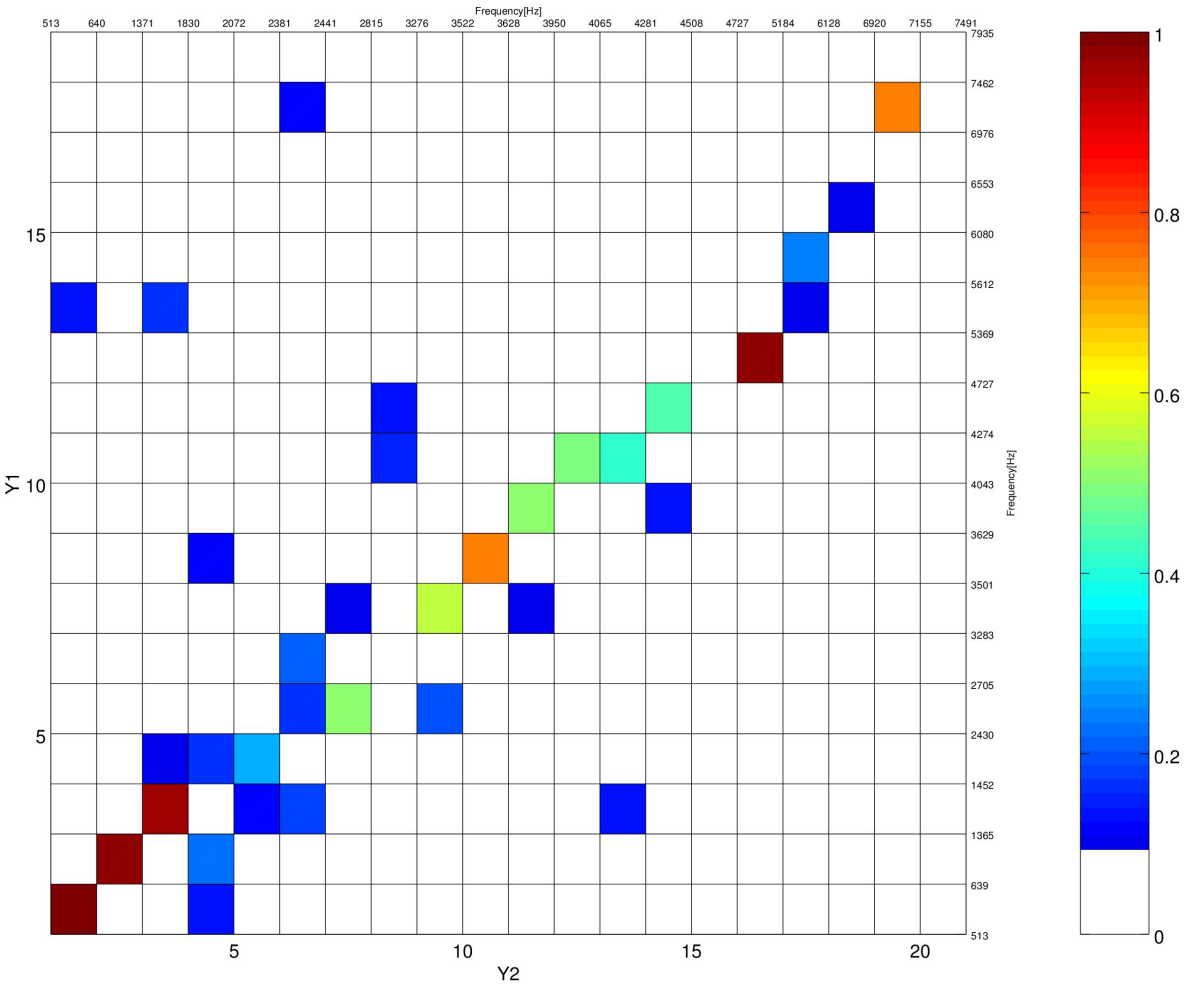

Figure 3.56 – MAC of the measurements with excitation in Y direction (2 different positions) for the stator

Frequency comparison. As there are not many mode pairs with a MAC above 0.7, the comparison of eigenfrequencies is not done graphically but using table 3.5. There the mode frequencies with MAC values above 0.7 are listed along with their shape classification and the deviation of frequencies calculated using equation 3.2. The classification used earlier is expanded to describe the axial deformation more detailed. The second classification number now states the number of zero crossings of the shape along the axial direction of the stator. For the last two modes the shape could not be classified clearly, therefore the missing data is replaced by an "X".
In some cases the mode pairs did not have a high MAC although their shape is classified the same and the eigenfrequencies are close to each other. This means that in the mode shape identification process the two possible manifestations of the shape which are rotated differently in space were detected for different measurement runs.

For the calculation of the frequency deviation the frequencies of both manifestations are used.

XYZ [Hz]	X [Hz]	Y1 [Hz]	Y2 [Hz]	Z [Hz]	Deviation [%]	Shape (-,-)
514	517	513	513	513	0.36	(2,0)
		639	640		0.08	(2,1)
1349	1358	1365	1371	1346	0.90	(3,0)
1457	1452			1446	0.39	(3,1)
		3501	3522		0.30	(2,2)
4729	4731	4727	4727	4727	0.04	(0,1)
5399	5340			5372	0.55	(6,X)
		6976	6920		0.40	(1,X)

Table 3.5 – Mode frequencies of matching mode shapes

The matching mode frequencies lie close to each other, the deviation is below 1% in all cases.

In section 3.4.4 is stated that only 19 mode shapes can be distinguished sufficiently well with the available sensor positions. When intersecting these 19 mode shapes with the eight matching modes, only three modes remain:

— (2,0) at $\approx 514\,\mathrm{Hz}$
— (0,1) at $\approx 4729\,\mathrm{Hz}$
— (1,X) at $\approx 6935\,\mathrm{Hz}$

Still, the modes listed in table 3.5 match each other by high MAC values and also their frequencies lie very close. Therefore, these modes that could be found in most of the measurement runs are of interest for the validation of the simulation data. One should keep in mind although, that the sensor positioning impairs the validation process.

Frequency response functions. A comparison of Frequency Response Functions for the different excitation directions is not meaningful, as the different directions go along with disparate excitation positions. These disparate excitation positions lead to mismatched FRFs. This makes the comparison obsolete.

Modal damping. The last step of analyzing the results of the modal analysis is to compare the modal damping of the different measurement runs.
In figure 3.57 the modal damping for each of the mode frequencies are scattered along with the curve fits for each of the excitation directions using the fitting algorithm from section 3.2.7.

It can be seen that the course of the curve fit differs noticeable from measurement run to measurement run. Especially the curves from X excitation and the Y1 excitation show a considerable deviation.
This makes it hard to make a trustworthy statement regarding the modal damping.

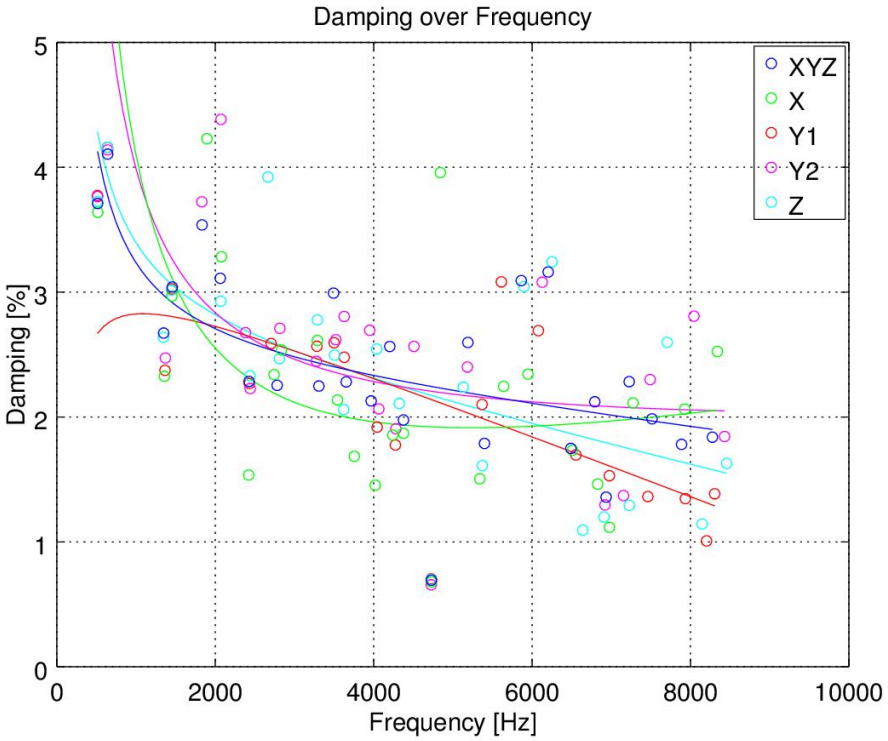

Figure 3.57 – Modal Damping

Nonetheless, the damping is examined to assess if there is a systematic deviation depending on the mode shape.
Figure 3.58 shows the damping for the XYZ excitation measurement run. 0-type modes have a damping lower than the curve fit. The 1-type modes include all modes classified as (X, Y), where $Y \geq 1$ - meaning that there is some deformation along the machine axis.

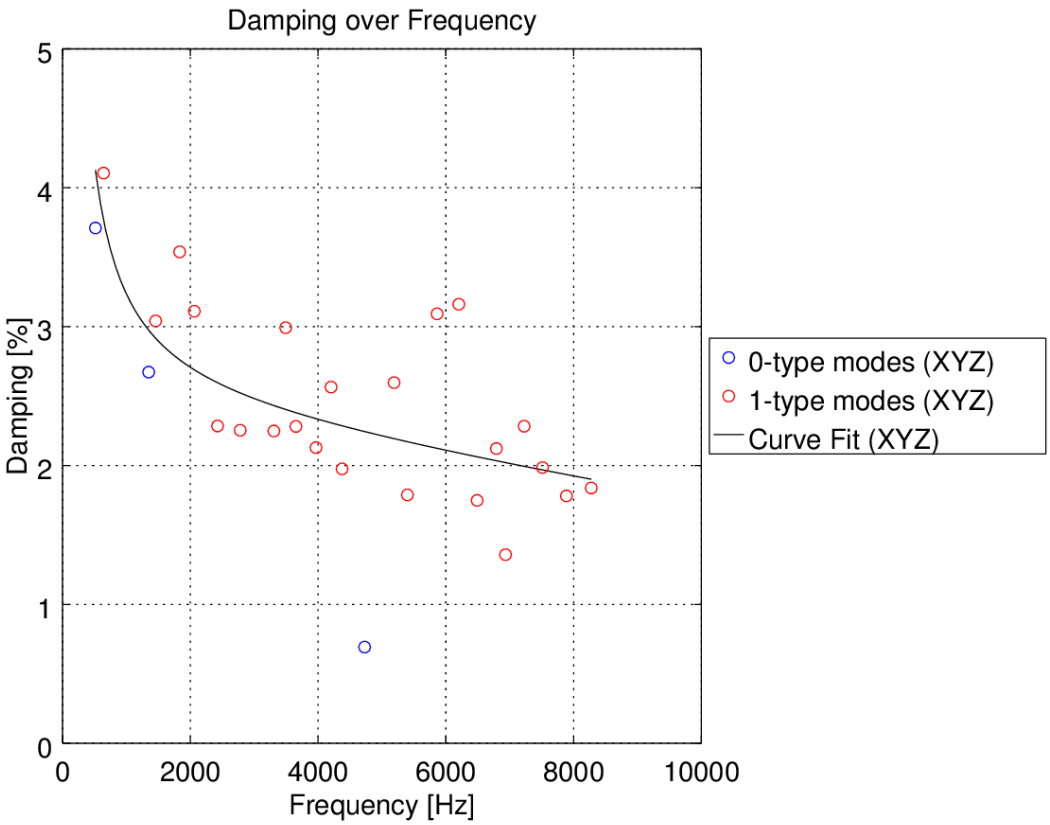

Figure 3.58 – Systematic deviation in damping for different mode types

3.4.6 Summary of the Results

The measurement data of the XYZ measurement run is coherent up to 5.5 kHz. No statement regarding the linearity of the oscillation behavior can be made. Only few mode shapes can be found in multiple of the measurement runs which makes the data less trustworthy as a mean of simulation validation. Therefore the validation of the simulation should be limited to the comparison with the few matching modes.

4 Simulation of Structural Dynamics

After examining the components of the electric machine in detail, the next step is to perform the simulation of the structural dynamics.
The simulation results are subsequently compared to the averaged measurement results of the different components. The validation process includes the comparison of mode shapes, mode frequencies, damping values, and frequency response functions.
The mode shape comparison is performed using one chosen measurement, the other properties are compared to averaged values from all available measurements.

4.1 Simulation Process

The simulation is performed using the software Abaqus (Version Abaqus/CAE 6.14-5) using finite element modeling [37].
The steps of the modeling are listed below.

1. Building of the 3D-model of the component
2. Meshing the model
3. Apply material parameters
4. Perform real-valued eigenvalue extraction (no damping effects)
5. Perform complex-valued eigenvalue extraction (including damping effects)
6. Perform forced response analysis
7. Review material parameters and enhance model by comparing to measurement data

4.2 Lamination Stack

The first component to perform the simulation on is the lamination stack. It is important to understand how to model the base component made of alternating layers of steel and varnish before the more complex components can be analyzed. Especially the modeling of the composite orthogonal material is challenging and not well investigated up to now.

4.2.1 Model

The 3D model is based on a `dxf` file containing the package profile. The profile was then extruded to a thickness of 50 mm.
The mesh consists of 183660 nodes and 155179 hexagonal linear elements with an approximate size of 1.7 mm.
Shape and size metrics to verify the mesh's quality are listed in the appendix.

4.2.2 Material Modeling

Material parameters of components The material of the steel sheets is known, the material parameter's density, Young's modulus and sheet thickness can be found in the manufacturers data sheet and are listed in table 4.1 [38]. The Poisson's ratio is set to a typical value for steel and the shear modulus is calculated from an average Young's modulus and the set Poisson's ratio using equation 2.17.

Material	M250-35A
Sheet thickness	0.35 mm $\pm$ 8%
Density	7600 $\frac{\text{kg}}{\text{m}^3}$
Young's modulus	$185 - 200$ GPa
Poisson's ratio	0.3
Shear modulus	79.3 GPa

Table 4.1 – Material parameters electric sheets

For the synthetic resin, it proved to be more difficult to find reliable material parameters. The first several simulation runs were performed based on material parameters gathered from different data sheets as the actually used material was unknown. The values on these data sheets spanned a wide possible parameter range, especially for the Young's modulus. The Young's modulus used for the first simulations is calculated from the median of the values from the different data sheets.
After some research at the manufacturer, the used resin could be identified (table 4.2). The Young's modulus was not listed in the data sheet so the manufacturer provided data from a tensile shear test of the resin. From these measurement data the shear modulus can be deduced. Unfortunately no Poisson's ratio could be found for this material, therefore it was set to $\nu = 0.4$, based on typical values for epoxy resins. Based on the measurement data and this Poisson's ratio, the Young's modulus was calculated using equation 2.17 solved for E.
It has to be noted that the static tensile shear test determines the shear modulus in a displacement range that is larger than the range in which acoustic displacements usually happen. Therefore, it is not settled whether the measured properties can be applied for the simulation of structural dynamics.

Material	Voltatex 1175W
Layer thickness	$\approx 2 - 5$ µm
Density	$1050 - 1150$ $\frac{\text{kg}}{\text{m}^3}$
Young's modulus	1373 MPa

Table 4.2 – Material parameters varnish (synthetic resin)

As we know, there is a considerable production tolerance on the thickness of the sheets.

Therefore, the exact steel percentage is unknown and can only be estimated. Also the material properties of the varnish are not well known and require a set of simulation runs to investigate the influence of these parameters.

4.2.3 Real-valued Eigenvalue Extraction

In order to examine the vibration behavior of the lamination stack, a series of parameter variations is executed. Not all of these variations will be explained in detail in the following. The focus is put on the variations that lead to a better modeling and a deeper understanding of the vibration behavior.
When performing the first sets of simulations, the correct nominal material parameters were not known. Data about the used material could be acquired only later after contacting the manufacturer. Despite the missing data, parameter studies could be performed to examine the influence of specific material characteristics such as the Young's modulus of the components.
The executed parameter variations based on the only roughly estimated material parameters can be found in table 4.3 along with their descriptions. The name of the variation denotes which parameter has been changed, by which percentage it was changed, and in which direction that change happened - upwards (U) or downwards (D). When a change in the parameter 'Phi' is indicated, it refers to the varnish percentage $(1 - \phi_{St})$.
The variations performed after inserting the updated material parameters are listed in table 4.4. The use of the new material settings is indicated by the abbreviation 'NM'.
The parameter variations of most interest including the nominal parameters are explained in detail in the following.

Name	Description	Changed Parameter
Nom	Nominal parameters	
Phi_50D	Reduction of steel percentage	$(1 - \phi_{St}) + 50\%$
E1_10D	Reduction of Young's modulus in-plane direction	$E_p - 10\%$
E3_10D	Reduction of Young's modulus in axial direction	$E_z - 10\%$
G1_10D	Reduction of Shear modulus	$G_p - 10\%$
G3_10D	Reduction of Shear modulus	$G_{zp} - 10\%$
Nu1_10D	Reduction of Poisson's ratio	$\nu_p - 10\%$
Nu3_10D	Reduction of Poisson's ratio	$\nu_{zp} - 10\%$
Ef_20D	Reduction of Young's modulus of steel (fiber material)	$E_f - 20\%$
Em_20D	Reduction of Young's modulus of varnish (matrix material)	$E_m - 20\%$

Table 4.3 – List of executed simulations with roughly estimated material settings

Name	Description	Changed Parameter
NM Nom	Nominal parameters	Corrected material parameters
NM Phi_20U	Reduction of steel percentage	$(1-\phi_{St})+20\%$
NM Phi_50U	Reduction of steel percentage	$(1-\phi_{St})+50\%$
NM Phi_75U	Reduction of steel percentage	$(1-\phi_{St})+75\%$
NM Phi_95U	Reduction of steel percentage	$(1-\phi_{St})+95\%$
NM Phi_100U	Reduction of steel percentage	$(1-\phi_{St})+100\%$
NM Phi_100U _Em_20D	Reduction of steel percentage Reduction of Young's Modulus of varnish	$(1-\phi_{St})+100\%$ $E_m-20\%$
NM Phi_100U _Em_50D	Reduction of steel percentage Reduction of Young's Modulus of varnish	$(1-\phi_{St})+100\%$ $E_m-50\%$

Table 4.4 – List of executed simulations with updated material settings

Nominal Parameters. As the exact steel percentage is unknown, the first idea is to start from the nominal parameters. This means to assume a varnish layer thickness of 4 µm for every layer. The thickness of the layers is assumed to be 0.35 mm. Equation 4.1 shows the steel percentage for these assumptions. In equation 4.2 the nominal sheet thickness is indicated.

$$\phi_{St,Nom} = \frac{350\,\mu m - 4\,\mu m}{350\,\mu m} = 98.86\,\% \tag{4.1}$$

$$l = 350\,\mu m - 4\,\mu m = 0.346\,mm \tag{4.2}$$

The material parameters of the homogenized orthotrop material can be calculated using equations 2.18 to 2.24. As was said before, initially, only rough estimations of the material properties were available and used for the simulation. These material properties along with the updated properties are listed in table 4.5. The simulations performed using the new material settings are explained in detail later on.

Quantity	Unit	Value (old)	Value (new)
ρ_f	$\frac{kg}{m^3}$	7650	7600
ρ_m	$\frac{kg}{m^3}$	1200	1100
E_f	MPa	210000	185000
E_m	MPa	3500	1373
ν_f	-	0.3	0.3
ν_m	-	0.3	0.4

Table 4.5 – Comparison of old and new material parameters

The result of the nominal simulation run using the rough parameter estimation is not shown, as these settings do not lead to reliable results - as is expected. The values that are inserted in Abaqus for this simulation run can be found in the appendix (table B.1).

Variation of sheet thickness. The steel percentage ϕ_{St} depends on the layer thickness. When the varnish layer thickness is greater than the assumed 4 µm, the homogenized properties change.
For this variation the varnish layer thickness is set to $l_V = 6\,\mu m$, which is within the range of possible values. Equation 4.3 shows the steel percentage for this case.

$$\phi_{St,6\,\mu m} = \frac{350\,\mu m - 6\,\mu m}{350\,\mu m} \qquad = 98.29\,\% \tag{4.3}$$

The influence of this change in steel percentage on the material parameters varies depending on the orientation. A change in steel percentage below 1% from 98.86 $\%$ to 98.29 $\%$ leads to a variation of E_z, ν_{zp} and G_{zp} of more than 16%. The resulting material properties can be found in the appendix (table B.1).

Changing the steel percentage mainly influences the frequencies of 1-type modes, 0-type modes are much less affected.

The result of this simulation run is not shown, as the roughly estimated material settings do not lead to reliable results.

Variation of single parameters of the homogenized material. The parameters entered in Abaqus (E_p,E_z,ν_p,ν_{zp},G_p,G_{zp}) are reduced one by one by 10% to investigate their influence on the mode shapes and frequencies. The dependency between the different values is omitted for this investigation.
The results are not explained in detail - yet they were useful for the decision which further variations to execute.

Variation of the Young's moduli of steel sheets and resin. The Young's moduli of the steel sheets E_f as well as the varnish E_m are separately reduced by 20%. The resulting material parameters are listed in the appendix in table B.2.
As the percentage of steel is much higher than the percentage of varnish, the variation of E_f leads to a larger change in parameters.

The Young's modulus of the steel sheets E_f has a considerable influence on all mode frequencies. The package consists mainly of steel, therefore a change in its stiffness properties has an overall large impact.
The Young's modulus of resin on the other hand influences mainly the mode frequencies of 1-type modes. For 0-type modes the stiffness of the steel sheets is the predominant factor.

Varying the Poisson's ratios of the two components had no considerable influence on the mode frequencies.

New Material Parameters. At this point the material data from the manufacturer became available and new simulations could be executed. The now used values for the Young's moduli are considerably reduced in comparison to the values used before. The reduction of the Young's modulus of the sheets influences the frequency position of all eigenfrequencies. All eigenfrequencies are reduced. The reduction of the Young's modulus of the varnish lowers mostly the eigenfrequencies of mode shapes of type one, the other modes are only slightly influenced.

With these new values an updated set of nominal parameters can be applied. These nominal parameters can be found in table 4.6.

Quantity	Unit	Nom
ρ	$\frac{\text{kg}}{\text{m}^3}$	7526
E_p	GPa	190.3
E_z	GPa	74.3
ν_p	-	0.3011
ν_{zp}	-	0.1176
G_{zp}	GPa	27.3
G_p	GPa	73.1

Table 4.6 – Nominal material parameters with the new material data

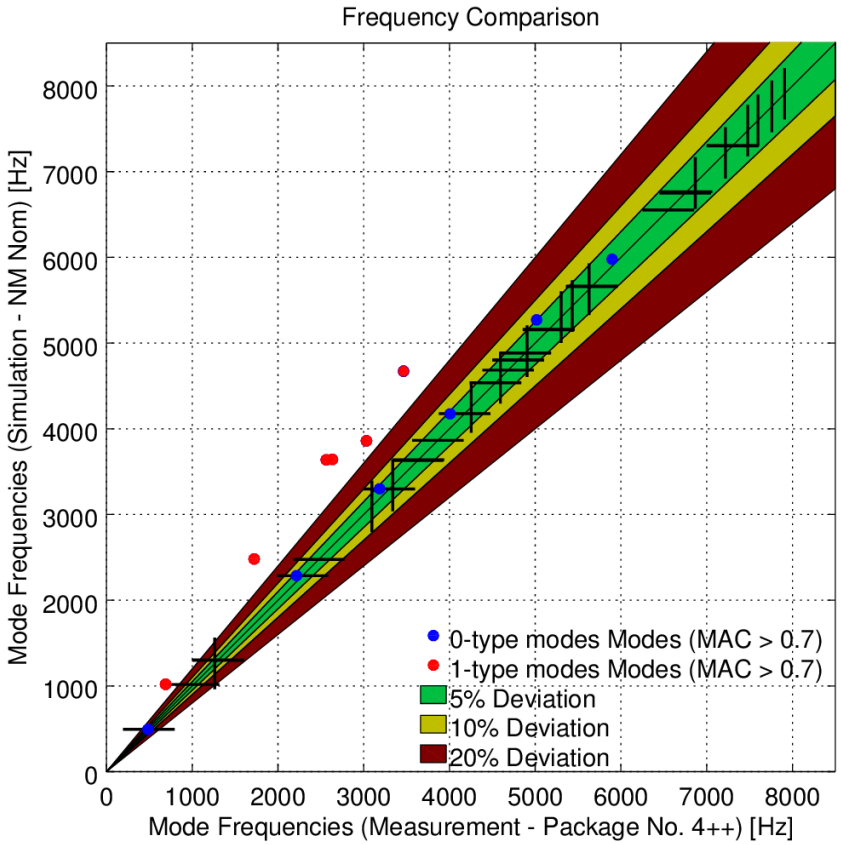

Figure 4.1 – Frequency Comparison - new material parameters (nominal)

Setting of the resin layer thickness to $8\mu\mathrm{m}$. As the eigenfrequencies for the 1-type modes are still too high (figure 4.1), the varnish layer thickness is increased to 8 µm. With these values the 1-type mode frequencies lie approximately 20 % above the measured frequencies (figure 4.2).

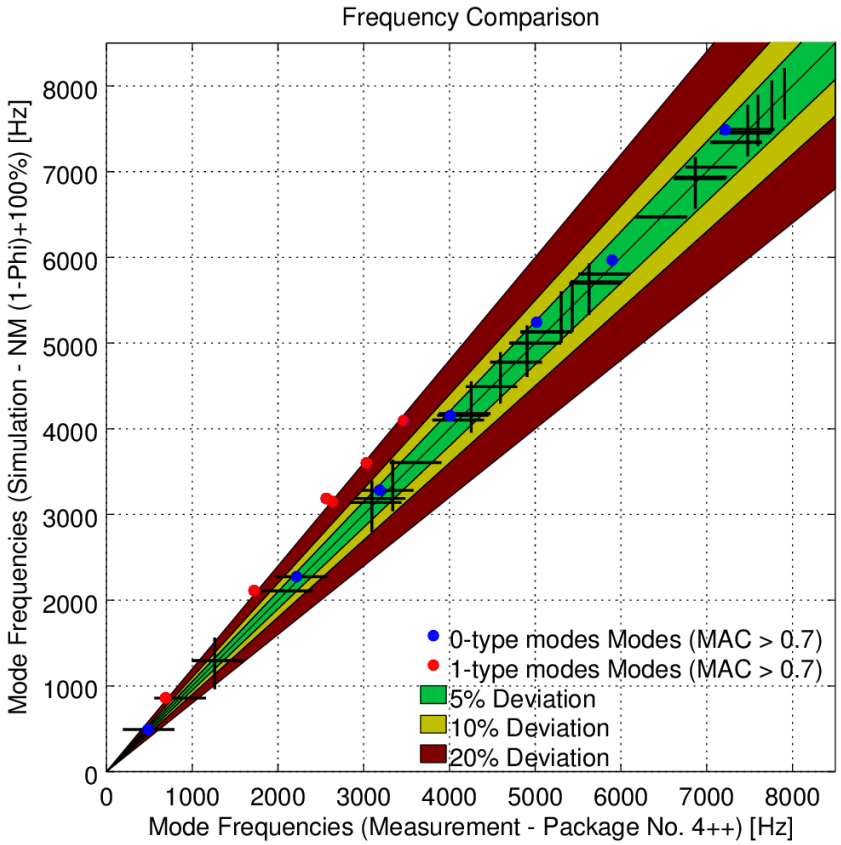

Figure 4.2 – Frequency Comparison - New Material Parameters - 8 µm varnish layer thickness

Parameter variation for adjustment to the measurement. As the increase of the varnish layer thickness did not suffice to get simulation results matching the measurement, the Young's modulus of the varnish is again reduced in order to fit the mode frequencies. For acceptable matching the Young's modulus is reduced by 50 %. This goes in concordance with the assumption, that the stiffness properties of the resin gathered from the tensile shear test are not directly applicable in the simulation of structural dynamics. The frequency comparison between the measurement and the optimized simulation can be seen in figure 4.3.

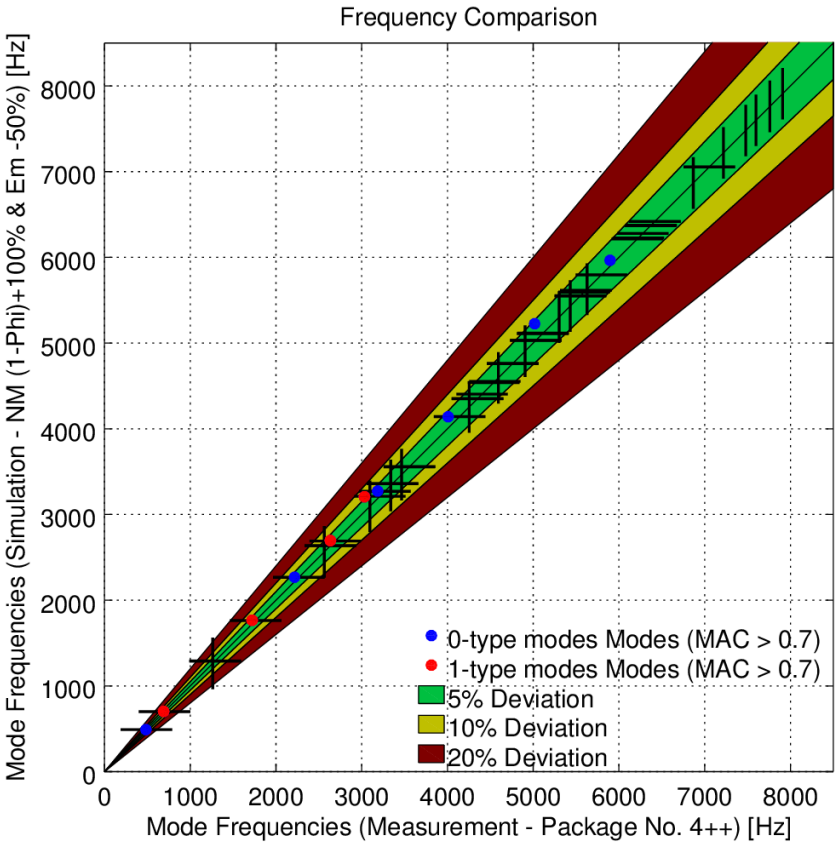

Figure 4.3 – Frequency Comparison - New Material Parameters - 8 µm varnish layer thickness and reduced Young's modulus E_m

Quantity	Unit	Nom	8 µm	8 µm $E_m - 50\%$
ϕ_f	%	98.86	97.71	97.71
E_m	GPa	1.4	1.4	0.7
ρ	$\frac{kg}{m^3}$	7526	7451	7451
E_p	GPa	190.3	188.1	188.1
E_z	GPa	74.3	46.0	26.1
ν_p	-	0.3011	0.3023	0.3023
ν_{zp}	-	0.1176	0.0740	0.0419
G_{zp}	GPa	27.3	16.7	9.4
G_p	GPa	73.1	72.2	72.2

Table 4.7 – Material parameters for the different parameter studies with the new material data

The deviation of the simulation mode frequencies from the averaged mode frequencies can be seen in detail in table 4.8. Apart from one case, all deviations lie in the range from $-5\,\%$ to $5\,\%$ (marked green). The one mode at 3032 Hz, where the deviation is beyond this range (marked yellow), can only be found in the measurement of package No.4. In general the mode frequencies are rather overestimated than underestimated, yet a further reduction of stiffness is not plausibly allegeable and the modeling is sufficiently good.

∅ Measurement [Hz]	Simulation [Hz]	Deviation [%]	Shape (-,-)
483	490	1.52	(2,0)
720	702	-2.42	(2,1)
1788	1766	-1.24	(3,1)
2215	2269	2.44	(4,0)
2672	2696	0.91	(4,1)
3032	3207	5.78	(1,1)
3183	3274	2.83	(5,0)
4009	4140	3.26	(6,0)
5011	5225	4.28	(9,0)
5899	5965	1.12	(0,0)

Table 4.8 – Comparison between the averaged measurement mode frequencies and the simulation mode frequencies

4.2.4 Complex-valued Eigenvalue Extraction

For the complex eigenvalue analysis the material has to be assigned a damping value. The material damping is defined using the Rayleigh damping coefficients.
The values are chosen based on the measurement results and can be seen in equations 4.4 and 4.5.

$$\alpha = 187.92\,\frac{1}{\mathrm{s}} \tag{4.4}$$

$$\gamma = 1.8327 \times 10^{-7}\,\mathrm{s} \tag{4.5}$$

When looking at the modal damping of the simulation results in figure 4.4 it can seen, that the damping for all of the eigenfrequencies lie on the curve. There is no difference observable between different mode shapes as is was in the measurement results.
The direction dependent stiffness behavior unfortunately does not effect the modal damping although the factor γ is stiffness proportional using this FE-tool.

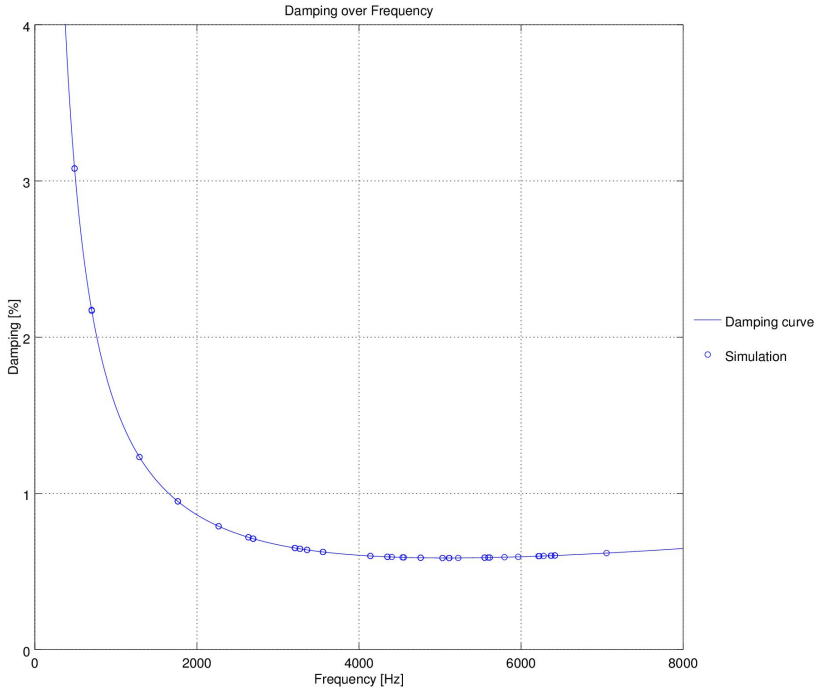

Figure 4.4 – Modal damping in complex eigenvalue analysis

The direction dependent damping behavior the lamination stack exhibits cannot be modeled using this FE-tool. This was confirmed after contacting the publisher's service desk.

4.2.5 Forced Response Analysis

In order to acquire a frequency response function that can be compared to the measurement results, a force of 1 N is applied to the node that lies closest to the position where the hammer excitation happened in the experimental modal analysis. This way the output data can directly be interpreted as FRF data.
The FRF is displayed in terms of velocity for the three sensor positions used in the comparison of measured FRFs complemented by one further sensor inside the stator slot (vR6_160). The measurement range includes the FRFs of the five different laminated packages.
Between the measurement and the simulation a difference in level of approximately 13 dB is observed. This is the case in all measurement-simulation comparisons. The origin of this deviation could not be determined.
In the display of FRFs the factor of 13 dB is added to the simulation data in order to calibrate them for the comparison.
The damping is again defined using the Rayleigh coefficients from equations 4.4 and 4.5.

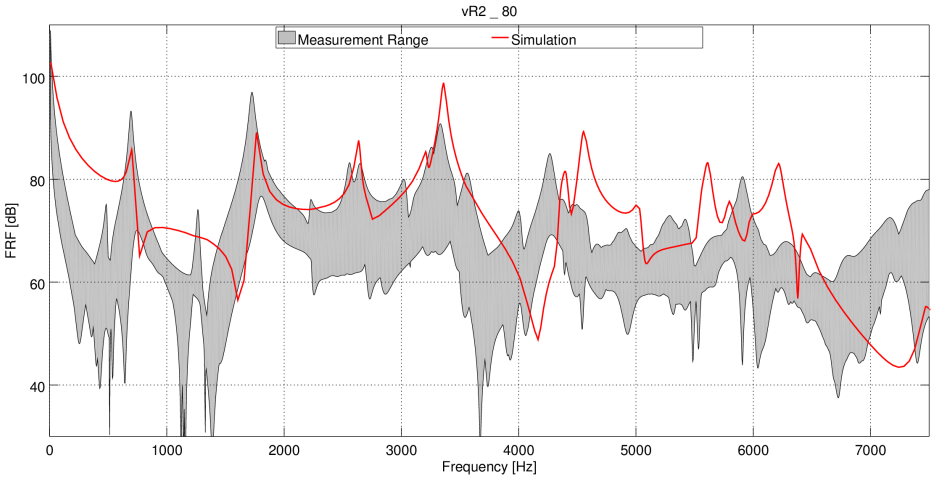

(a) FRFs at sensor vR2_80

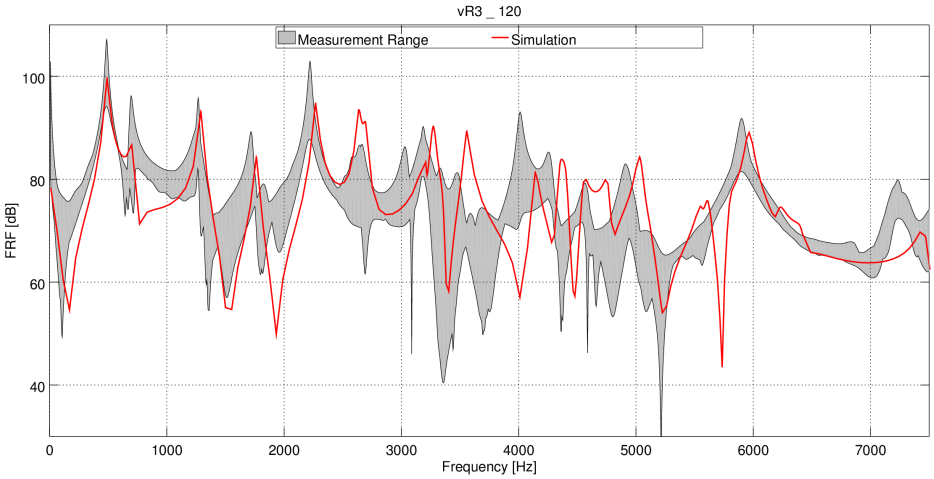

(b) FRFs at sensor vR3_120

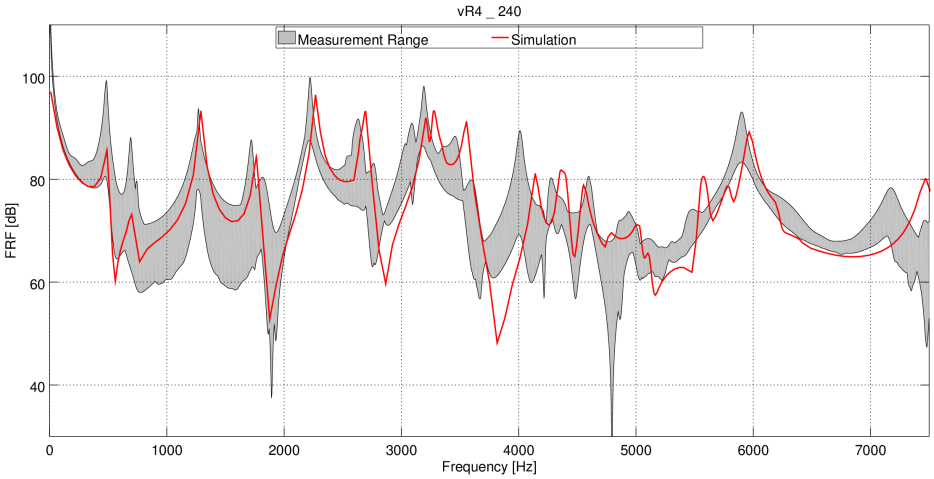

(c) FRFs at sensor vR4_240

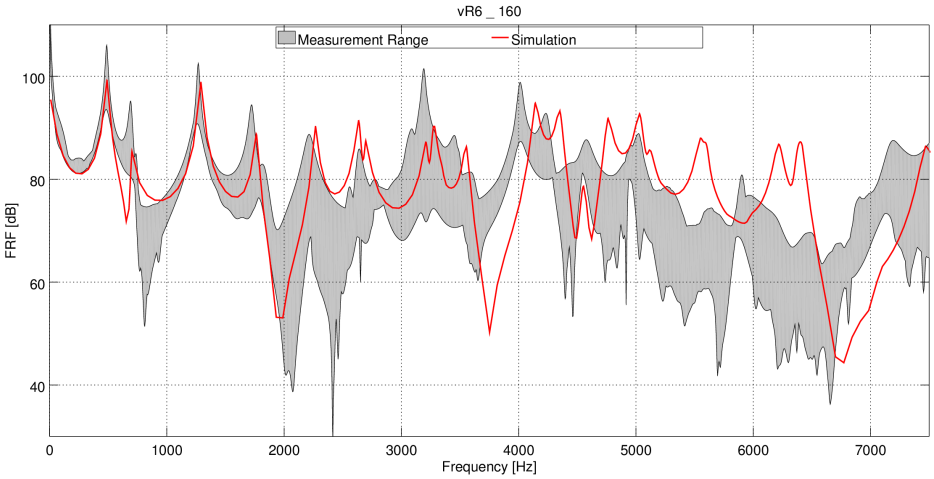

(d) FRFs at sensor vR6_160

Figure 4.5 – FRF comparison measurement/simulation at four different sensor positions

As this modeling cannot reproduce the effect of higher and lower modal damping for the different mode types, a systematic error is made in the calculation of the FRF. This error expressed in terms of dB can be seen figure 4.6. The error is displayed along with the exemplary FRF at sensor vR2_80, as the error is the same for all FRFs. The range from the minimum to the maximum error per mode derives from the widely scattered damping values from the different measurements.

Although there is a considerable systematic error in the calculation of the FRFs, the qualitative course of the simulated FRF matches the measurement. It can be seen that for some frequencies the resonance frequencies do not lie on top of each other, yet the overall behavior can be described well.

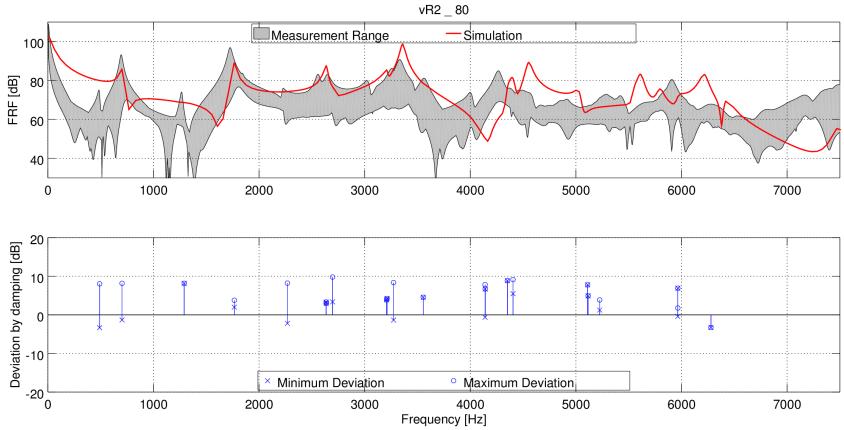

Figure 4.6 – FRF and deviation in damping due to systematic modeling error

4.2.6 Summary of the Results

Transverse isotropic modeling of the laminated sheets leads to a good approximation of mode frequencies, the deviation from the measurement lies mostly below 5%.
The volume percentage and the properties of the insulating varnish have a considerable influence - especially on modes of type 1. Therefore, these properties should be determined with high accuracy before performing the simulations.
Direction dependent modeling of the damping could not be implemented, therefore a systematic error is made in the calculation of modal damping and frequency response functions. A consideration of the direction dependent damping behavior should be attended to in future projects.

4.3 Stator (Range Extender)

After simulating the lamination stack, the stator of the range extender can be examined. As the behavior of the iron core is now known, the influence of windings and coating are to be investigated.

4.3.1 Model

The 3D model is based on the iron core model which is then expanded by including the windings and the coating. The insulating paper between sheets and windings is omitted at first to investigate whether this simplification is applicable. Later on a second model is built with a layer of paper included for comparison.
The mesh of the model without paper consists of 1560639 nodes and 1087666 elements. For the model including the paper, the mesh contains 1975758 nodes and 1651519 elements.

A tabular enumeration of the element types used in the meshes for the stator models can be found in table 4.9.

Element type	Model without paper	Model with paper
linear hexahedral	366696	127194
linear tetrahedral	-	299576
quadratic tetrahedral	720970	1224749

Table 4.9 – Used element types in the stator models without and with paper

The element types influence the accuracy of the model and its convergence rate. Hexahedral elements lead to equal accuracy as tetrahedral elements at less computational cost, given their shape is approximately rectangular. If the modeled structure is too complex for hexahedral elements, tetrahedral elements should be used. The interpolation between the nodes of the elements is either linear or quadratic. Further information can be found in [37] and [39].

4.3.2 Material Modeling

Material parameters of components. For the lamination stack, the properties determined in the adaptation process in section 4.2.3 are used.
The coating data is based on the manufacturer's data sheet. In the sheet only the density and the hardness of the coating were defined. Therefore, the Young's modulus and the Poisson's ratio had to be estimated. The estimation of the Young's modulus E is based on the approximation equation 4.6 using the hardness S_D [40]. Because no other data was available, the Poisson's ratio of the coating is set to 0.4. The data used for the simulation can be seen in table 4.10.

$$S_D = 100 - \frac{20\left(-78.188 + \sqrt{6113.36 + 781.88E}\right)}{E} \tag{4.6}$$

Material	Epoxylite EIP 4260
Density	1680 $\frac{\text{kg}}{\text{m}^3}$
Young's modulus	2806.9 MPa
Poisson's ratio	0.4

Table 4.10 – Material parameters coating

The windings were modeled as a composite from copper and the coating material using the homogenization equations for windings introduced in section 2.5. The mechanical properties of copper can be found in table 4.11.
The properties of the insulating paper were taken from literature and adopted based on another stator (table 4.12).

Material	Copper
Density	8920 $\frac{\text{kg}}{\text{m}^3}$
Young's modulus	100 GPa – 130 GPa
Poisson's ratio	0.345

Table 4.11 – Material parameters copper

Material	Paper
Density	1020 $\frac{\text{kg}}{\text{m}^3}$
Young's modulus	100 MPa
Poisson's ratio	0.3

Table 4.12 – Material parameters insulating paper

4.3.3 Real-valued Eigenvalue Extraction

Performed Variations of Material Parameters (without paper) The parameter studies that were performed on the stator model without paper are listed in table 4.13. Again, the name states which parameter has been changed, by which percentage and in which direction. 'Phi' refers to the copper percentage ϕ_{Cu}, the index 'C' indicates a change of the properties of the coating. The abbreviation 'WOP' stands for 'without paper'.

Performed Variations of Material Parameters (with paper) The parameter studies that were performed on the stator model with paper are listed in table 4.13. The naming convention is the same as before. The abbreviation 'WP' stands for 'with paper'.

Nominal parameters. The starting point for the parameter variation are the nominal parameters gathered from the data sheets and the previous simulation.

Name	Description
WOP Nom	Nominal parameters
WOP Phi_20D	Copper percentage reduced by 20%
WOP Phi_20U	Copper percentage increased by 20%
WOP EC_20D	Young's modulus of coating reduced by 20%
WOP EC_20U	Young's modulus of coating increased by 20%
WOP nuC_20D	Poisson's ratio of coating reduced by 20%
WOP nuC_20U	Poisson's ratio of coating increased by 20%
WOP nuC_22.5U	Poisson's ratio of coating increased by 22.5%
WOP EW_10D	Copper percentage in end windings reduced by 10%
WOP EW_10U	Copper percentage in end windings increased by 10%
WOP xiE_50D	Adjustment factor reduced by 50%
WOP xiG_100D	Adjustment factor reduced by 100%
WOP xiG_100U	Adjustment factor increased by 100%

Table 4.13 – List of executed simulations (model without paper)

The copper percentage ϕ_{Cu} was estimated using half the cross-sectional area of the slot A_S and the diameter of the windings. The used slot area is illustrated in figure 4.7.
The windings consist of two pairs of wires with different diameters D_{W1} and D_{W2}. With these values and the number of windings N_W, the total winding area A_W can be calculated (equation 4.7).
The slot area A_S differs from the model without paper to the model with paper, therefore the copper percentage has to be adjusted. The different values are denoted by the index WOP for the model without paper and the index WP for the model with paper.
The calculation of the two copper percentage values can be found in the equations 4.8 and 4.9.

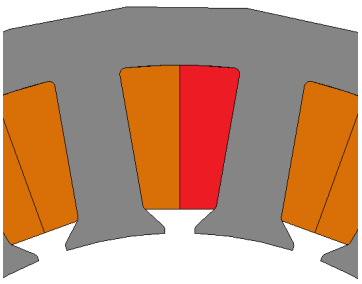

Figure 4.7 – Cross-sectional area of the slot for the copper percentage calculation (red)

$$A_{S,WOP} = 193.74\,\text{mm}^2$$
$$A_{S,WP} = 173.85\,\text{mm}^2$$

$$D_{W1} = 0.75\,\text{mm}$$
$$D_{W2} = 0.80\,\text{mm}$$

$$N_W = 45$$

$$A_{W1,2} = \pi \left(\frac{D_{W1,2}}{2} \right)^2$$

Name	Description
WP Nom	Nominal parameters (with paper)
WP Phi_10D	Copper percentage reduced by 10%
WP EP_50U	Young's modulus of paper increased by 50%
WP PhiP_50D	Paper percentage is reduced by 50%
WP xiE_50D	Adjustment factor ξ_E reduced by 50%
WP xiG_100U	Adjustment factor ξ_G increased by 100%
WP nuC_20U	Poisson's ratio of coating increased by 20%
WP nuP_50U	Poisson's ratio of paper increased by 50%
WP EC_15U	Young's modulus of coating increased by 15%
WP EC_20U	Young's modulus of coating increased by 20%

Table 4.14 – List of executed simulations (model with paper)

$$A_W = N_W \left(2 \cdot A_{W1} + 2 \cdot A_{W2}\right) \tag{4.7}$$

$$\phi_{Cu,WOP} = \frac{A_W}{A_{S,WOP}} = \frac{84.9997\,\text{mm}^2}{193.74\,\text{mm}^2} = 43.9\,\% \tag{4.8}$$

$$\phi_{Cu,WP} = \frac{A_W}{A_{S,WP}} = \frac{84.9997\,\text{mm}^2}{173.85\,\text{mm}^2} = 48.9\,\% \tag{4.9}$$

The data for the calculation simulation values for the windings can be found in table 4.15.

Quantity	Unit	Value
$\phi_{Cu,WOP}$	$\%$	43.9
$\phi_{Cu,WP}$	$\%$	48.9
ρ_w	$\frac{\text{kg}}{\text{m}^3}$	8920
ρ_i	$\frac{\text{kg}}{\text{m}^3}$	1680
E_w	GPa	115.0
E_i	GPa	2.8
ξ_E	-	2
ν_w	-	0.345
ν_i	-	0.4
G_w	GPa	42.8
G_i	GPa	1.0
ξ_G	-	1

Table 4.15 – Material parameters for the calculation of the nominal material parameters

The result of the simulation with nominal parameters (WOP) can be seen in figure 4.8.

The frequencies of the 0-type modes fit the measured frequencies quite well, the frequencies of 1-type modes are scattered over a wide range.

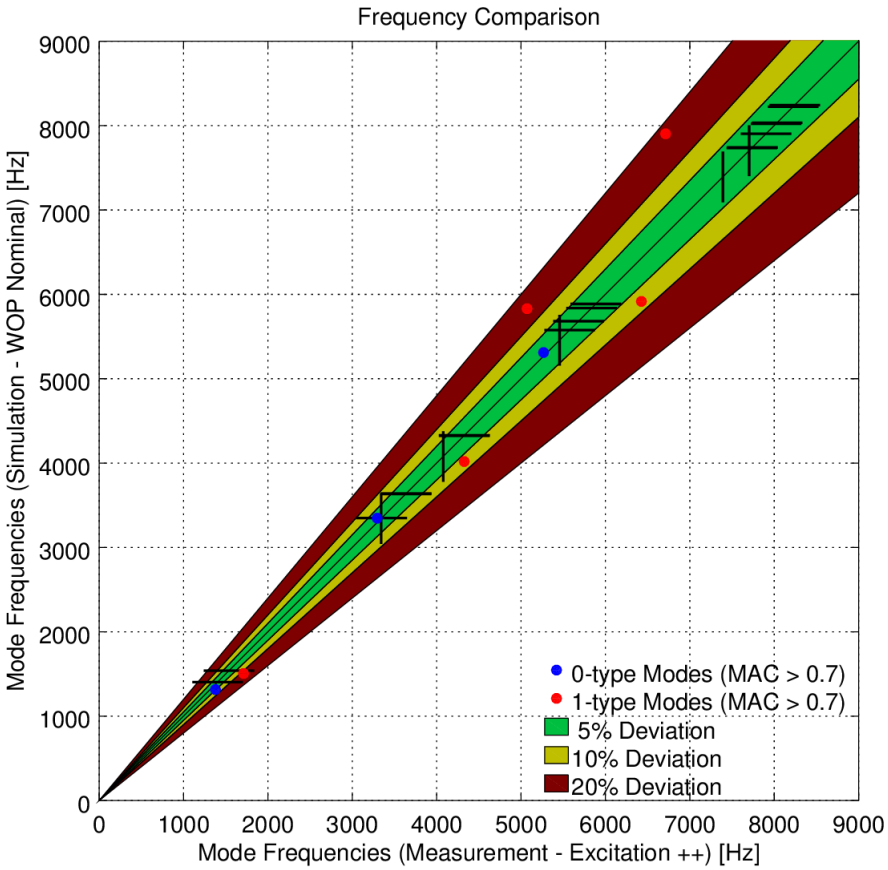

Figure 4.8 – Frequency comparison - nominal parameters

Variation of the mechanical properties of the coating As the actual mechanical properties of the coating could not directly be determined from the data sheet, the values for its Young's modulus and its Poisson's ratio are varied by 20% in both directions. Table 4.16 shows the values that are entered in Abaqus when performing the sensitivity analysis.

The influences of the variations are explained in the following.

The Young's modulus of the coating has a strong impact on all mode frequencies. A higher Young's modulus leads to a upward shift of mode frequencies, 0-type modes are influenced stronger than 1-type modes.
The frequency comparison resulting from the reduced Young's modulus can be seen in figure 4.9.

Quantity	Unit	Nom	$E_i - 20\%$	$E_i + 20\%$	$\nu_i - 20\%$	$\nu_i + 20\%$
ρ	$\frac{\text{kg}}{\text{m}^3}$	4856	4856	4856	4856	4856
E_θ	GPa	52.0	51.7	52.3	52.0	52.0
$E_z = E_r$	GPa	11.8	9.7	13.7	11.8	11.8
$\nu_{\theta r} = \nu_{\theta z}$	-	0.3640	0.3639	0.3641	0.3364	0.3917
ν_{rz}	-	0.1228	0.1151	0.1301	0.1024	0.1431
$G_{\theta r} = G_{\theta z}$	GPa	19.1	19.0	19.8	19.5	18.7
G_{rz}	GPa	2.4	2.0	2.9	2.6	2.3

Table 4.16 – Material parameters for the varied material parameters of the coating

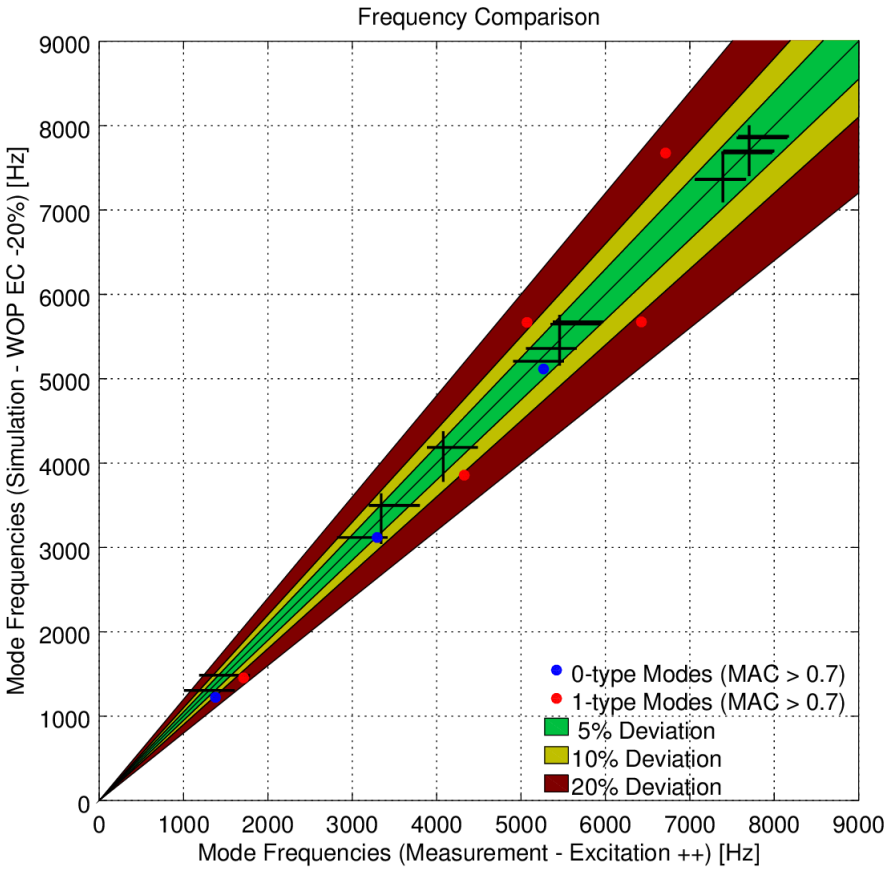

Figure 4.9 – Frequency comparison - reduced Young's modulus of coating

A change of the Poisson's ratio of the coating does not lead to large frequency shifts. It has only a slight influence on the mode frequencies of 0-type modes. Increasing the Poisson's ratio shifts those frequencies upwards nonuniformly.
The measurement-simulation comparison for the increased Poisson's ratio is displayed in figure 4.10.

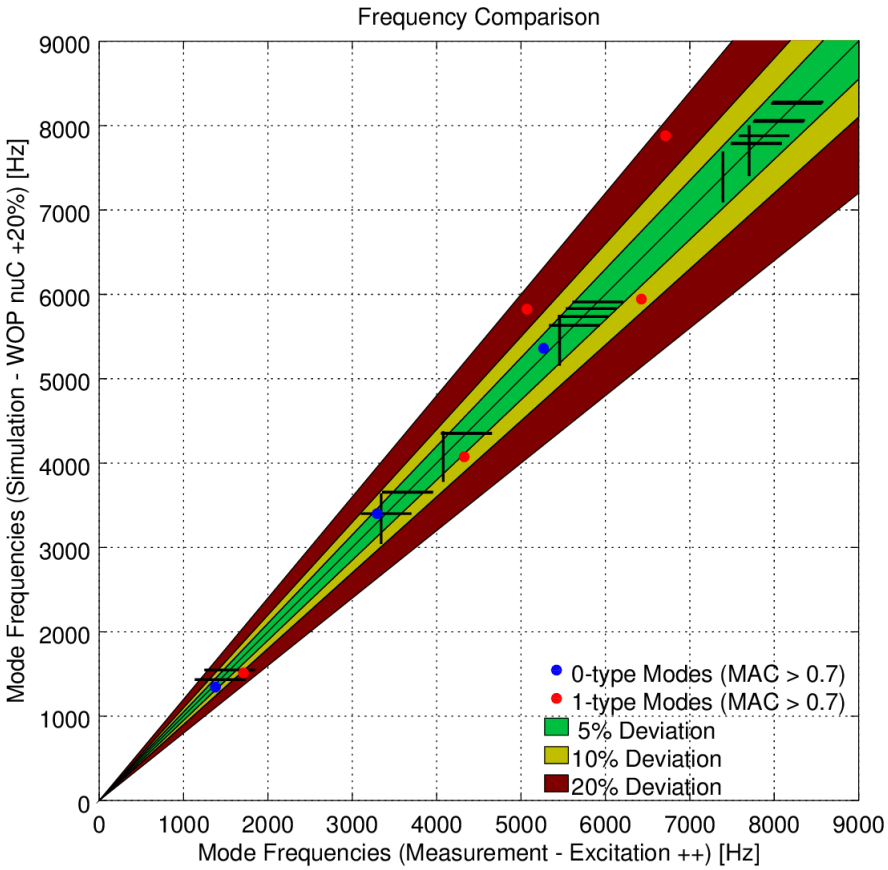

Figure 4.10 – Frequency comparison - increased Poisson's ratio of coating

Variation of the copper percentage in the windings The next variable that is varied is the copper percentage in the windings. Although this variable is determined by the known winding and slot areas, a hypothetical variation is executed to study its influence. The overall copper percentage is varied by $\pm 20\%$. Also the copper percentage of the end windings alone is varied by $\pm 10\%$ emulating a tighter or looser winding. Table 4.17 lists the simulation parameters.

The results for these variations are not shown in detail, but the influences of the varied parameters are explained.

Changing the copper percentage in the whole model has an impact on all mode frequencies - the effect is slightly stronger at 0-type modes. An increased copper percentage leads to higher mode frequencies.
When the copper percentage is changed only in the end winding section, effectively no influence can be seen on the mode frequencies.

Quantity	Unit	Nom	$\phi_{Cu} - 10\%$	$\phi_{Cu} + 10\%$	$\phi_{Cu} - 20\%$	$\phi_{Cu} + 20\%$
ρ	$\frac{\text{kg}}{\text{m}^3}$	4856	4539	5174	4221	5492
E_θ	GPa	52.0	47.1	57.0	42.2	61.9
$E_z = E_r$	GPa	11.8	10.3	13.5	8.9	15.5
$\nu_{\theta r} = \nu_{\theta z}$	-	0.3640	0.3659	0.3622	0.3680	0.3605
ν_{rz}	-	0.1228	0.1346	0.1129	0.1488	0.1048
$G_{\theta r} = G_{\theta z}$	GPa	19.0	17.2	20.9	15.4	22.7
G_{rz}	GPa	2.4	2.2	2.7	2.0	3.0

Table 4.17 – Material parameters for the varied copper percentage

Variation of adjustment factors ξ_E and ξ_G The next step is to investigate the influence of the adjustment parameters ξ_E and ξ_G. The material properties for these investigations are listed in table 4.18.

Quantity	Unit	Nom	$\xi_E - 50\%$	$\xi_G + 100\%$	$\xi_G - 100\%$
ρ	$\frac{\text{kg}}{\text{m}^3}$	4856	4856	4856	4856
E_θ	GPa	52.0	52.0	52.0	52.028
$E_z = E_r$	GPa	11.8	9.2	11.8	11.8
$\nu_{\theta r} = \nu_{\theta z}$	-	0.3648	0.3648	0.3640	0.3640
ν_{rz}	-	0.1228	0.1472	0.1228	0.1228
$G_{\theta r} = G_{\theta z}$	GPa	19.1	19.1	19.1	19.1
G_{rz}	GPa	2.4	2.4	31	18

Table 4.18 – Material parameters for the varied adjustment factors

Again, the results for these variations are not shown in detail, but the influences of the varied parameters are explained.

The changes in the adjustment factors did not lead to large changes in the mode frequencies. A reduction of the factors in each case shifts the mode frequencies of 0-type modes slightly down.

Optimization The results of the parameter studies are used to create an optimized parameter set. The used parameters for the winding and the coating section can be seen in table 4.19.
The optimization includes the reduction of the Young's modulus of the coating by 10% as well as an increase of the Poisson's ratio of the coating by 22.5%.
As the Young's modulus was only approximated using the Shore hardness and the Poisson's ratio was set to a typical value, a change in these parameters is plausible.

Quantity	Unit	Value
$\phi_{Cu,WOP}$	%	43.87
ρ_w	$\frac{kg}{m^3}$	8920
ρ_i	$\frac{kg}{m^3}$	1680 $\frac{kg}{m^3}$
E_w	MPa	115000
E_i	MPa	2526
ξ_E	-	2
ν_w	-	0.345
ν_i	-	0.49
G_w	MPa	42751
G_i	MPa	1002
ξ_G	-	1

Table 4.19 – Material parameters for the calculation of the optimized material parameters (WOP)

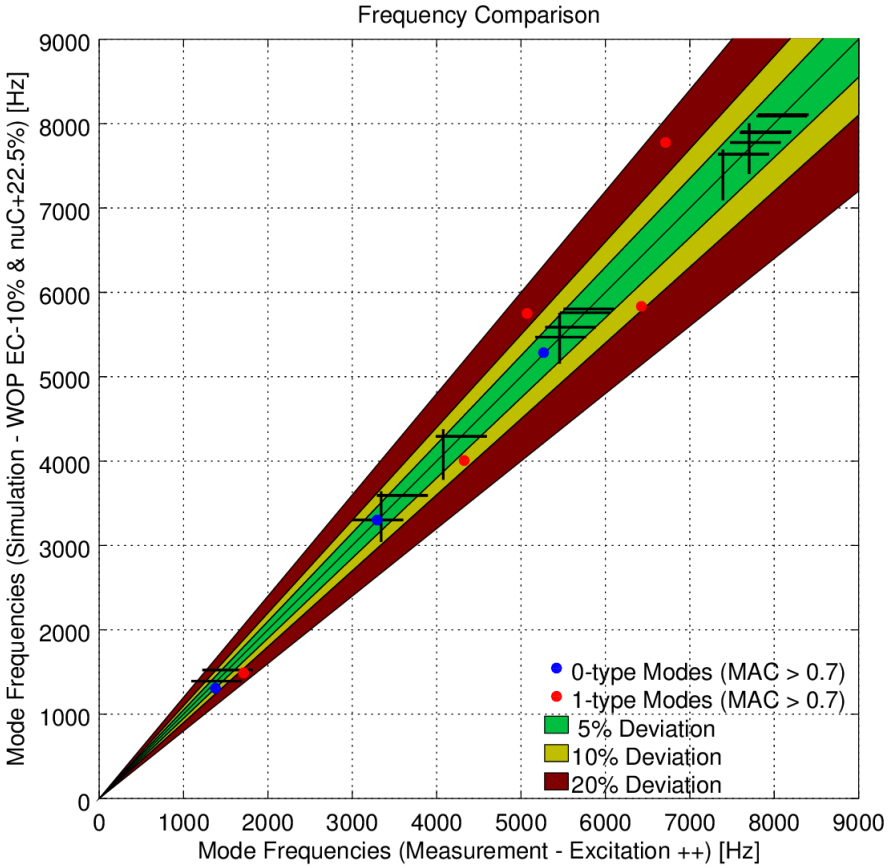

Figure 4.11 – Frequency comparison - optimized parameters

The results after optimization can be seen in figure 4.11. The mode frequencies of the 0-type modes match very well with the measurement, but this is not the case for the 1-type modes. Their frequencies are scattered within the $\pm 20\%$ range around the measurement results.
The deviations from the measurement are listed in detail in table 4.20. Deviations up to $\pm 5\%$ are marked green, deviations between $\pm 5\%$ and $\pm 10\%$ are yellow, larger deviations are marked red.
The deviations of 1-type modes lie between 7.39% and 15.85% which is not satisfying.

∅ Measurement [Hz]	Simulation [Hz]	Deviation [%]	Shape (-,-)
1378	1303	-5.19	(2,0)
1710	1489	-12.93	(2,1)
3293	3301	0.23	(3,0)
4326	4007	-7.37	(0,1)
5069	5750	13.44	(2,1)
5265	5285	0.38	(0,0)
6425	5834	-9.21	(4,1)
6714	7776	15.83	(3,1)

Table 4.20 – Comparison between the averaged measurement mode frequencies and the simulation mode frequencies

A model without consideration of the insulating paper does not suffice to describe the modal behavior of the stator.

Inclusion of the insulating paper After having determined that sufficient modeling requires the consideration of the insulating paper, a second stator model is built. This model includes a section of 0.5 mm thickness d_{PS} between the iron core and the windings. [18] concluded that the insulating paper influences the overall tangential stiffness of the model.

Nominal parameters The nominal parameters are the same as for the model without paper apart from the changed copper percentage.

The properties for the paper section are determined as explained in the following.
The actual paper thickness d_P is not known, it lies approximately in the range from 0.2 mm to 0.3 mm.

This means that the paper section in the model does not consist of paper only, but a part of it is filled with coating material. This can be seen in figure 4.12.

Figure 4.12 – Cut stator

Homogenized isotropical material parameters are applied to the paper section (PS). These parameters are calculated using a weighted mean from the properties of paper and coating approximating the assumed paper thickness. For the nominal simulation run the relation between paper and coating is set to $2:1$. The resulting material properties are calculated using the equations 4.12 to 4.14.

$$\phi_C = \frac{1}{3} \tag{4.10}$$

$$\phi_P = \frac{2}{3} \tag{4.11}$$

$$E_{PS} = \phi_P \cdot E_P + \phi_C \cdot E_C \tag{4.12}$$

$$\nu_{PS} = \phi_P \cdot \nu_P + \phi_C \cdot \nu_C \tag{4.13}$$

$$G_{PS} = \frac{E_{PS}}{2(1+\nu_{PS})} \tag{4.14}$$

The results of the simulation including the insulation paper can be seen in figure 4.13. Compared to the simulation without paper, all mode frequencies are shifted downward non-uniformly. No systematic difference between 0-type modes and 1-type modes can be seen. The consideration of the insulation paper leads to reduced overall stiffness of the model as the Young's modulus of paper is much lower than the Young's moduli of the other obstructed materials. This reduction of stiffness explains the downward shift of mode frequencies.

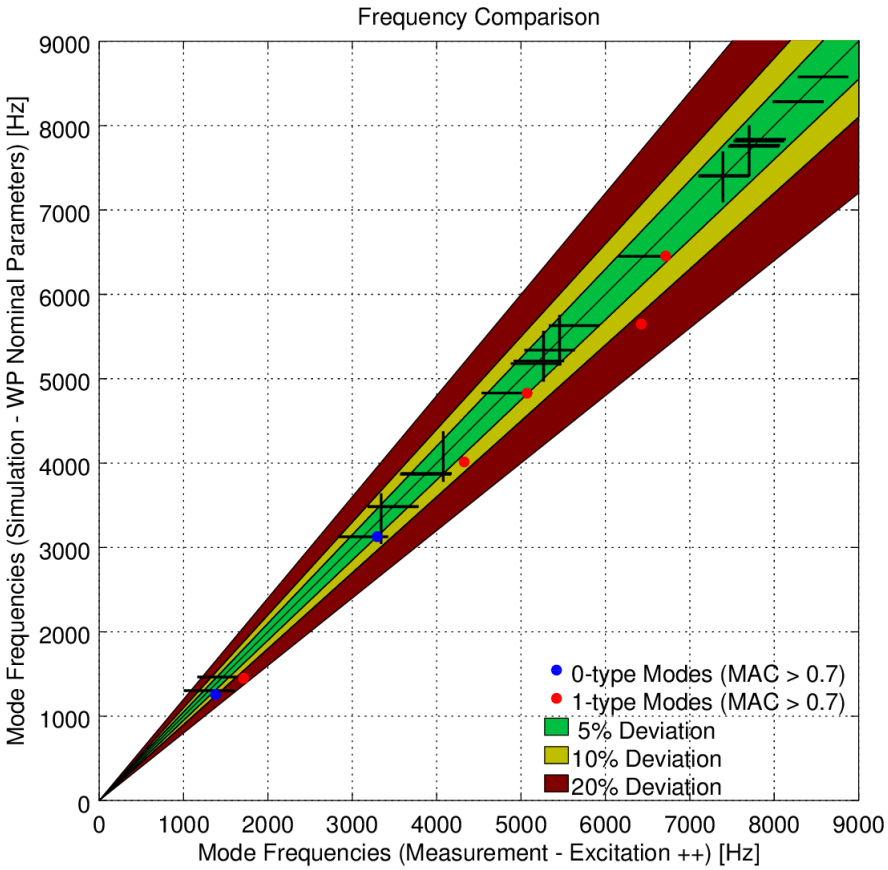

Figure 4.13 – Frequency comparison - nominal parameters (corrected copper percentage)

Variation of the copper percentage in the windings In this parameter study the influence of a hypothetically changed copper percentage is examined. The copper percentage is reduced by 10% which corresponds to the copper percentage used in the model without paper.
The comparison of the resulting mode frequencies to the measurement is displayed in 4.14.
The reduction of the copper percentage leads to a reduction of mode frequencies. When reducing the copper percentage the winding-insulation mixture is determined more by the properties of the coating which is less stiff than copper.

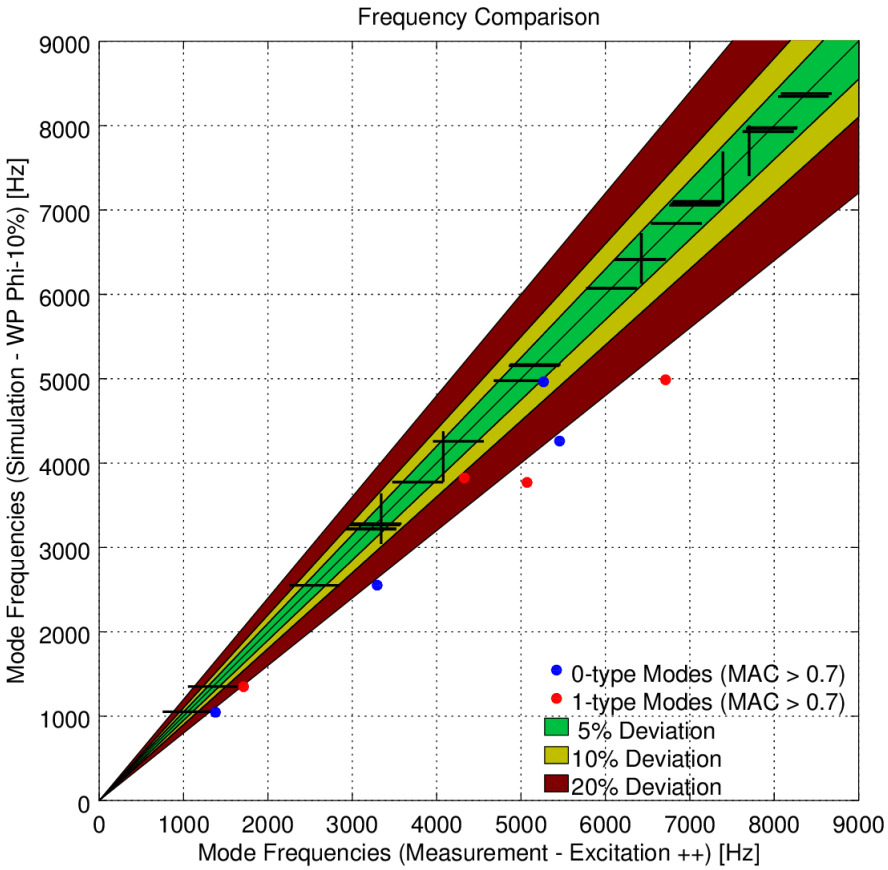

Figure 4.14 – Frequency comparison - reduced copper percentage

Variation of the paper-winding relation in the paper section The relation of paper to winding in the paper section is reversed and set from $2:1$ to $1:2$, which means a reduction of paper material by half. The resulting properties for the paper section can be seen in table 4.21.
The change in the relation towards the coating leads to increased values for Young's modulus, Poisson's ratio and shear modulus.

Quantity	Unit	Nom	$\phi_P - 50\%$
ρ_{PS}	$\frac{\text{kg}}{\text{m}^3}$	1240	1460
E_{PS}	MPa	1002	1905
ν_{PS}	-	0.333333	0.366667
G_{PS}	MPa	376	697

Table 4.21 – Material parameters for the varied paper percentage

When looking at the simulation result in figure 4.15 it can be seen, that the mode frequencies are shifted upwards compared to the nominal situation.
The frequencies of the 0-type modes match the measured frequencies quite well, the frequencies of the 1-type modes show more deviation towards lower and higher frequencies.

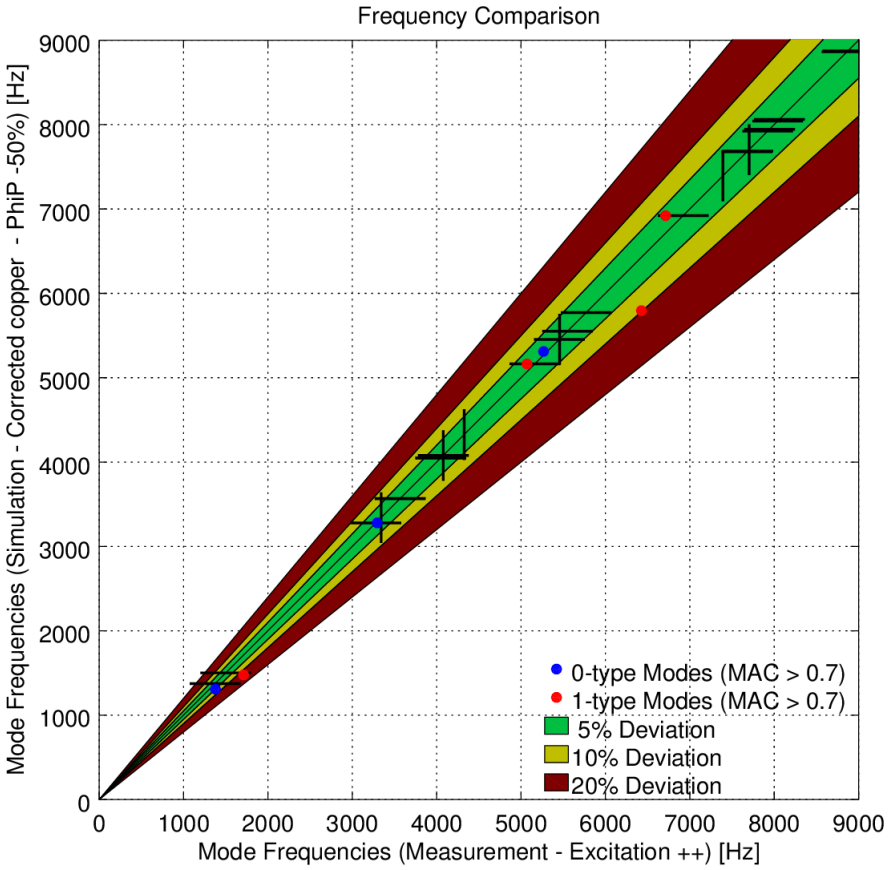

Figure 4.15 – Frequency comparison - reduced paper percentage

Variation of the paper properties The Young's modulus and the Poisson's ratio of the insulating paper are increased by 50% each. The resulting material properties can be seen in table 4.22.

Quantity	Unit	Nom	$E_P + 50\%$	$\nu_P + 50\%$
ρ_{PS}	$\frac{\text{kg}}{\text{m}^3}$	1240	1240	1240
E_{PS}	MPa	1002	1036	1002
ν_{PS}	-	0.333333	0.333333	0.433333
G_{PS}	MPa	376	388	350

Table 4.22 – Material parameters for the varied paper properties

The influences of the changed paper parameters are very little, therefore no results are displayed. An increase of the Young's modulus leads to a slight upward shift of all mode frequencies, there is no dependency of the shift on the mode type. The same applies to an increase of the Poisson's ratio.

Variation of adjustment factors The adjustment factors are varied in the same manner as for the model without paper. The resulting material properties for the windings are listed in table 4.23.

Quantity	Unit	Nom	$\xi_E - 50\%$	$\xi_G + 100\%$
ρ	$\frac{\text{kg}}{\text{m}^3}$	5220	5220	5220
E_θ	GPa	57.7	57.7	57.7
$E_z = E_r$	GPa	13.8	10.6	13.8
$\nu_{\theta r} = \nu_{\theta z}$	-	0.3619	0.3619	0.3619
ν_{rz}	-	0.1116	0.1331	0.1116
$G_{\theta r} = G_{\theta z}$	GPa	21.2	21.2	21.2
G_{rz}	GPa	2.8	2.8	3.5

Table 4.23 – Material parameters for the varied adjustment factors

The results of these simulations are not shown in detail because these variations did not lead to significant changes in the mode frequencies. The impact of the changes of the adjustment factors is very small, but 0-type modes are influenced more than 1-type modes. An increase of the factors leads to an upward shift and vice versa.

Variation of the coating properties The properties of the coating are varied according to table 4.24. A change of the coating properties influences the resulting properties in the winding and paper section.

Quantity	Unit	Nom	$\nu_C + 50\%$	$E_C + 15\%$	$E_C + 20\%$
ρ	$\frac{\text{kg}}{\text{m}^3}$	5220	5220	5220	5220
E_θ	GPa	57.7	57.7	57.9	57.9
$E_z = E_r$	GPa	13.8	13.8	15.4	16.0
$\nu_{\theta r} = \nu_{\theta z}$	-	0.3619	0.3866	0.3620	0.3620
ν_{rz}	-	0.1116	0.1291	0.1174	0.1193
$G_{\theta r} = G_{\theta z}$	GPa	21.2	20.8	21.2	21.3
G_{rz}	GPa	2.8	2.6	3.1	3.3
ρ_{PS}	$\frac{\text{kg}}{\text{m}^3}$	1240	1240	1240	1240
E_{PS}	MPa	1002	1002	1143	1189
ν_{PS}	-	0.3333	0.36	0.3333	0.3333
G_{PS}	MPa	376	368	428	446

Table 4.24 – Material parameters for the varied coating properties

Changing the Poisson's ratio does not lead to considerable changes in the mode frequencies. The increase of the Poisson's ratio provokes a little non-uniform upward shift of mode frequencies, the shift is slightly stronger for 0-type modes.

The increase of the Young's modulus has a considerable impact on the mode frequencies. Compared to the nominal simulation the frequencies are shifted upward non-uniformly. The shift happens in a very similar manner as for the change in the paper/coating relation. Both parameter studies include an increased stiffness in the paper section. The result for the Young's modulus increased by 20% can be seen in figure 4.16.
It has to be noted that in this frequency comparison the criterion for matching modes of $MAC > 0.7$ was changed to $MAC > 0.69$ in order to include the mode at 6714 Hz in the comparison.

In the first step the Young's modulus has only been increased by 15% but in order to match the simulation result to the measurement, the higher increase is calculated. For an increase of 15% the general frequency level is a little lower than for 20%, the qualitative result is very similar though.

The simulation with the 20% yields the best result regarding mode frequencies from all executed parameter studies. This might be an over-adaptation, as the modeling of the pure lamination stack yielded mode frequencies that were slightly overestimated.
The 0-type modes match well between measurement and simulation. The majority of the 1-type modes lie within the range of $\pm 5\%$ deviation apart from two modes with higher deviations.

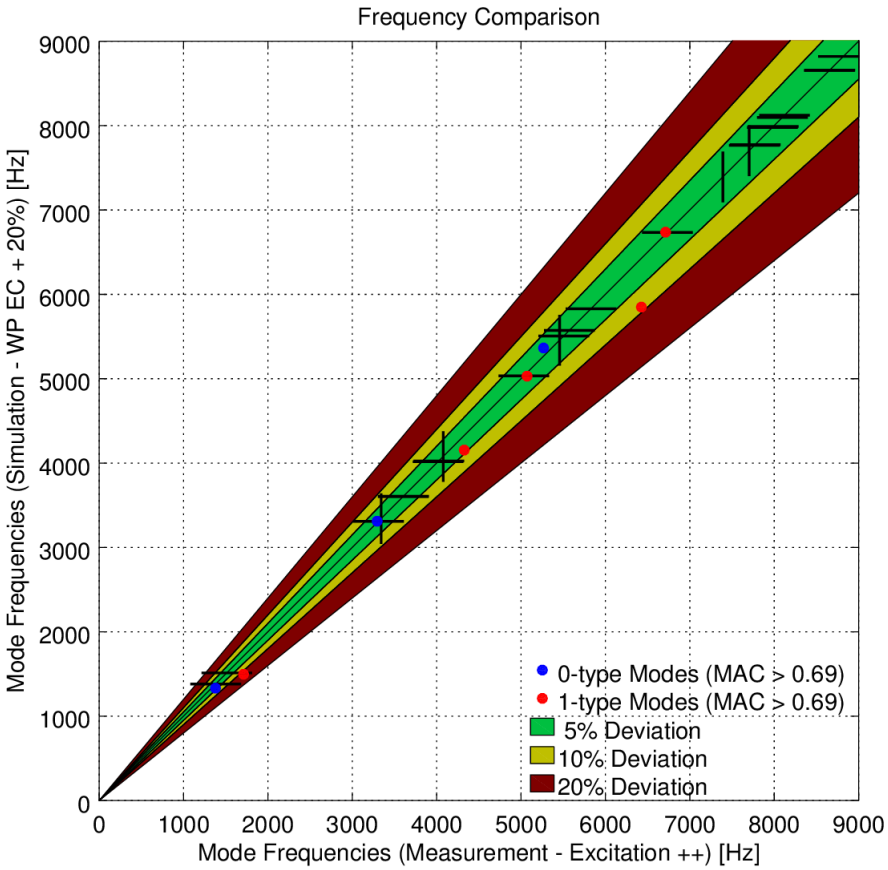

Figure 4.16 – Frequency comparison - optimized parameters (WP)

The deviations from the averaged measured frequencies are listed in table 4.25.

∅ Measurement [Hz]	Simulation [Hz]	Deviation [%]	Shape (-,-)
1378	1332	-3.34	(2,0)
1710	1497	-12.50	(2,1)
3293	3311	0.55	(3,0)
4326	4154	-3.97	(0,1)
5069	5030	-0.76	(2,1)
5265	5364	1.88	(0,0)
6425	5849	-8.97	(4,1)
6714	6737	0.35	(3,1)

Table 4.25 – Comparison between the averaged measurement mode frequencies and the simulation mode frequencies

The coloring denotes the range of deviation used in the visual frequency comparison from figure 4.16.
One of the 1-type outliers lies in the range of $\pm 10\%$ deviation, the other outlier dwells in the range of $\pm 20\%$ deviation.

4.3.4 Complex-valued Eigenvalue Extraction

For the complex eigenvalue analysis the material is assigned a damping value.
Equations 4.15 and 4.16 show the damping parameters corresponding to the measurement α_{Stator} and γ_{Stator}.

$$\alpha_{Stator} = 211.37 \, \frac{1}{\mathrm{s}} \tag{4.15}$$

$$\gamma_{Stator} = 7.1411 \times 10^{-7} \, \mathrm{s} \tag{4.16}$$

For the simulation the material damping of the stator core is taken from the simulation of the lamination stack, the values can be found in equations 4.4 and 4.5.
The remaining components are assigned another set of Rayleigh damping coefficients determined from a parameter study. As there are no clues as to how much the different components contribute to the damping, the same damping values are applied to windings, coating, and paper. These values $\alpha_{W,C,P}$ and $\gamma_{W,C,P}$ can be seen in the equations 4.17 and 4.18.

$$\alpha_{W,C,P} = 0 \, \frac{1}{\mathrm{s}} \tag{4.17}$$

$$\gamma_{W,C,P} = 4.9988 \times 10^{-7} \, \mathrm{s} \tag{4.18}$$

In the determination process it could be seen that a low level of damping compared to the lamination stack leads to a significant increase in the modal damping result. Therefore, it can be concluded that the added components are strongly effective regarding the modal damping.
The effect of the mass proportional damping α is negligible, the inner damping γ is the prominent factor.

Figure 4.17 shows the resulting modal damping from the simulation. As there are different damping values applied to different components, the modal damping deviates from the curve fit - as opposed to the behavior of the simulation of the lamination stack. In the figure, lines denote matching modes. In the measurement there are a few outliers in the damping that can not be reproduced by the simulation.
Possible explanations for the deviation may be, that the direction dependent damping of the lamination stack can not be considered and that the windings, coating and paper do not have all the same damping values in reality. Therefore, some effects cannot be considered.

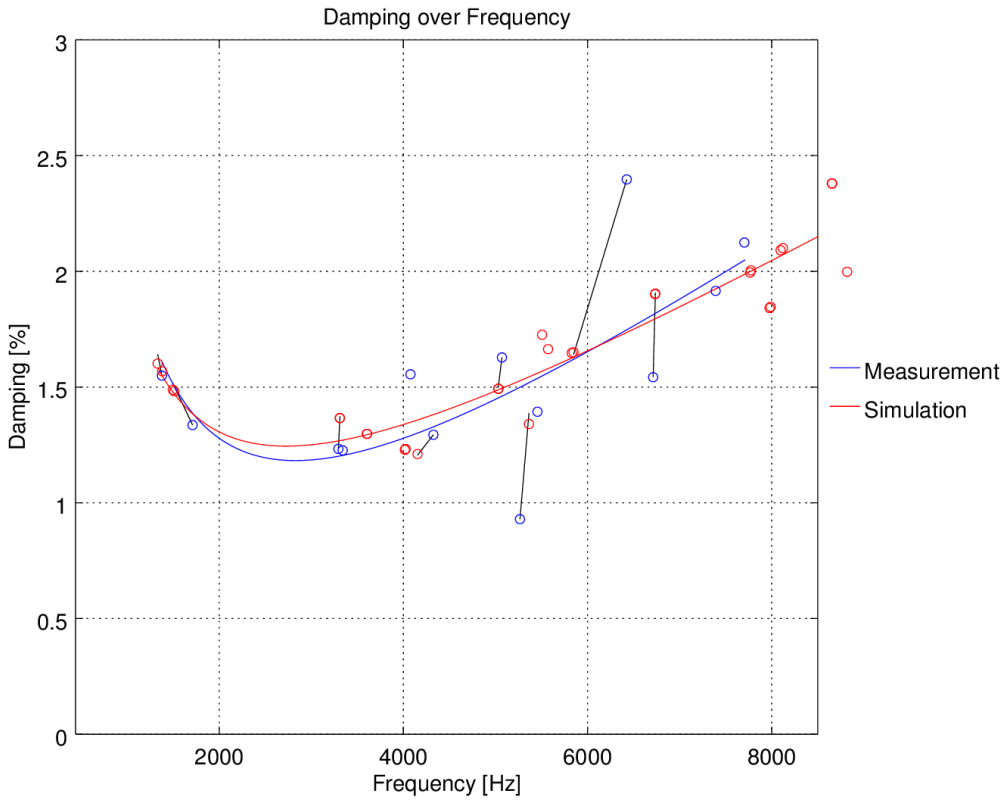

Figure 4.17 – Comparison of measured and simulated damping

4.3.5 Forced Response Analysis

The frequency response functions are calculated by applying a force of 1 N to the node that lies closest to the position where the hammer excitation happened in the experimental modal analysis.
The damping is defined using the Rayleigh coefficients from the measurement (equations 4.15 and 4.16).
The FRFs are displayed in the four sensor positions that were used for the measurement-measurement comparison (figure 4.18), the comparison is done in terms of velocity.
The measurement range consists of the data from the measurement runs with medium and high excitation, the low excitation was excluded because of bad measurement quality.
In the comparison it can be seen that the most prominent peaks exist in the measured as well as in the simulated FRFs. The deviations in mode frequencies for two of the modes that has already been evident in the frequency comparison is visible in the FRFs. The overall course of the simulated FRF resembles the measurement, yet some effects have not been considered.

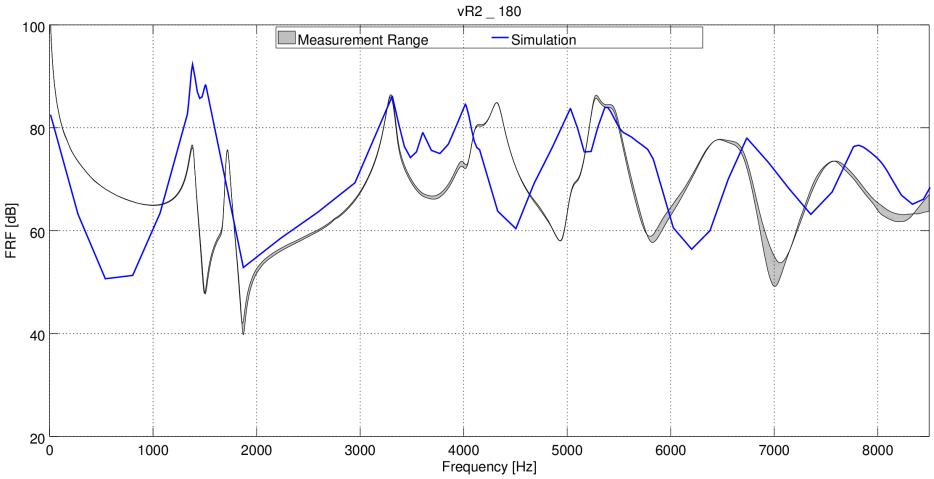

(a) FRFs at sensor vR2_180

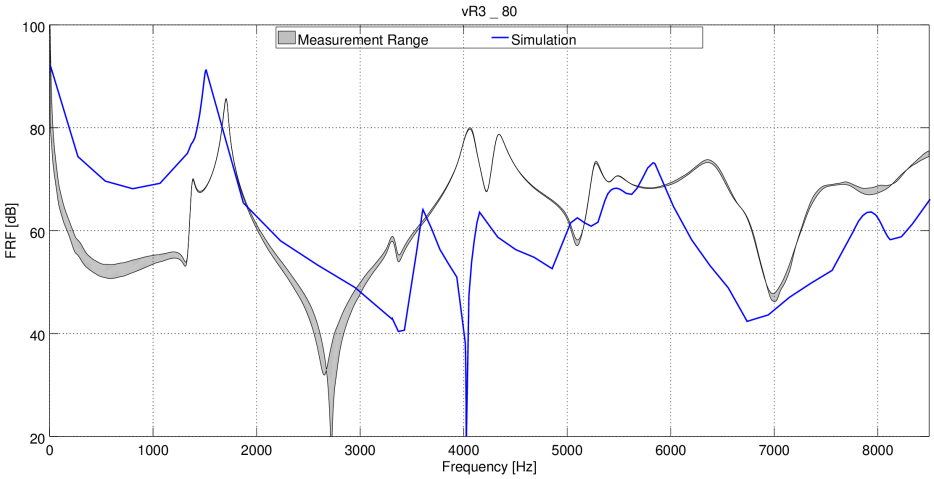

(b) FRFs at sensor vR3_180

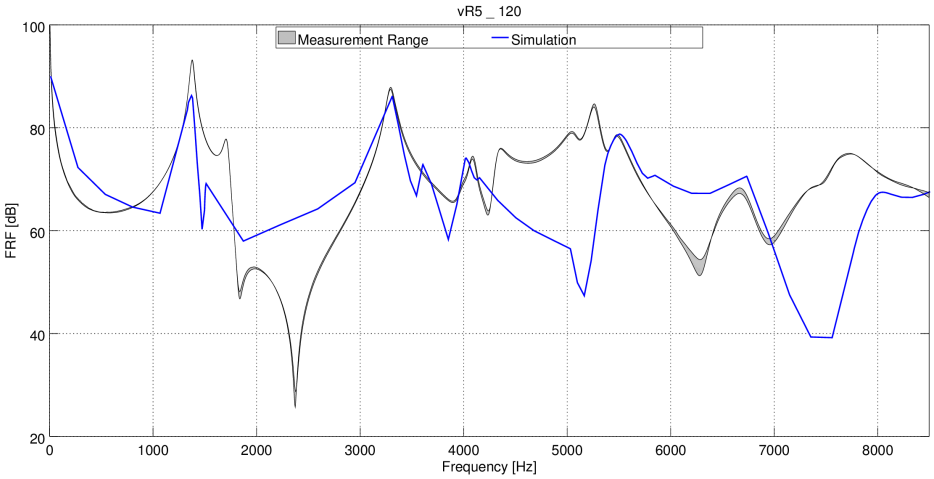

(c) FRFs at sensor vR5_120

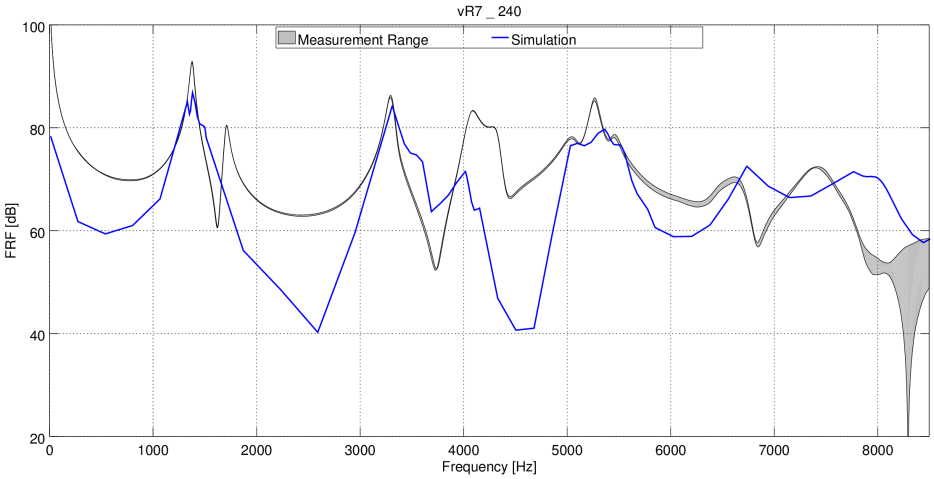

(d) FRFs at sensor vR7_240

Figure 4.18 – FRF comparison measurement/simulation at four different sensor positions

4.3.6 Summary of the Results

The consideration of the insulating paper is crucial for the correct modeling of the stator. The properties of the paper section (determined by paper and coating material) are of utmost importance for a good result. With a good approximation of the properties, the eigenfrequencies can be estimated well in most cases.
For a better description of modal damping, an exploration of the damping properties of the different components (windings, coating, paper) should be engaged.

4.4 Stator (HM132)

It is of interest whether the results and findings from the stator of the range extender can be applied to a different stator of a bigger electric machine.

4.4.1 Model

The stator model has different sections for the laminated sheets, the insulating paper, the winding within the slot, and the end winding. The mesh of this model is coarser than of the other models. It consists of 298329 nodes and 263136 linear hexahedral nodes.

4.4.2 Material Modeling

Material parameters of components. For the laminated sheets, the properties determined in the optimization process in section 4.2.3 are used, but the Young's modulus of the electrical steel is slightly altered, as the material is not exactly the same as before. The properties of the steel sheets from the data sheet can be found in table 4.26

Material	M330-35A
Sheet thickness	0.35 mm $\pm$ 8%
Density	7650 $\frac{\text{kg}}{\text{m}^3}$
Young's modulus	$200 - 220$ GPa
Poisson's ratio	0.3

Table 4.26 – Material parameters electric sheets

The properties of the paper are the same as for the stator of the range extender (table 4.12).
The windings are again modeled as a homogenized material made from copper (see table 4.11) and an insulation material. The specific insulation material is not known, therefore the parameters from the optimization process of the range extender stator (WOP) were used for the investigation (table 4.27).

Material	Insulation material
Density	1680 $\frac{\text{kg}}{\text{m}^3}$
Young's modulus	2526 MPa
Poisson's ratio	0.49

Table 4.27 – Material parameters insulation material

The winding inside the slots is modeled transverse isotropically, whereas the end windings are modeled isotropically. The end windings of this stator are interlaced in a way, that no distinct orientation can be determined - therefore the isotropic modeling is chosen. For that, the Young's modulus 4.19 and Poisson's ratio 4.20 are averaged between the values in axial and perpendicular direction.

If one wanted to calculate the Young's modulus using the equations 2.26 and 2.27, one has to set the adjustment factor ξ_E to 20.03 to achieve the same result. This increase of this equivalent adjustment factor corresponds to a shift towards a serial connection compared to the winding stiffness in the plane perpendicular to the wire direction inside the slots.

$$E_{EW} = \frac{E_\theta + E_r}{2} \tag{4.19}$$

$$\nu_{EW} = \frac{\nu_{\theta z} + \nu_{rz}}{2} \tag{4.20}$$

4.4.3 Real-valued Eigenvalue Extraction

Performed Variations of Material Parameters A set of parameter variations is executed. The variations are listed in table 4.28.
The relevant variations are explained in the following.

Name	Description
Nom	Nominal parameters
Phi20D	Copper percentage reduced by 20%
Phi20U	Copper percentage increased by 20%
E_C20D	Young's modulus of coating reduced by 20%
E_C20U	Young's modulus of coating increased by 20%
EW_E20D	Young's modulus in end windings reduced by 20%
EW_E20U	Young's modulus in end windings increased by 20%
EW_nu20D	Poisson's ratio in end windings reduced by 20%
EW_nu20U	Poisson's ratio in end windings increased by 20%

Table 4.28 – List of executed simulation

Nominal Parameters. The laminated sheets are modeled as before - the properties of the varnish and the steel percentage are taken from the optimized result of the simulation of the lamination stack. The properties of the steel sheets are slightly altered as a different sheet material has been used. The parameters used for the calculation of the homogenized material can be seen in table 4.29.

The windings are modeled as for the stator of the range extender. The material parameters are listed in table 4.30.

The insulation paper is modeled in the same way as for the stator of the range extender, the parameters can be seen table 4.31. As there is a double layer of insulation paper no mixture with the coating material is calculated, but the pure paper properties are applied to whole paper section.

Quantity	Unit	Value
ϕ_{St}	%	97.71
ρ_f	$\frac{\text{kg}}{\text{m}^3}$	7650
ρ_m	$\frac{\text{kg}}{\text{m}^3}$	1100
E_f	MPa	210000
E_m	MPa	687
ν_f	-	0.3
ν_m	-	0.4
G_f	MPa	8077
G_m	MPa	245

Table 4.29 – Material parameters for the calculation of the nominal material parameters - laminated sheets

Quantity	Unit	Value
ϕ_{Cu}	%	43.87
ρ_w	$\frac{\text{kg}}{\text{m}^3}$	8920
ρ_i	$\frac{\text{kg}}{\text{m}^3}$	1680
E_w	MPa	115000
E_i	MPa	2526
ξ_E	-	2
ν_w	-	0.345
ν_i	-	0.49
G_w	MPa	42751
G_i	MPa	848
ξ_G	-	1

Table 4.30 – Material parameters for the calculation of the nominal material parameters - windings

Quantity	Unit	Value
ρ_P	$\frac{\text{kg}}{\text{m}^3}$	1020
E_P	MPa	100
ν_P	-	0.3
G_P	MPa	38.5

Table 4.31 – Material parameters for the calculation of the nominal material parameters - paper

The simulation-measurement comparison is done using the MAC in the first step. The results can be seen in figure 4.19.

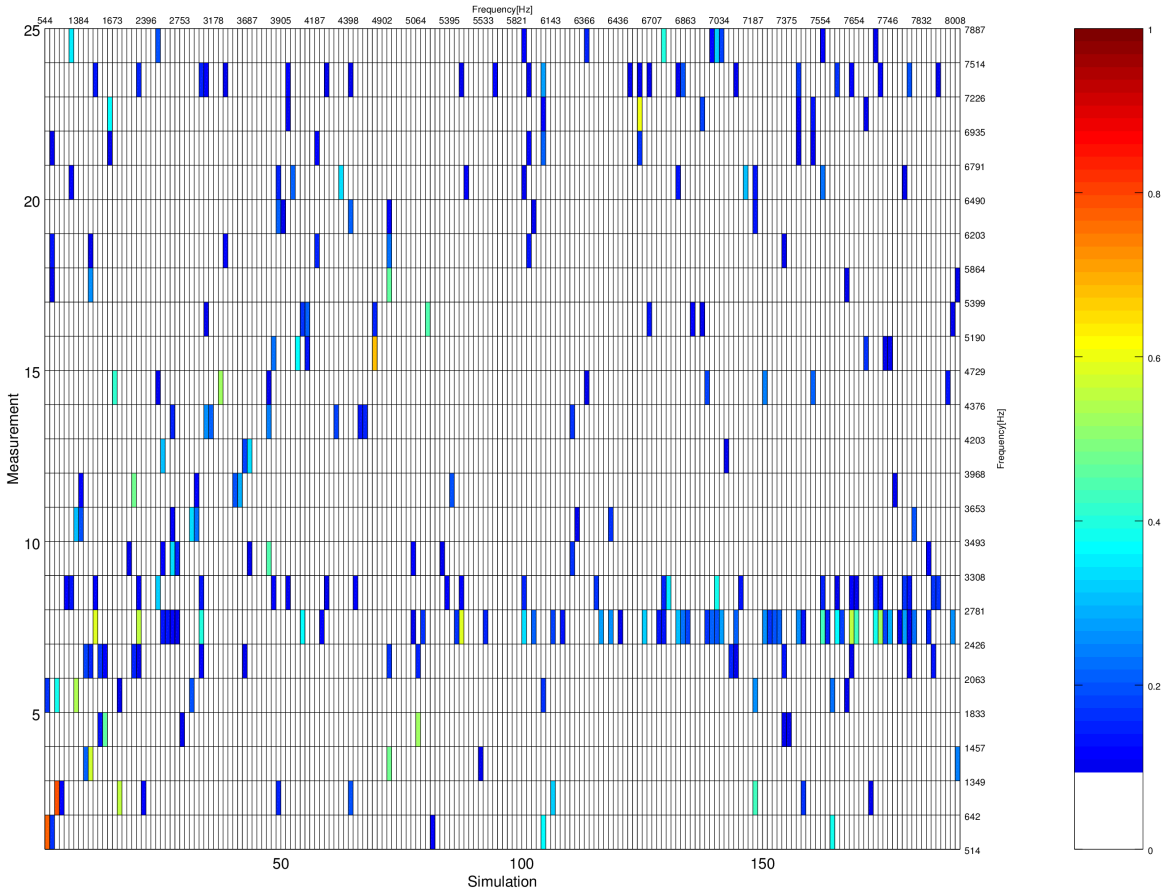

Figure 4.19 – MAC comparison between measurement and simulation - nominal parameters

For the other components a limit of 0.7 has been set to determine the matching modes. When applying this on the results for this stator, only two modes are considered matching. Because two modes are a weak basis for a comparison, some additional modes are chosen for comparison. The conditions for the further modes for comparison are that there is only one distinct maximum in the respective MAC row and that the mode appears in the measurement-measurement comparison.

A closer look on the areas in which the chosen modes lie in the MAC can be taken in figure 4.20.

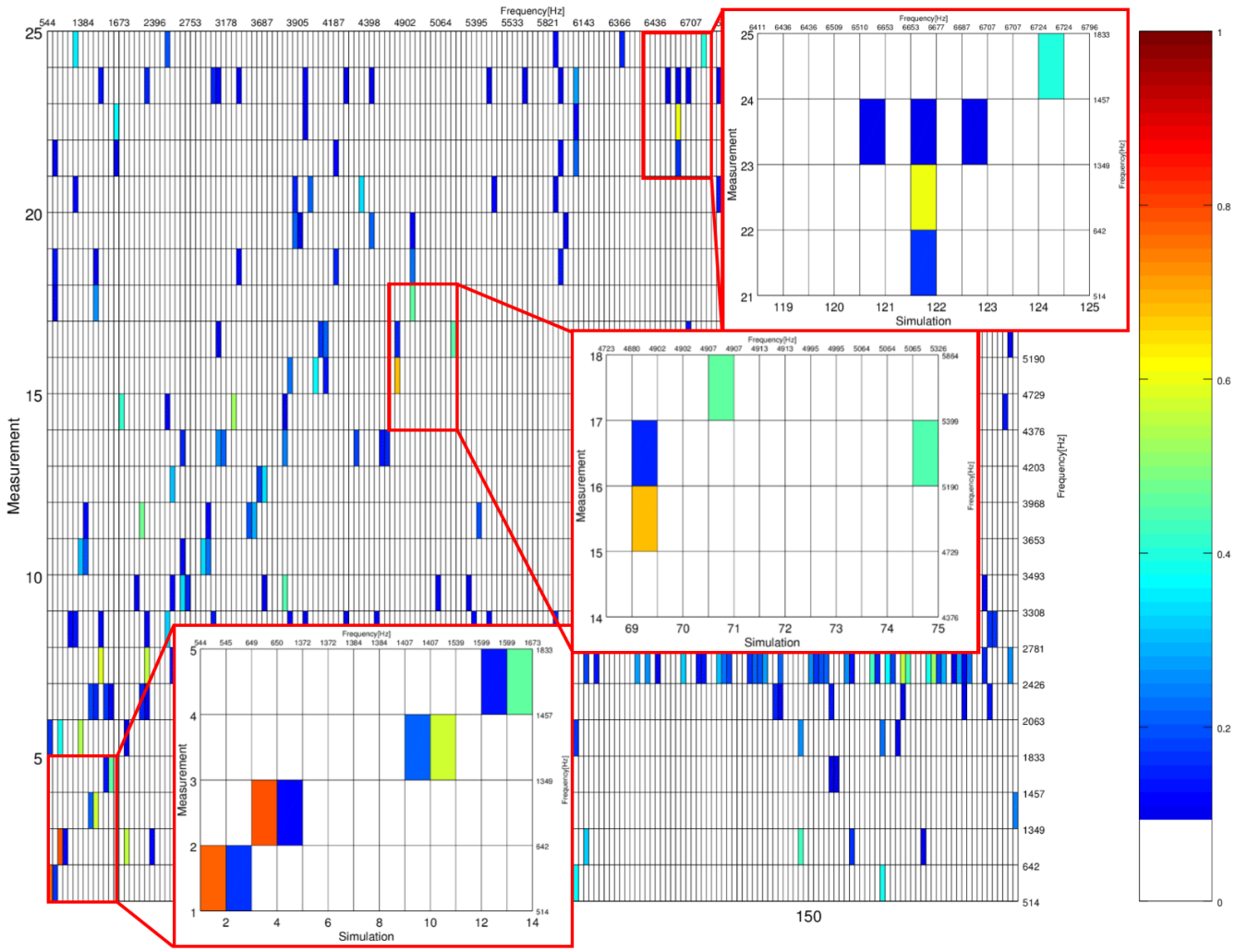

Figure 4.20 – MAC comparison between measurement and simulation - nominal parameters - zoomed on relevant areas

The chosen modes are divided into two groups:

Good Matches:

$MAC > 0.59$ and the conditions mentioned above are met

The good matches can be seen in table 4.32.

∅ Measurement [Hz]	Simulation [Hz]	MAC [–]	Deviation [%]	Shape (-,-)
514	544	0.775	5.91	(2,0)
642	649	0.798	1.11	(2,1)
4729	4880	0.681	3.20	(0,1)
6935	6653	0.596	-4.06	(1,X)

Table 4.32 – Good matches (nominal)

Tolerable Matches:
$MAC > 0.44$, and the conditions mentioned above are met
The tolerable matches can be seen in table 4.33.

∅ Measurement [Hz]	Simulation [Hz]	MAC [−]	Deviation [%]	Shape (-,-)
1349	1407	0.573	4.28	(3,0)
1457	1599	0.530	9.75	(3,1)
5190	5065	0.449	-2.41	(0,4)
5399	4907	0.466	-9.11	(6,X)

Table 4.33 – Tolerable matches (nominal)

These chosen modes are used in the subsequent material studies to conduct the comparison.

Variation of the copper percentage The copper percentage in the windings is varied in both directions by 20%. The resulting homogenized winding properties can be seen in table 4.34.

Quantity	Unit	Nom	$\phi_{Cu} - 20\%$	$\phi_{Cu} + 20\%$
ρ	$\frac{kg}{m^3}$	4856	4221	5492
E_θ	GPa	51.9	42.0	61.7
$E_z = E_r$	GPa	10.5	8.1	14.2
E_{EW}	GPa	31.3	25.1	38.0
$\nu_{\theta r} = \nu_{\theta z}$	-	0.3950	0.4054	0.3857
ν_{rz}	-	0.1414	0.1747	0.1179
ν_{EW}	-	0.2682	0.2900	0.2518
$G_{\theta r} = G_{\theta z}$	GPa	18.6	14.9	22.3
G_{rz}	GPa	2.1	1.7	2.6

Table 4.34 – Material parameters for the varied copper percentage

The effect of the property changes on the mode frequencies can be seen in table 4.35. The eigenfrequencies from the two simulations are listed along with their deviations from the averaged measured frequency. Deviations within the range of $\pm 5\%$ are marked green, deviations within $\pm 10\%$ are marked yellow, larger deviations are marked red.
Changing the copper percentage does lead to frequency shifts, but no pattern can be seen. Some modes are shifted upwards, some downwards - independent from the respective mode type.
The largest frequency shift compared to the nominal simulation can be seen for the (2,1) mode at 642 Hz. For an increased copper percentage this mode frequency is increased by 2.2% in comparison to the nominal parameters.

∅ Measurement [Hz]	Simulation $\phi_{Cu} - 20\%$ [Hz]	Deviation $\phi_{Cu} - 20\%$ [%]	Simulation $\phi_{Cu} + 20\%$ [Hz]	Deviation $\phi_{Cu} + 20\%$ [%]
514	541	5.27	548	6.54
642	634	-1.20	663	3.32
4729	4933	4.31	4828	2.09
6935	6733	-2.92	6569	-5.27
1349	1411	4.59	1402	3.91
1457	1579	8.35	1617	11.01
5190	5081	-2.10	5051	-2.69
5399	4963	-8.08	4850	-10.16

Table 4.35 – Frequency comparison - variation of the copper percentage

The overall deviations to the measured frequencies are smaller than in the nominal case for the reduced copper percentage, for the increased copper percentage the opposite is the case.

Variation of the coating properties The Young's modulus of the coating is varied in both directions by 20%. The resulting homogenized winding properties can be seen in table 4.36.

Quantity	Unit	Nom	$E_C - 20\%$	$E_C + 20\%$
ρ	$\frac{kg}{m^3}$	4856	4856	4856
E_θ	GPa	51.9	51.6	52.2
$E_z = E_r$	GPa	10.7	8.8	1.26
E_{EW}	GPa	31.3	30.2	32.4
$\nu_{\theta r} = \nu_{\theta z}$	-	0.3950	0.3948	0.3952
ν_{rz}	-	0.1414	0.1337	0.1489
ν_{EW}	-	0.2682	0.2643	0.2721
$G_{\theta r} = G_{\theta z}$	GPa	18.6	18.5	18.7
G_{rz}	GPa	2.1	1.7	2.5

Table 4.36 – Material parameters for the varied coating properties

Changing the Young's modulus of the coating does not have a large influence on the mode frequencies compared to nominal. The deviations of the simulated mode frequencies from the measurement can be seen in table 4.37.
The only noticeable change happened for the (2,1) mode which shifted slightly upwards for an increased Young's modulus and vice versa.

∅ Measurement [Hz]	Simulation $E_C - 20\%$ [Hz]	Deviation $E_C - 20\%$ [%]	Simulation $E_C + 20\%$ [Hz]	Deviation $E_C + 20\%$ [%]
514	545	6.06	547	6.39
642	647	0.73	655	1.97
4729	4913	3.90	4884	3.28
6935	6703	-3.35	6659	-3.98
1349	1412	4.70	1410	4.53
1457	1599	9.75	1608	10.37
5190	5088	-1.97	5075	-2.22
5399	4938	-8.55	4915	-8.96

Table 4.37 – Frequency comparison - variation of the copper percentage

Compared to nominal the overall deviation is slightly improved for the reduced Young's modulus, for the increased Young's modulus the deviations are larger.

Variation of the end winding properties The Young's modulus and the Poisson's ratio of the end windings is varied in both directions by 20%. The resulting homogenized winding properties can be seen in table 4.36.

Quantity	Unit	Nom	$E_{EW} - 20\%$	$E_{EW} + 20\%$	$\nu_{EW} - 20\%$	$\nu_{EW} + 20\%$
E_{EW}	GPa	31.3	25.0	37.6	31.3	31.3
ν_{EW}	-	0.2682	0.2682	0.2682	0.2146	0.3219

Table 4.38 – Material parameters for the varied end winding properties

The mode frequencies resulting from the change of the Poisson's ratio can be seen in table 4.39.

Compared to nominal there are no large changes in mode frequencies. The mode frequencies tend to shift slightly upwards for an increased Poisson's ratio, but the deviation from nominal does not exceed 0.13%. Again the (2,1) mode makes the largest frequency shift.

The deviation from the measured frequencies has only slightly changed compared to the nominal simulation. The reduced Poisson's ratio leads to an improvement, the increased Poisson's ratio to a worsening.

The mode frequencies resulting from the change of the Young's modulus in the end windings can be seen in table 4.40.
From all executed variations the change of the end winding stiffness has the largest

∅ Measurement [Hz]	Simulation $\nu_{EW} - 20\%$ [Hz]	Deviation $\nu_{EW} - 20\%$ [%]	Simulation $\nu_{EW} + 20\%$ [Hz]	Deviation $\nu_{EW} + 20\%$ [%]
514	544	5.88	545	5.95
642	648	1.00	650	1.24
4729	4880	3.19	4880	3.20
6935	6653	-4.06	6654	-4.06
1349	1407	4.30	1407	4.26
1457	1598	9.70	1600	9.80
5190	5064	-2.42	5066	-2.39
5399	4907	-9.11	4907	-9.12

Table 4.39 – Frequency comparison - variation of the Poisson's ratio of the end windings

impact. A reduction of the Young's modulus leads to a downward shift of mode frequencies, this applies more strongly to 1-type modes, especially on the (2,1) mode. For the increased Young's modulus the frequencies are shifted in the opposite direction.
The end winding properties have a considerable impact on the overall vibration behavior of the stator.

∅ Measurement [Hz]	Simulation $E_{EW} - 20\%$ [Hz]	Deviation $E_{EW} - 20\%$ [%]	Simulation $E_{EW} + 20\%$ [Hz]	Deviation $E_{EW} + 20\%$ [%]
514	533	3.69	555	7.91
642	618	-3.72	677	5.48
4729	4866	2.89	4896	3.53
6935	6643	-4.21	6662	-3.94
1349	1393	3.29	1417	5.02
1457	1548	6.23	1641	12.61
5190	5028	-3.12	5115	-1.45
5399	4903	-9.19	4910	-9.07

Table 4.40 – Frequency comparison - variation of the Young's modulus of the end windings

The overall deviation from the measured frequencies has slightly improved for the reduced Young's modulus compared to nominal. Now all modes from the group of good matches lie within the range of $\pm 5\%$ deviation.
For the increased Young's modulus the deviations have grown.

For further investigations the material parameters including the reduced Young's modulus of the end windings are used.

The reduction of the Young's modulus can be apportioned to a change in the equivalent adjustment factor ξ_E. The factor is reduced from $\xi_E = 20.03$ in the nominal case (equations 4.19 and 4.20) to $\xi_E = 11.62$ which corresponds to a shift more towards a serial connection of springs compared to the inital assumption.
Another possible influence is the stiffening effect of the paper bandage which has been omitted in the simulation.

In the course of the parameter study it could be seen that the mode of classification type (2,1) reacts more sensitive to parameter changes than other examined modes. This mode shape is depicted in 4.21.

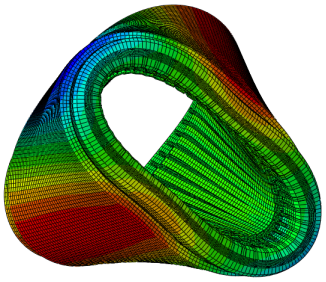

Figure 4.21 – Mode shape (2,1)

4.4.4 Complex-valued Eigenvalue Extraction

In order to check, whether the findings of the complex eigenvalue analysis from the stator of the range extender can be applied to the stator of the HM132, the same damping values are used for the calculation.
This means applying the values from 4.4 and 4.5 to the stator core and for the remaining components the values from 4.17 and 4.17 are used.
The result of the respective simulation run in terms of modal damping can be seen in figure 4.22.

When reusing the damping parameters from the range extender, the modal damping is severely underestimated.
Due to the structural differences between the two stators, the transfer of damping properties is not admissible.
The structural differences are as follows and illustrated by the figures 4.23 (a) and (b):

- The windings of the range extender are fully impregnated with coating material, the end windings are concentrated.
- The end windings of the HM132 are distributed and bandaged.

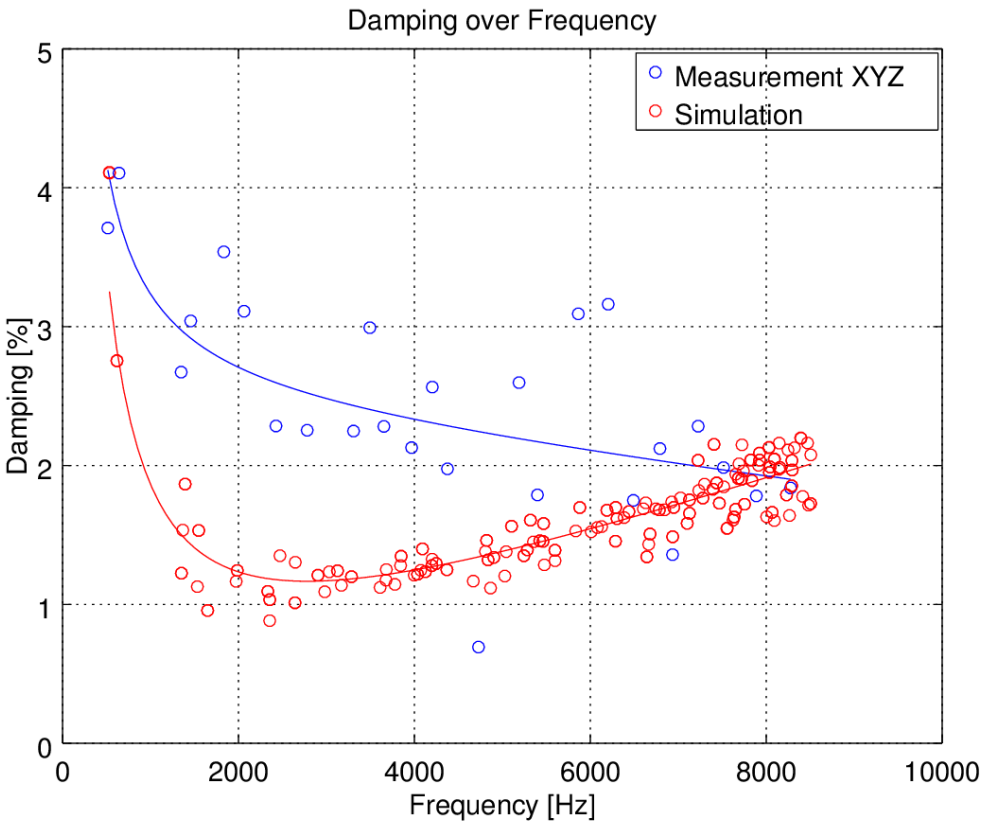

Figure 4.22 – Modal damping when applying the damping parameters from the range extender

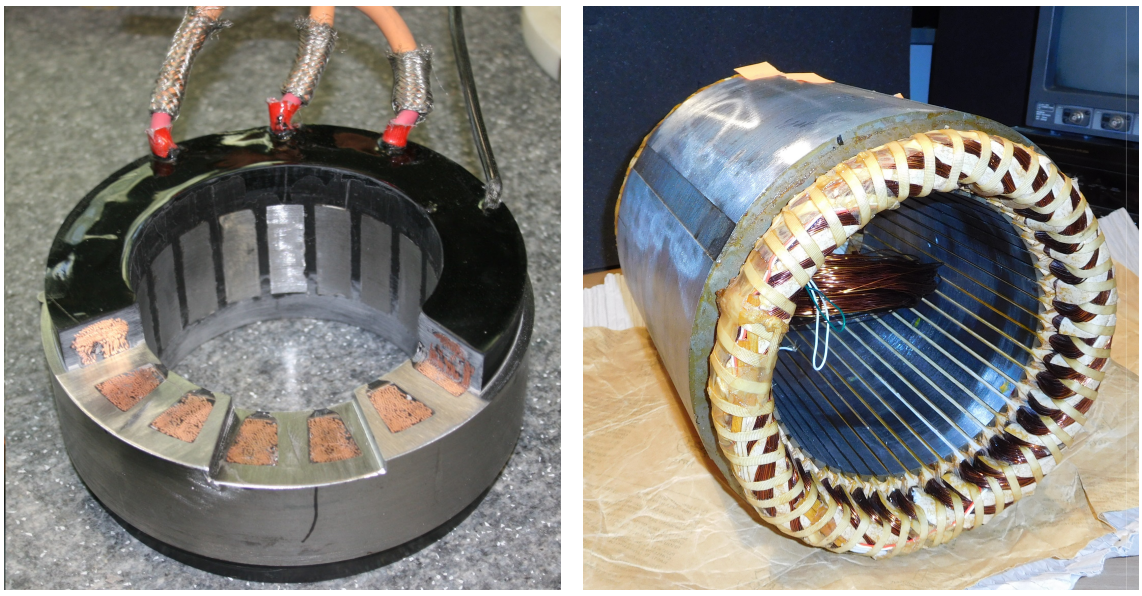

(a) Structure of the stator (Range Extender) (b) Structure of the stator (HM132)

Figure 4.23 – Structural differences between the stators

4.4.5 Forced Response Analysis

As a final step in the analysis of structural dynamics, the forced response analysis is executed.
The determining of damping values proved difficult for the simulation of the stator. In order to fit the curve to the damping values the three parameters α, β, and γ, as they were introduced in the equations 3.1 to **??**, are necessary.
The simulation program only allows for the entering of α and γ. Because of this restriction an error in damping is made that inevitably leads to erroneous amplitudes in the frequency response functions.
The curve fit for the measurement using α, β, and γ along with the curve fit used for the simulation are displayed in figure 4.24.
The used damping parameters can be seen in equations 4.21 and 4.21.

$$\alpha = 600 \, \frac{1}{\mathrm{s}} \tag{4.21}$$

$$\gamma = 5 \times 10^{-7} \, \mathrm{s} \tag{4.22}$$

From 0 to 2 kHz the damping is set too high, which will cause the resonance peaks to be damped to lower amplitudes. Above 2 kHz the opposite is the case.

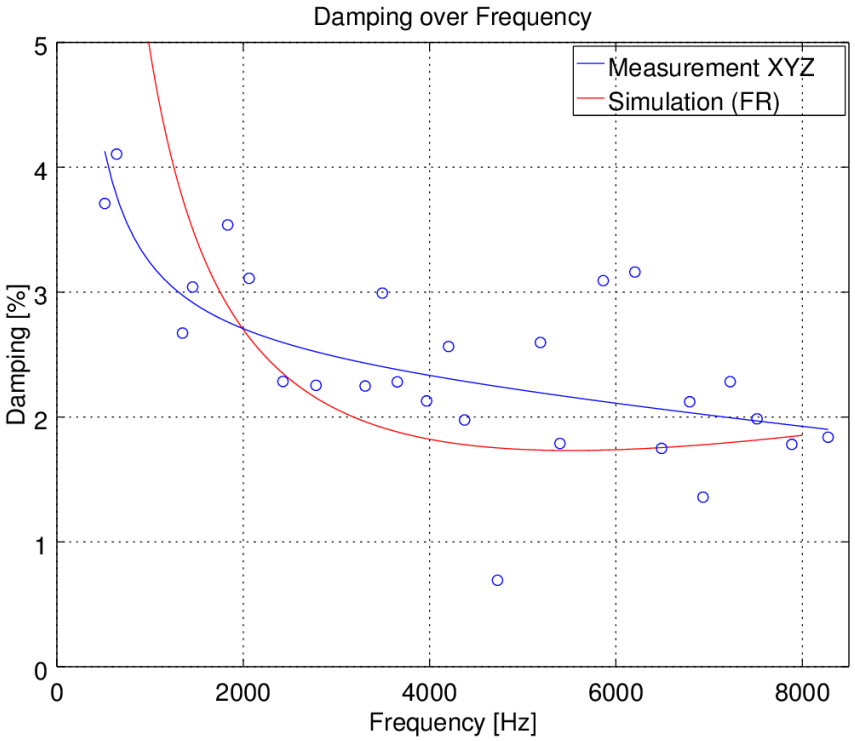

Figure 4.24 – Error in damping

The frequency response functions are generated by applying an instantaneous force of

1 N to the stator.
The results are regarded in three sensor positions and are displayed in terms of velocity (figure 4.25).

The course of the simulated FRF matches the measurement very well around the first two resonance peaks which correspond to the modes with the highest MAC correlation between measurement and simulation.
For the remaining resonances the larger deviations in frequency are visible in the comparison.

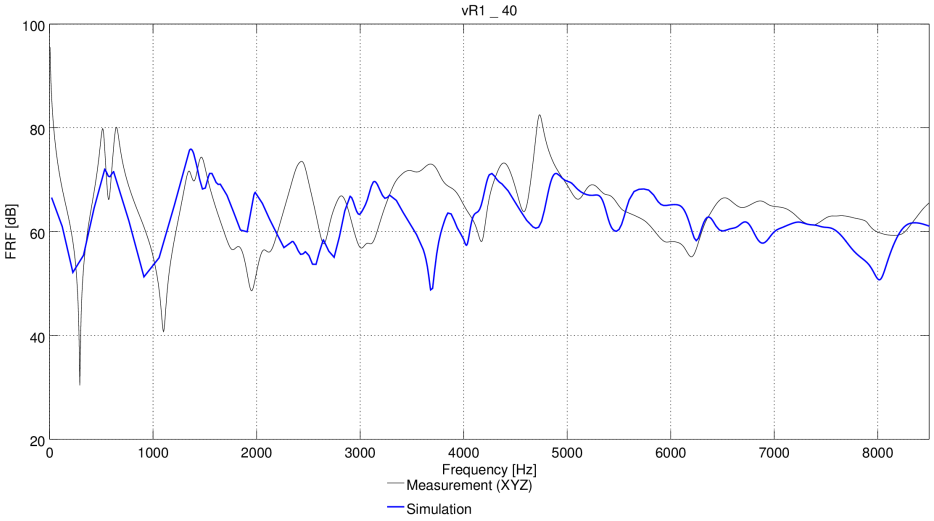

(a) FRFs at sensor vR1_40

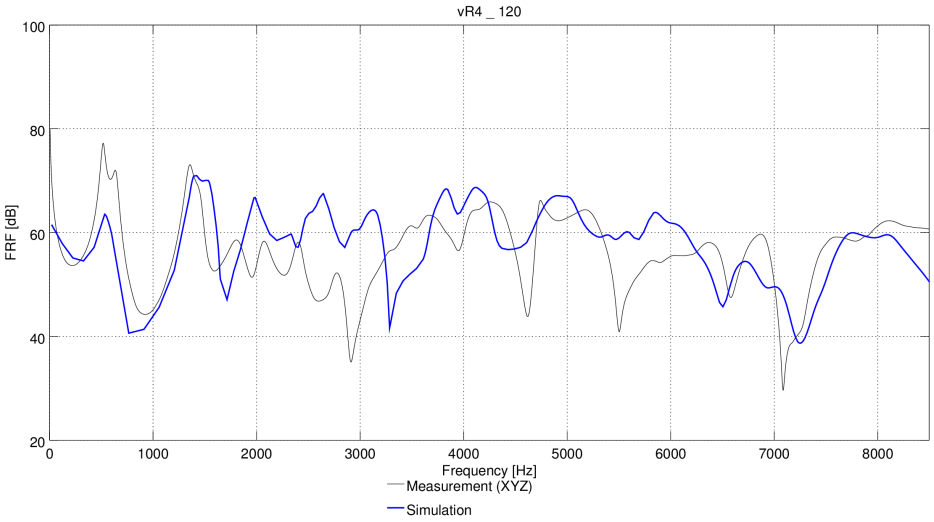

(b) FRFs at sensor vR4_120

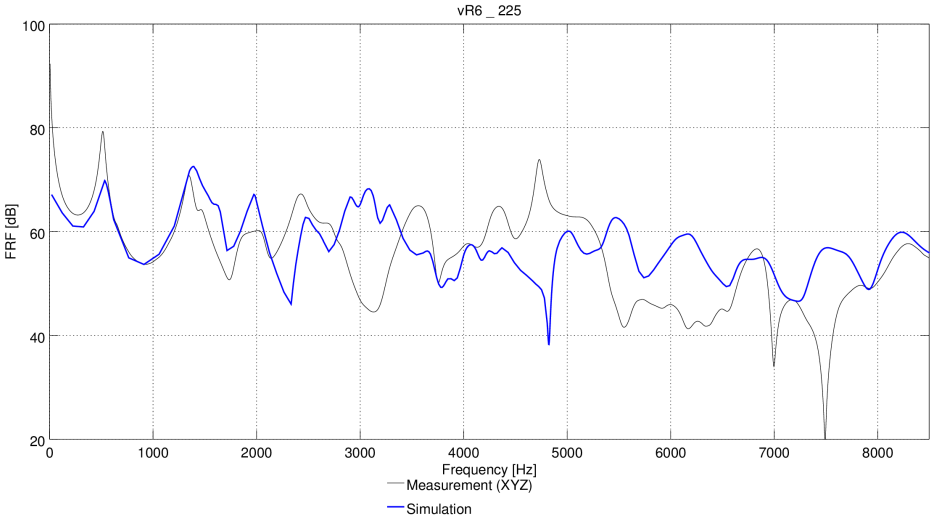

(c) FRFs at sensor vR6_225

Figure 4.25 – FRF comparison measurement/simulation in three different sensor positions

4.4.6 Summary of the Results

The mechanical properties of the end windings have a large impact on the vibration behavior of the stator. With a correct setting of their properties an approximation of mode frequencies is possible.
A transfer of damping data from the structurally different stator of the HM132 to the stator of the range extender is not applicable.
In the selection of sensor positions in the measurement, it should be taken care of a sufficiently good spatial resolution to render a validation possible. A preceding calculation of the AutoMAC may help in choosing appropriate positions.

5 Simulation of Acoustic Emission

The simulation of the acoustic emission is based on a model of the complete electric machine HM132 including the housing and a frame it is mounted on. For the structural dynamic simulation, the model [4] was excited using electromagnetic forces corresponding to the 48^{th} order. This order was identified as an important noise source beforehand as the 48 teeth of the stator core are strongly excited.
The eigenforms and modal contribution data from this model were subsequently used for the sound emission simulations using EXCITE$^{\mathrm{TM}}$ Acoustics.

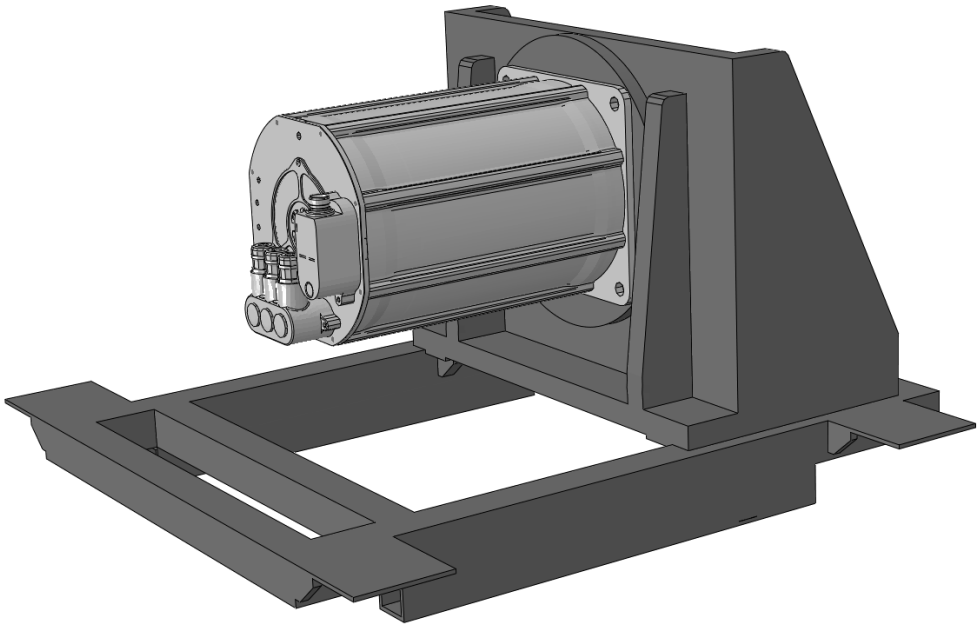

Figure 5.1 – Structural dynamic model of the electric machine

5.1 Theoretical Background

The modal contribution fraction MCF_i is the contribution to the displacement d at sensor position x_j at one specific frequency for one mode i. It is calculated from the mode shape of the i^{th} mode $\boldsymbol{\phi}_i(x_j)$ at the chosen sensor position and the location independent modal participation factor MPF_i (equation 5.1). When performing the summation of the MCFs for all possible modes, the total displacement can be calculated, as is done in equation 5.2.

4. The model was provided by AVL

Not all modes contribute to the displacement equally strong. There are few modes that mostly determine the displacement. Therefore, these most dominant modes can be used to approximate the total displacement. In equation 5.3 the four most relevant modes are chosen for the approximation based on the most prominent peaks in the displacement data over frequency.

$$\mathrm{MCF}_i(x_j, f) = \mathrm{MPF}_i(f) \cdot \boldsymbol{\phi}_i(x_j) \tag{5.1}$$

$$d(x_j, f) = \sum_{i=1}^{N} \mathrm{MCF}_i(x_j, f) \tag{5.2}$$

$$d(x_j, f) \approx \sum_{i=1}^{4} \mathrm{MCF}_i(x_j, f) \tag{5.3}$$

A similar approach can be used to calculate the sound pressure at one specific microphone position.
Instead of the mode shape $\boldsymbol{\phi}_i(x_j)$, the solution of the Helmholtz-Equation (equation 5.4) at the microphone position $\Pi(x_k)$ based on the surface velocity of the electric machine v is used. v is the first derivative of $\boldsymbol{\phi}_i$ by time (equation 5.5).

$$\nabla^2 p_i(x_k) + k^2 p_i(x_k) = 0 \tag{5.4}$$

$$\frac{j}{\rho\omega} \nabla p_i(x_k) = v = j\omega \cdot \boldsymbol{\phi}_i \tag{5.5}$$

The MPFs can then be reused to calculate the sound pressure in a specified microphone position x_k. The sound pressure can be approximated using the sum of the sound emission of the four most relevant eigenforms. The relevance of these eigenforms lies in their potential to effectively emit sound into the far field.

$$p(x_k, f) = \sum_{i=1}^{N} \mathrm{MPF}_i(f) \cdot p_i(x_k) \tag{5.6}$$

$$p(x_k, f) \approx \sum_{i=1}^{4} \mathrm{MPF}_i(f) \cdot p_i(x_k) \tag{5.7}$$

5.2 Modal Contribution Fractions

In order to verify whether the four most prominent modes can sufficiently approximate the total surface displacement, a comparison is performed.
For the approximation the four modes with the eigenfrequencies 714 Hz, 726 Hz, 2931 Hz

and 4827 Hz are used. Their MCFs are summed up in order to approximate the displacement.
The comparison is performed at three sensor positions in one direction each on the housing surface. Figures 5.2 to 5.4 show the comparison between the magnitude of the summed MCFs and the total displacement (top) along with the contributions of the four respective modes at these positions (bottom).

For the different sensor positions, the quality of the approximation varies with different frequency ranges. For sensor 1021 the approximation is good from 1.2 kHz upwards, around the two lower eigenfrequencies there is a noticeable deviation (figure 5.2).

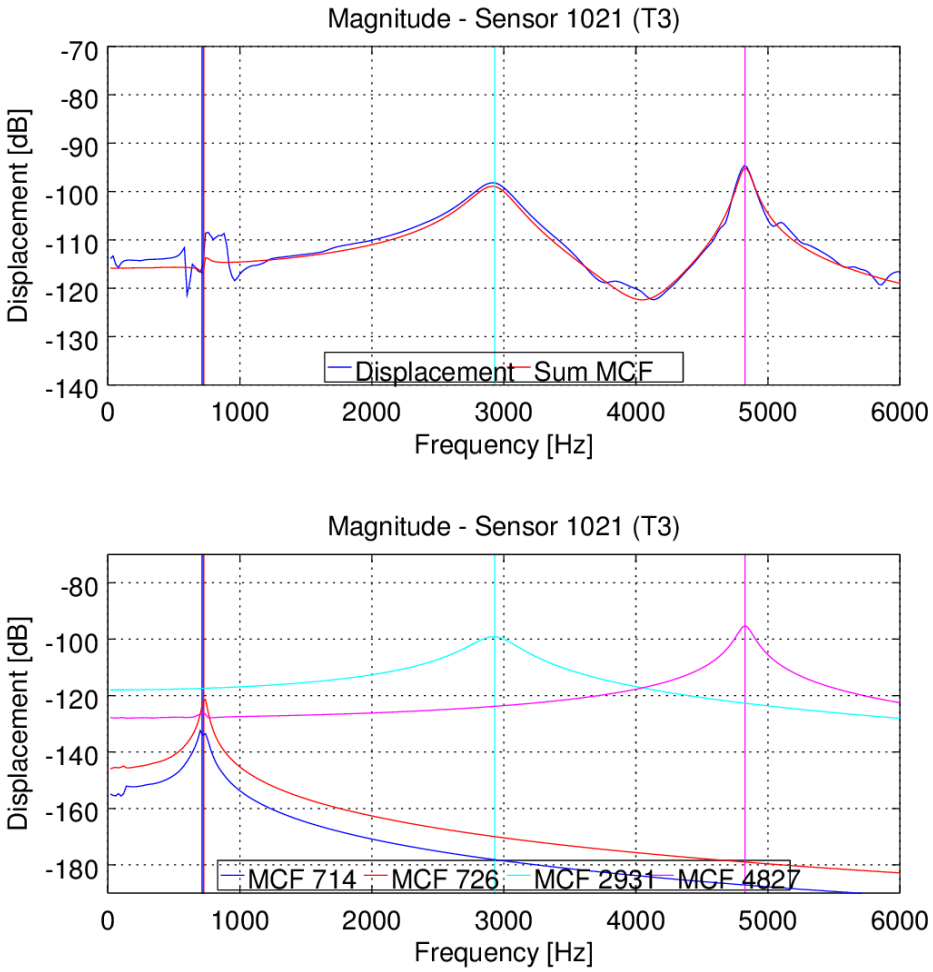

Figure 5.2 – Comparison of total displacement and sum of the MCFs of the four most relevant modes (top) and the contributions of the respective modes (bottom) in sensor position 1021

A deviation of the two curves at lower frequencies can also be seen at sensor 1023.

Around the third eigenfrequency at 2931 Hz the sum of MCFs underestimates the displacement, some influences from other modes seem to miss in that frequency range. From 4.6 kHz the concordance between the curves is good (figure 5.3).

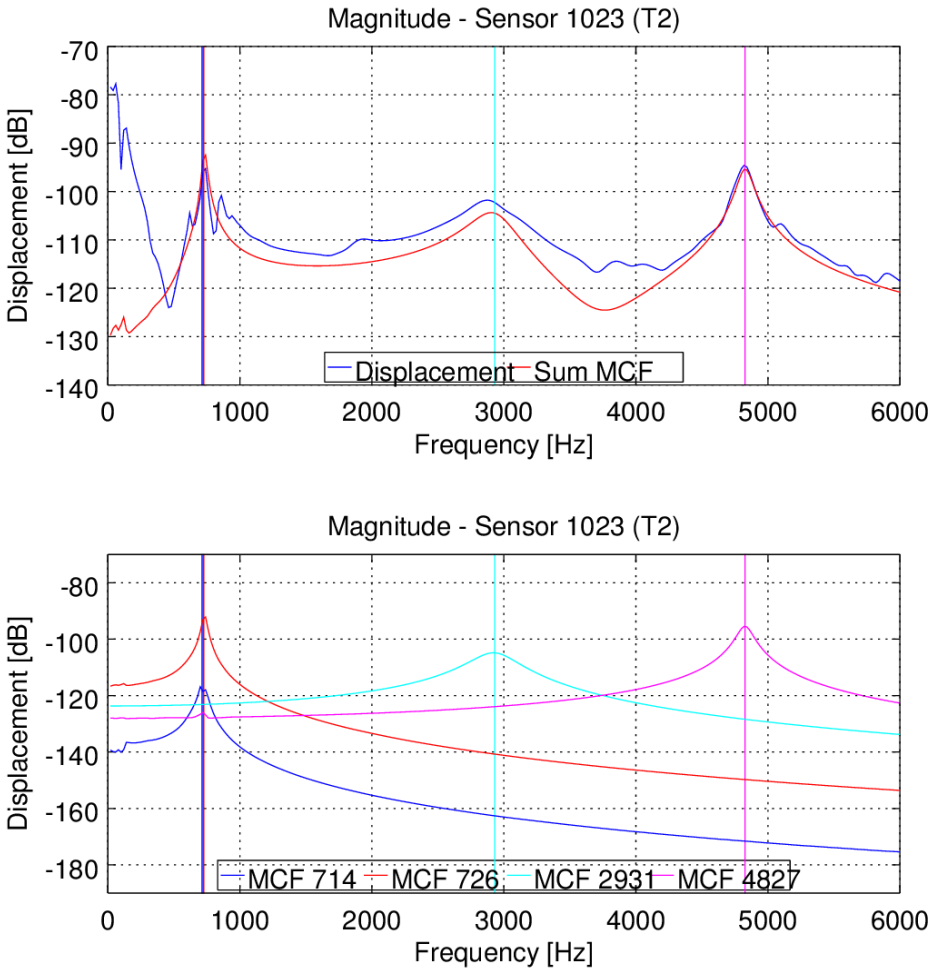

Figure 5.3 – Comparison of total displacement and sum of the MCFs of the four most relevant modes (top) and the contributions of the respective modes (bottom) in sensor position 1023

At sensor 1026 the range around the first two eigenfrequencies is approximated very well, in the middle frequency range again an underestimation can be seen. The resonance peak of the fourth mode coincides well with the total displacement (figure 5.4).

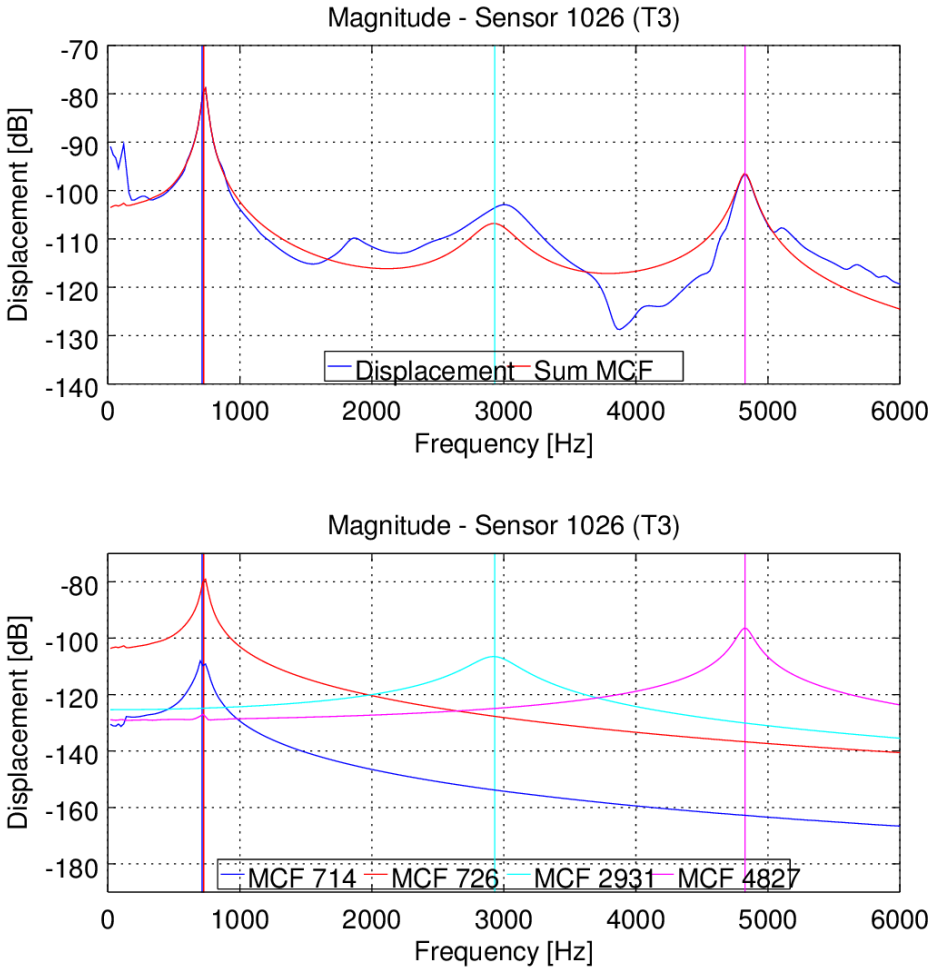

Figure 5.4 – Comparison of total displacement and sum of the MCFs of the four most relevant modes (top) and the contributions of the respective modes (bottom) in sensor position 1026

In conclusion is can be said that the overall approximation works in consideration of the different sensor positions although not all influences from the eigenvectors are considered.

5.3 Solution for Helmholtz Equation for the Chosen Eigenforms

The four chosen eigenvectors are used as input for a sound emission calculation using the WBT tool EXCITE^{TM} Acoustics [41]. The calculation is done from 20 Hz to 5 kHz in steps of 20 Hz. The solutions for the individual modes at one chosen microphone position (lateral, 1 m distance) are displayed in the following figures 5.5 to 5.8. The top part of the figures shows the Sound Pressure Level (SPL), the bottom part shows the

unwrapped phase corrected by $k \cdot r$. k denotes the wave number, r is the distance to the microphone of 1 m. The addition of this factor eliminates the steady descent of the phase and highlights phase shifts. The fluctuations that are visible above 3.5 kHz are rooted in the realization of the WBT and are therefore a methodical problem. Increasing the number of wave functions, radiation functions, and Gauss points did not lead to an improvement.

The course of the solutions may help in estimating the necessary number of sampling points in future implementations of the calculation. Especially in the higher frequency range the calculation is very costly. An even frequency response allows for the use of fewer sampling points and therefore reduces computation time considerably.

For the two lower modes at 714 Hz and 726 Hz there are slumps in the magnitude that coincide with phase jumps. This may be explained by the radiation behavior of the respective eigenforms ((2,0) and 1st torsion) which leads to destructive interference for some frequencies. This behavior does not allow for a reduction of sampling points at higher frequencies.

The magnitude of the other two modes ((4,0) and (0,0)) is more uniform and constant - especially at higher frequencies. The eigenforms of these modes resemble an acoustic monopole, therefore there is much less destructive interference.
A reduction of sampling points is admittable for these types of modes which implies a considerable saving of calculation time.

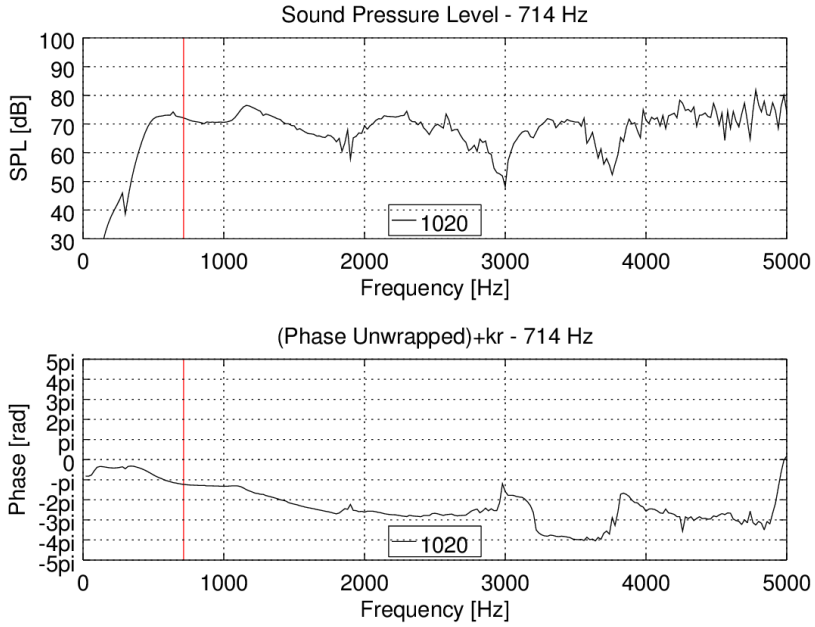

Figure 5.5 – Solution for Helmholtz equation in microphone position 1020 based on the eigenform at 714 Hz

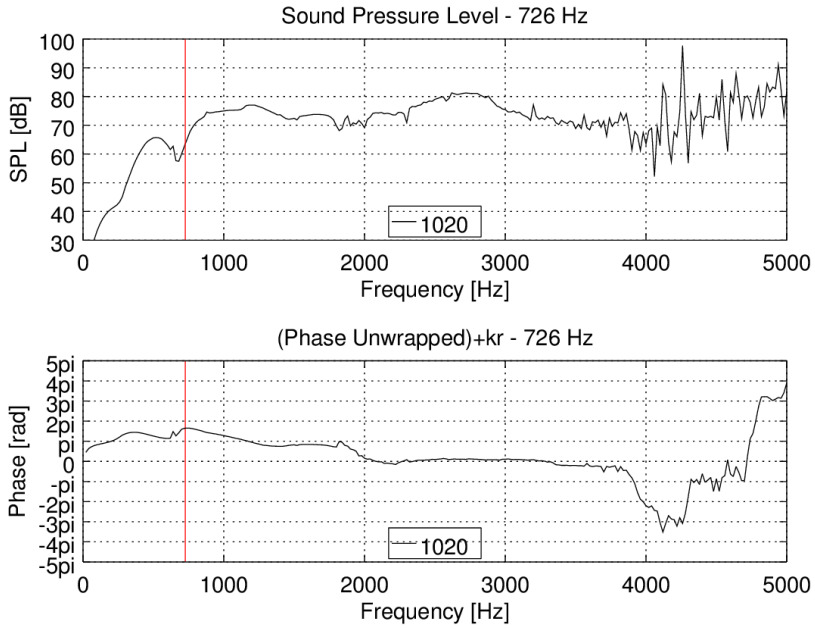

Figure 5.6 – Solution for Helmholtz equation in microphone position 1020 based on the eigenform at 726 Hz

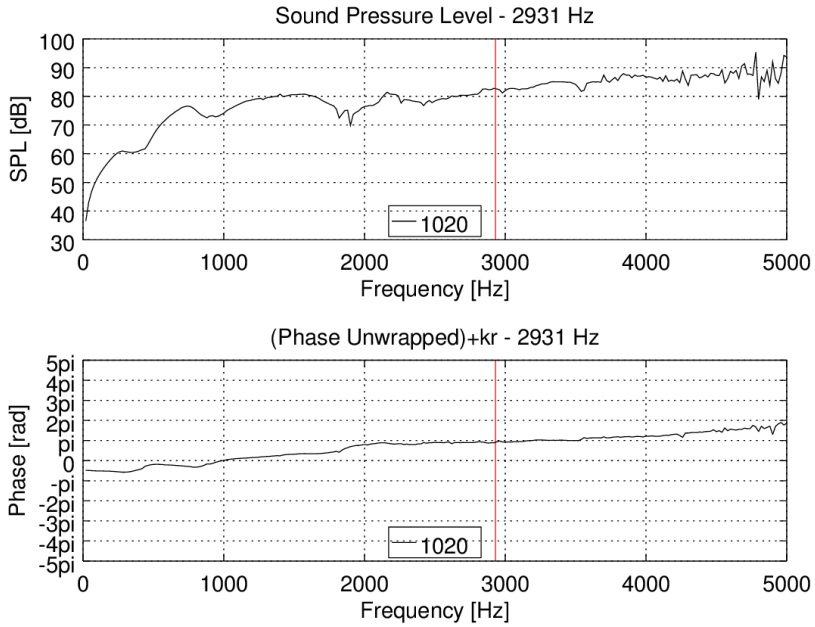

Figure 5.7 – Solution for Helmholtz equation in microphone position 1020 based on the eigenform at 2931 Hz

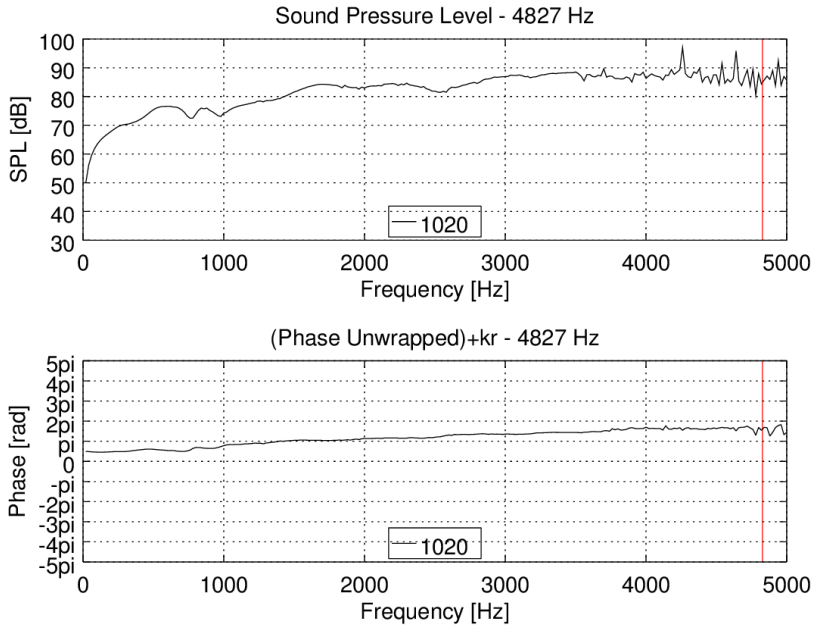

Figure 5.8 – Solution for Helmholtz equation in microphone position 1020 based on the eigenform at 4827 Hz

5.4 Total Sound Pressure

For the comparison of the partial simulation based on four modes, with the complete simulation result that considered all modes and with the measurement, the results from the simulation of the single modes are multiplied with their respective MPFs and subsequently added up.
Figure 5.9 shows the comparison in the same microphone position that was chosen before. The abscissa of the display is scaled in RPM - corresponding to the excitation at the 48^{th} order. 4000 RPM are equivalent to 5000 Hz.

The peak around the two lower modes coincides well between complete simulation and partial simulation, also in the measurement a peak can be seen at that frequency. In the middle frequency range where the displacements have been rather underestimated by the approximation, the sound pressure is overestimated. The deviations may be caused by missing influences from modes that are not considered in the summation. Towards higher frequencies the course of full simulation, partial simulation and measurement match well, although the level of the partial simulation is a bit lower.

The method for approximating the sound emission shows room for improvement regarding the choice of eigenvectors, yet the results are promising.
Further investigations in that direction may be worthwhile to accomplish a much reduced computation time in the simulation of sound emission.

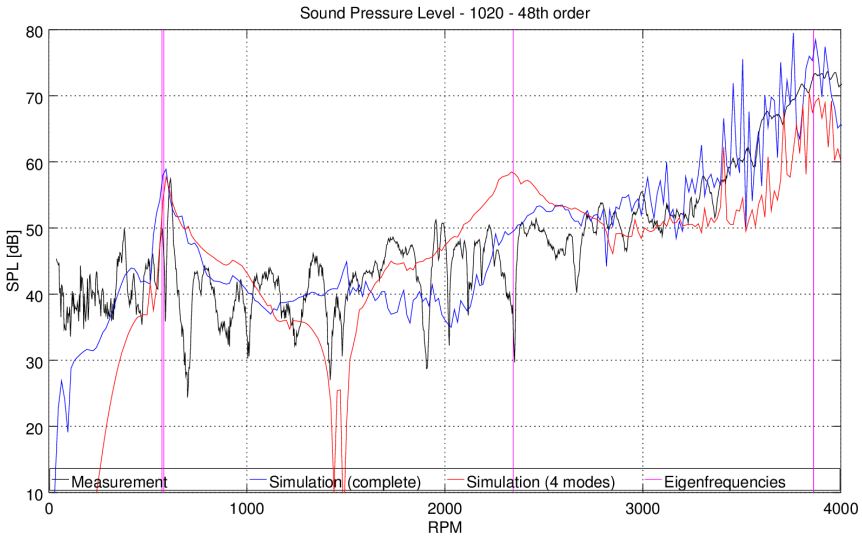

Figure 5.9 – Total sound emission in one microphone position - comparison between full simulation, simulation with four eigenforms and measurement

6 Conclusion and Outlook

Experimental modal analysis The experimental modal analysis as a basis for validation yields some interesting observations and conclusions.

In the production of lamination stacks there is noticeable production tolerance which impedes predictive modeling.
Depending on the mode classification type there are systematic deviations in mode frequencies and modal damping for the lamination stack. Modes with deformation along the machine axis show a higher deviation in mode frequencies and a higher level in modal damping than modes that deform purely in radial direction.

The impact force in modal testing has to be high enough to excite the structure's relevant mode shapes and to guarantee good measurement quality. Yet the impact force should not exceed the bounds of linearity. As a reference point for the magnitude of the excitation force, the forces yielded in operating state should be regarded. Further investigations to adapt the measurement set-up should be endeavored.

The positioning of sensors should yield a sufficiently good spatial resolution. The AutoMAC can be used as a mean for verifying the quality of the sensor positioning before performing experiments.

Simulation of structural dynamics The findings from the simulation of structural dynamics are listed in the following.

Simulation of the lamination stack:
Different parameters have impact on mode frequencies of different classification types with varying degrees of intensity.
While the 0-type modes are mainly determined by the properties of the electric steel, the 1-type modes are strongly influenced by variations in steel percentage and the Young's modulus of varnish.
The influence of changes in the Poisson's ratio of the components is almost negligible.

The simulation using transverse isotropic modeling of the sheets yields a good result with a slight overestimation of mode frequencies.
To improve the modeling, detailed knowledge about the stack's component's mechanical properties is essential. Measurements in order to determine the stiffness properties of steel and varnish are advisable in order to enhance the modeling quality.

An implementation of direction dependent damping properties is to be sought to avoid a systematic modeling error.

Simulation of the stator (Range Extender):
Neglecting the influence of the insulation paper is not admissible for sufficient modeling. A good estimation of the properties of the paper section permits a good modeling of eigenfrequencies. Therefore the properties of insulating paper and coating should be determined experimentally to allow for predictive modeling.
The influence of the adjustment factors in the calculation of the homogenized winding

properties and the Poisson's ratios of the different components is small.

Not only the stiffness properties, but also the damping properties of the different components should be investigated to obtain better results in complex eigenvalue analysis. The executed complex eigenvalue analysis suggests that for the stator with concentrated and impregnated windings, the damping is mainly determined by the inner damping. The influence of the mass proportional damping is little.

Simulation of the stator (HM132):
The structural dynamic behavior of the stator is strongly influenced by the stiffness properties of the end windings whereas the coating properties have only a little impact on mode frequencies.
Appropriate material settings for the end winding enable an approximation of mode frequencies.
Further investigations regarding the properties of the end windings that take into account the influence of the winding distribution and the paper bandage may lead to an improved modeling.

It could be observed that the mode of classification type (2,1) reacts more sensitive to changes of material parameters than the other examined modes.

The structural differences between the two examined stators impede the transfer of damping properties from one stator to another.

Simulation of acoustic emission The presented method includes an approximation of the excited structure's displacement and the resulting sound emission using a subset of four eigenvectors.

The approximation of the structure's displacement is possible, yet some structural influences are missing.

The radiation behavior of the eigenvectors differs depending on the mode shape.
Monopole-resembling shapes exhibit a relatively even magnitude course over frequency. Destructive interference occurs for other shapes which leads to slumps in the magnitude. The even character of the magnitude for the monopole-like shapes allows for a reduction of sampling points which shortens the computation time considerably.

The approximation of the total sound emission shows promising results, yet further investigations are necessary to improve the method's performance.

A Shape and Size Metrics of the Meshes

The following metrics are used to describe the quality of the mesh elements:

Shape Factor: Ratio between element volume and optimal element volume (for tetrahedral elements)

Face Angle: Angle between two edges of a face (for triangular and quadratic faces)

Aspect Ratio: Ratio between the longest and the shortest edge of an element (for tetrahedral and hexahedral elements)

Geometric deviation: Deviation of the element from the original geometry (for tetrahedral and hexahedral elements, not available for the HM132 stator)

Edge length: Length of edges (for tetrahedral and hexahedral elements)

Metric	Type	Unit	Laminated Sheets	Stator RE - WOP	Stator RE - WP	Stator HM132
Worst Shape Factor	tet	-	-	2.02E-14	1.10E-5	-
∅ Shape Factor	tet	-	-	0.595706	0.63204	-
Worst min. angle	tri	°	-	0.0762	1.82	-
∅ min. angle	tri	°	-	35.12	36.10	-
Worst min. angle	quad	°	23.19	17.38	14.73	22.51
∅ min. angle	quad	°	83.07	75.20	80.99	81.32
Worst max. angle	tri	°	-	177.64	174.66	-
∅ max. angle	tri	°	-	90.59	89.38	-
Worst max. angle	quad	°	167.18	172.31	169.99	157.49
∅ max. angle	quad	°	97.17	105.24	99.25	100.32
Worst aspect ratio	tet	-	-	752.4	14.05	-
∅ aspect ratio	tet	-	-	2.06	1.90	-
Worst aspect ratio	hex	-	10.57	12.59	14.39	22.17
∅ aspect ratio	hex	-	1.42	1.75	1.85	5.18
Worst geom. deviation	tet	-	-	0.172	0.219	-
∅ geom. deviation	tet	-	-	9.02E-4	4.44E-4	-
Worst geom. deviation	hex	-	0.218	0.107	0.218	-
∅ geom. deviation	hex	-	0.00673	0.00733	0.008977	-
Shortest edge	tet	mm	-	0.00262	0.146	-
∅ min. edge length	tet	mm	-	1.31	1.2767	-
Shortest edge	hex	mm	0.163	0.137	0.129	0.33
∅ min. edge length	hex	mm	1.36	1.31	1.13	1.58
Longest edge	tet	mm	-	6.87	3.64	-
∅ max. edge length	tet	mm	-	2.30	2.14	-
Longest edge	hex	mm	2.90	4.32	3.33	8.81
∅ max. edge length	hex	mm	1.78	2.04	1.73	4.91

B Material Parameters for the Simulations of the Lamination Stack based on the roughly estimated material properties

Quantity	Unit	Nom	$l_V = 6\,\mu m$	Δ
ϕ_{St}	%	98.86	98.29	-0.58%
ρ	$\frac{kg}{m^3}$	7576	7539	-0.49%
E_p	MPa	207640	206460	-0.57%
E_z	MPa	125420	104403	-16.76%
ν_p	-	0.3	0.3	$\pm 0.00\%$
ν_{zp}	-	0.1812	0.1517	-16.28%
G_p	MPa	79861	79408	-0.57%
G_{zp}	MPa	48239	40155	-16.76%

Table B.1 – Material parameters for the changed steel percentage

Quantity	Unit	Nom	$E_f - 20\%$	$E_m - 20\%$
ϕ_{St}	%	98.86	98.86	98.86
ρ	$\frac{kg}{m^3}$	7576	7576	7576
E_p	MPa	207640	166120	207632
E_z	MPa	125420	109289	113771
ν_p	-	0.3	0.3	0.3
ν_{zp}	-	0.1812	0.1974	0.1644
G_p	MPa	79861	63892	79858
G_{zp}	MPa	48239	42034	43758

Table B.2 – Material parameters for the variation of Young's moduli

C Nomenclature

C.1 Latin Characters

Symbol	Description	Unit
A	Area	m^2
$\mathbf{A}$	Linear operator	-
c	Viscous damping	-
d	Thickness	m
d	Displacement	m
$D_{W1,2}$	Winding diameter	m
E	Young's modulus	MPa
$\mathbf{E}$	Unit matrix	-
f, F	Force	N
f	Frequency	Hz
G	Shear modulus	MPa
h	Structural damping	-
h_l	Hankel functions	-
j	Imaginary unit	-
k	Stiffness	N/m
k	Wave number	1/m
l	Length	m
m	Mass	kg
n	Sheet quantity	-
N_W	Number of windings	-
p	Sound pressure	Pa
$\mathbf{r}$	Distance, radius	m
r_T	Truncation radius	m
S_D	Hardness	-
t	Time	s
v	Velocity	m/s
x, y, z	Cartesian coordinates	m
x	Displacement	m
$X(\omega)$	System response	-
Y_{lm}	Spherical harmonics	-

C.2 Greek Characters

Symbol	Description	Unit
α_n	Polynomial coefficient	-
$\alpha(\omega)$	Receptance	m/N
α	Mass proportional damping	1/s
β	Velocity proportional damping	-
γ	Stiffness proportional damping	s
γ	Shear strain	m/m
Γ	Boundary condition	-
$\varepsilon_{el,xx,zz}$	Strain	m/m
η_E	Calculation factor for Young's modulus in Halpin-Tsai method	-
η_G	Calculation factor for shear modulus in Halpin-Tsai method	-
θ, r, z	Cylindrical coordinates	-
λ	Eigenvalue	-
Λ	Matrix of eigenvalues	-
μ	Calculation factor for Poisson's ratio in Halpin-Tsai method	-
μ_k	Algebraic multiplicity of eigenvalues	-
ν	Poisson's ratio	-
ξ_E	Adjustment factor for Young's modulus	-
ξ_G	Adjustment factor for shear modulus	-
ζ	Damping ratio	-
ρ	Density	$\frac{\text{kg}}{\text{m}^3}$
σ_{el}	Stress	Pa
τ	Shear stress	Pa
ϕ_{Cu}	Copper percentage	%
ϕ_{St}	Steel percentage	%
$\boldsymbol{\phi}_i$	Eigenvector, Mode shape	-
$\boldsymbol{\Phi}_i$	Matrix of eigenvectors	-
φ	Shear angle	°
$\phi_{w_{r,s,t}}$	Wave sets	-
ω	Angular frequency	1/s
Ω	Fluid domain	-

C.3 Abbreviations

Abbreviation	Description
DoF	Degree of freedom
FE	Finite-element
FEM	Finite-element method
FRF	Forced Response Function
MAC	Modal Assurance Criterion
MCF	Modal Contribution Fraction
MPF	Modal Participation Factor
MBS	Multi-Body-Simulation
NM	New Material
Nom	Nominal
PMSM	Permanent magnet excited synchronous machine
PS	Paper section
RPM	Revolutions per minute
SDoF	Single degree of freedom
SPL	Sound Pressure Level
WBT	Wave Based Technique
WOP	Without paper
WP	With paper
+	Low excitation force level
++	Medium excitation force level
+++	High excitation force level

C.4 Scalars, Vectors and Matrices

Symbol	Description
x	Scalar
$\mathbf{x}$	Vector
$\mathbf{X}$	Matrix

References

[1] J. Weickert, "Kapitel: Eigenwerte und Eigenvektoren." Website. Online available `https://web.archive.org/web/20121119065630/http://www.mia.uni-saarland.de/Teaching/MFI07/kap45.pdf`; accessed on 27th of July 2017.

[2] J. He and Z.-F. Fu, *Modal Analysis*. Butterworth Heinemann, 2001.

[3] R. J. Allemang, "The Modal Assurance Criterion - Twenty Years of Use and Abuse," *Sound and Vibration*, vol. 37, pp. 14–21, August 2003.

[4] L. Issler, H. Ruoß, and P. Häfele, *Festigkeitslehre Grundlagen*. Springer, 1995.

[5] Wikipedia, "Poissonzahl." Website. Online available `https://de.wikipedia.org/wiki/Poissonzahl`; accessed on 27th of July 2017.

[6] Wikipedia, "Shear modulus." Website. Online available `https://en.wikipedia.org/wiki/Shear_modulus`; accessed on 27th of July 2017.

[7] G. Müller and B. Ponick, *Grundlagen elektrischer Maschinen*. Wiley-VCH, 10 ed., 2014.

[8] C. Wang and J. Lai, "Vibration analysis of an induction motor," *Journal of Sound and Vibration*, vol. 224, no. 4, pp. 733 – 756, 1999.

[9] M. Schwarzer, *Structural Dynamic Modeling and Simulation of Acoustic Sound Emissions of Electric Traction Motors*. PhD thesis, Technische Universität, Darmstadt, 2017.

[10] I. Ramesohl, G. Henneberger, S. Kuppers, and W. Hadrys, "Three dimensional calculation of magnetic forces and displacements of a claw-pole generator," *IEEE Transactions on Magnetics*, vol. 32, pp. 1685–1688, May 1996.

[11] I. Ramesohl, C. Kaehler, and G. Henneberger, "Influencing factors on acoustical simulations including manufacturing tolerances and numerical strategies," in *1999. Ninth International Conference on Electrical Machines and Drives (Conf. Publ. No. 468)*, pp. 142–146, 1999.

[12] D. Franck, M. van der Giet, and K. Hameyer, "Towards low audible noise drives for FEV applications," in *Proceedings of 14th International Power Electronics and Motion Control Conference EPE-PEMC 2010*, pp. S11–25–S11–30, Sept 2010.

[13] S. Sakamoto, T. Hirata, T. Kobayashi, and K. Kajiwara, "Vibration analysis considering higher harmonics of electromagnetic forces for rotating electric machines," *IEEE Transactions on Magnetics*, vol. 35, pp. 1662–1665, May 1999.

[14] S. A. Long, Z. Q. Zhu, and D. Howe, "Vibration behaviour of stators of switched reluctance motors," *IEE Proceedings - Electric Power Applications*, vol. 148, pp. 257–264, May 2001.

[15] S. Singhal, K. V. Singh, and A. Hyder, "Effect of laminated core on rotor mode shape of large high speed induction motor," in *2011 IEEE International Electric Machines Drives Conference (IEMDC)*, pp. 1557–1562, May 2011.

[16] J. B. Dupont, P. Bouvet, and L. Humbert, "Vibroacoustic simulation of an electric motor: Methodology and focus on the structural FEM representativity," in *2012 XXth International Conference on Electrical Machines*, pp. 3027–3033, Sept 2012.

[17] X. Li, S. Huang, Q. Zhang, and Y. Dai, "Electromagnetic noise assessment for EV's PM driving machines," in *2014 17th International Conference on Electrical Machines and Systems (ICEMS)*, pp. 1552–1555, Oct 2014.

[18] R. Nitzsche, *Elektromagnetisch erzwungene und Eigenschwingungen des Statorgehäuses eines zweipoligen Turbogenerators*. PhD thesis, Fachbereich Elektrotechnik und Informationstechnik der Universität Hannover, 1998.

[19] H. Wang and K. Williams, "The vibrational analysis and experimental verification of a plane electrical machine stator model," *Mechanical Systems and Signal Processing*, vol. 9, no. 4, pp. 429 – 438, 1995.

[20] H. Wang and K. Williams, "Effects of laminations on the vibrational behaviour of electrical machine stators," *Journal of Sound and Vibration*, vol. 202, no. 5, pp. 703 – 715, 1997.

[21] M. van der Giet, K. Kasper, R. W. D. Doncker, and K. Hameyer, "Material parameters for the structural dynamic simulation of electrical machines," in *2012 XXth International Conference on Electrical Machines*, pp. 2994–2995, Sept 2012.

[22] K. H. Yim, J. W. Jang, G. H. Jang, M. G. Kim, and K. N. Kim, "Forced Vibration Analysis of an IPM Motor for Electrical Vehicles due to Magnetic Force," *IEEE Transactions on Magnetics*, vol. 48, pp. 2981–2984, Nov 2012.

[23] S. Watanabe, S. Kenjo, K. Ide, F. Sato, and M. Yamamoto, "Natural Frequencies and Vibration Behaviour of Motor Stators," *IEEE Transactions on Power Apparatus and Systems*, vol. PAS-102, pp. 949–956, April 1983.

[24] S. Noda, S. Mori, F. Ishibashi, and K. Itomi, "Effect of Coils on Natural Frequencies of Stator Cores in Small Induction Motors," *IEEE Transactions on Energy Conversion*, vol. EC-2, pp. 93–99, March 1987.

[25] W. Cai, P. Pillay, and Z. Tang, "Impact of stator windings and end-bells on resonant frequencies and mode shapes of switched reluctance motors," *IEEE Transactions on Industry Applications*, vol. 38, pp. 1027–1036, Jul 2002.

[26] Z. Fengge, T. Ningze, and W. Fengxiang, "Analysis of vibration modes for large induction motor," in *2005 International Conference on Electrical Machines and Systems*, vol. 1, pp. 64–67 Vol. 1, Sept 2005.

[27] T. Ishikawa, *Analysis of natural frequency, radial force and vibration of induction motors fed by PWM inverter*. INTECH Open Access Publisher, 2012.

[28] B. Weilharter, M. Mair, H. Lang, K. Ellermann, and O. Bíró, "Experimental investigation of the vibration behaviour of a laminated stack with winding," in *IECON 2013 - 39th Annual Conference of the IEEE Industrial Electronics Society*, pp. 2816–2820, Nov 2013.

[29] R. Lin, A. N. Laiho, A. Haavisto, and A. Arkkio, "End-Winding Vibrations Caused by Steady-State Magnetic Forces in an Induction Machine," *IEEE Transactions on Magnetics*, vol. 46, pp. 2665–2674, July 2010.

[30] M. G. N. M. Oudendijk, "Mechanical Aspects of High-Field Magnet Coil-Systems," tech. rep., University of Amsterdam, Eindhoven University of Technology, May 1995.

[31] B. Harris, *Engineering composite materials*. London: The Institute of Materials, 1999.

[32] T. Mócsai, H.-H. Priebsch, F. Diwoky, and A. Hepberger, "Engine Radiation Simulation up to 3kHz using the Wave Based Technique," in *Proc. of the ICSV 2009 - The 16th International Congress on Sound and Vibration*, (Krakow, Poland), 2009.

[33] T. Mócsai, F. Diwoky, A. Hepberger, H.-H. Priebsch, and F. Augusztinovicz, "Application and analysis of an adaptive wave-based technique based on a boundary error indicator for the sound radiation simulation of a combustion engine model," *Computer Assisted Methods in Engineering and Science*, vol. 22, no. 1, pp. 3–30, 2017.

[34] Vibrant Technologies, Inc., Scotts Valley, CA, USA, *ME'scopeVES: Tutorial Manual*, 2014.

[35] A. Gernemann, "Kohärenz und Korrelation in der Tonstudiotechnik." Website. Online available `http://www.uni-koeln.de/phil-fak/muwi/ag/tec/kohkor.pdf`; accessed on 27th of November 2017.

[36] M. Mair, "Numerische und Experimentelle Modalanalyse eines Statorblechpaketes," Master's thesis, Technische Universität Graz, Graz, 2010.

[37] Dassault Systèmes Simulia Corp., Providence, RI, USA, *Abaqus CAE: User's Guide*, 2014. Online available `http://abaqus.software.polimi.it/v6.14/books/usi/default.htm`; accessed on 27th of November 2017.

[38] CogentPowerLtd, "Electrical Steel Non Oriented Fully Processed." Data Sheet. Online available `https://perso.uclouvain.be/ernest.matagne/ELEC2311/T2006/NOFP.pdf`; accessed on 22th of November 2017.

[39] G. Müller and C. Goth, *FEM für Praktiker - Band 1: Grundlagen*. expert verlag, 2007.

[40] Wikipedia, "Shore durometer." Website. Online available `https://en.wikipedia.org/wiki/Shore_durometer`; accessed on 27th of November 2017.

[41] AVL LIST GmbH, Graz, Austria, *EXCITE Acoustics*$^{\mathrm{TM}}$*: Users Manual*, 2017.